The Dissertation Committee for Kristopher Nickolas Darnell certifies that this is the approved version of the following dissertation:

Phase behavior and the interaction of multiple gas molecules in hydrate-dominated geological flow processes

Committee:

Peter B. Flemings, Supervisor

Hugh Daigle

David DiCarlo

Marc Hesse

David Mohrig

Phase behavior and the interaction of multiple gas molecules in hydrate-dominated geological flow processes

by

Kristopher Nickolas Darnell,

Dissertation

Presented to the Faculty of the Graduate School
of the University of Texas at Austin
in Partial Fulfillment
of the Requirements
for the Degree of

Doctor of Philosophy

The University of Texas at Austin
May 2018

Acknowledgments

I must first thank my advisor, Peter Flemings, for encouraging me to attend graduate school, giving me a second opportunity to pursue a Ph.D., and allowing me the flexibility to pursue this project. My success in science stems directly from your guidance. During my time at UT-Austin, you always seemed to find ways to steer me in the right direction even when the detailed science was far from your field of expertise. I must thank David DiCarlo for making substantial contributions to this work. I don't think I would have advanced this science as far as I did without your course on phase behavior and your general intuition about these systems. I would also like to thank the rest of my committee members, Hugh Daigle, Marc Hesse, and David Mohrig. You all provided valuable feedback during various points of my Ph.D. I'm glad that you were always available to discuss interesting topics or offer insights that diverged from my immediate research group.

I owe a great deal of gratitude to my family, Elaine, Charlie, Andrew, and Kathy. I'm sure that my actions and motivations have seemed ridiculous at times. Thank you for being a constant source of encouragement and unconditional support.

I must acknowledge the wonderful friends I've met during my academic journey that have made this experience so rich and rewarding. Thank you to Dorian Abbot, Mac Cathles, and Michael Glotter for being such amazing friends and bright spots during my days in Chicago. Thank you to Jake Jordan, Colin McNeece, Jasmine Mason, Miguel Cisneros, Stephen Ferencz, Elliot Dahl, Mason Fried, Scott Eckley, Kelly Olsen, and Bryce and Michelle Hermiston. You all made my life in Austin fun and effortless.

Lastly, I must thank Carra for believing in me and being the source of so much happiness. Your resilient optimism and positivity have become essential ingredients of my character. These traits greatly reduced the stress during the final stretch of this Ph.D.

I must also acknowledge generous funding from the University of Texas Institute for Geophysics, ExxonMobil, the U.S. Department of Energy, and NASA.

Phase behavior and the interaction of multiple gas molecules in hydrate-dominated geological flow processes

by

Kristopher Nickolas Darnell, Ph.D.

The University of Texas at Austin, 2018

Supervisor: Peter B. Flemings

Hydrate is a non-stoichiometric, ice-like solid compound of water and gas molecules that forms at low temperatures and high pressures. The stability of a particular hydrate is affected by the molecular composition of the environment in which it forms. For example, salt causes freezing point depression of hydrate much like it does for ice. In addition, a gas molecule, such as methane, that ordinarily forms hydrate at one pressure-temperature condition, may not form hydrate if the gas is mixed with another molecule, such as nitrogen, that requires increased pressure or decreased temperature to form hydrate. Here, I develop a modeling framework that incorporates the phase stability of gas mixtures to understand the coupling of equilibrium thermodynamics and fluid flow that governs hydrate-dominated geological flow processes. I first present a benchmark study that utilizes standard hydrate models to demonstrate the complex phase stability that occurs when salt and only methane are considered. The results show the impact that three-phase equilibrium, or the co-existence of a gas phase, a liquid water phase, and a hydrate phase, has on the evolution of hydrate systems. I then develop compositional phase diagrams for systems composed of water, methane, carbon dioxide, and nitrogen that elucidate how multiple hydrate-forming components interact to alter the composition of hydrate, completely de-stabilize hydrate, or create three-phase equilibrium conditions. I finally incorporate these compositional phase diagrams into a mathematical framework that describes multi-phase fluid flow that I use to simulate a subsurface injection strategy designed to simul-

taneously sequester carbon dioxide as hydrate and produce methane gas. The modeling framework illuminates the processes that govern the dynamic behavior of multiple hydrate-forming components. Simulations of subsurface injection demonstrate behaviors that support field and laboratory observations and clarify how composition impacts internal reservoir dynamics. The modeling framework developed here is general and flexible, so it can be modified to model additional components or to include additional physics. In particular, the modeling framework presented here is well-suited to simulate the buoyant ascent of thermogenic gas mixtures through marine sediments or the out-gassing of hydrate layers within the interior of icy planetary bodies like Enceladus.

Table of Contents

Chapter 1

Introduction

1.1 Background and motivation

The purpose of this thesis is to develop a fundamental understanding of hydrate systems in the presence of multiple hydrate-forming gas molecules using a modeling framework that couples multi-component phase behavior to fluid flow. This framework is applied to one case study where a carbon dioxide and nitrogen mixture is injected into a methane hydrate-bearing reservoir, but could be extended to other geological processes where hydrate plays an integral role in the dynamic evolution of the system. More generally, this work recasts fluid flow in hydrate systems as a process similar to enhanced oil recovery that, both, provides a robust toolkit for the analysis of hydrate systems and simplifies the dynamics to elucidate how phase-partitioning governs hydrate systems.

Prior to this work, the majority of hydrate models (Liu and Flemings, 2007, Garg et al., 2008, Moridis, 2003, Frederick and Buffett, 2014) included only methane as a hydrate-forming gas molecule for a few practical reasons. For instance, the large natural hydrate reservoir found in submarine and subpermafrost deposits on Earth (Milkov, 2004a) is predominantly composed of methane, so it is not necessary in most cases to consider other hydrate-forming gas molecules. In addition, simulations of hydrate deposits in marine environments that include salt introduce significant nonlinear effects (Liu and Flemings, 2007, Smith et al., 2014a), but still do not require computationally intensive dynamic updates to the phase compositions that are required if additional hydrate-forming components are included. Furthermore, there is no shortage of methane hydrate topics to study, which includes, but is not limited to, climate impacts on methane hydrate deposits Archer et al. (2009), Thatcher et al. (2013), Phrampus et al. (2014), fracture generation within methane hydrate deposits (Cook et al., 2008, Daigle and Dugan, 2010), economical methane gas production from hydrate deposits (Boswell, 2007, Collett et al., 2012, Moridis et al., 2007), formation of methane hydrate deposits through methanogensis (Claypool and Kaplan, 1974, Malinverno, 2010), and methane hydrate dissociation induced submarine landslides (Mienert et al., 2005, Xu and Ger-

manovich, 2006). Yet, there are at least two frequently discussed geological processes where the non-methane hydrate-forming components are too important to ignore but are under-explored due to the lack of capable models.

In the first geological process, a mixture of carbon dioxide and nitrogen is injected as a gas phase into submarine or subpermafrost methane hydrate-bearing reservoirs to produce methane gas and simultaneously store carbon dioxide as hydrate on geological time scales (Ohgaki et al., 1996, Park et al., 2006). This injection strategy is designed to leverage the difference in hydrate stability of each component to de-stabilize methane hydrate through chemical changes rather than pressure and/or temperature changes that are often proposed as methane hydrate production strategies (Moridis and Reagan, 2011, Collett et al., 2012). This injection strategy received a great deal of attention in the 2000s and 2010s (Ersland et al., 2009, Birkedal et al., 2015, Ersland et al., 2010, Park et al., 2006, Hauge et al., 2014, Anderson et al., 2014, Garapati and Anderson, 2014) and culminated in a field production test on the northern slope of Alaska that was sponsored by the Department of Energy and ConocoPhillips (Schoderbek and Boswell, 2011, Boswell et al., 2017).

In the second geological process, thermogenic gas composed of multiple, hydrate-forming hydrocarbons ascends through the marine sediment column and forms hydrate of variable, depth-dependent composition. This depth dependence produces hydrate deposits progressively more enriched in the heavier hydrocarbons with increasing depth, since ethane and propane hydrate are stable at greater temperatures, hence greater depth, than methane hydrate. The consequence is that the buoyant gas phase is also progressively more enriched in methane with decreasing depth. This geological process is purely conceptual at present, but is an increasingly plausible mechanism to create natural gas hydrate deposits for three main reasons. First, the presence of two hydrate-based phase transitions, a deeper phase transition where the source gas mixture first forms an ethane-rich hydrate and another where methane-rich gas forms pure methane hydrate at shallower depths, would explain the double bottom-simulating-reflectors (BSRs) observed in seismic data that have baffled researchers (Posewang and Mienert, 1999). Second, progressive enrichment of heavy hydrocarbons in the hydrate phase with increasing depth would explain the same trend observed in the gas composition of conventional and pressure cores recovered from hydrate-bearing deposits (Paganoni

et al., 2016). Third, progressive enrichment of methane in the gas phase with decreasing depth would explain the pervasive lack of heavier hydrocarbons within the methane hydrate stability zone, which is traditionally interpreted to indicate a biogenic source of methane (Paull et al., 1994).

The modeling framework developed here is used to simulate CO_2-N_2 subsurface injection rather than thermogenic gas ascent for a few strategic reasons. First, there is a large amount of data from the laboratory (Birkedal et al., 2015, Youn et al., 2016, Yonkofski et al., 2016), field (Schoderbek and Boswell, 2011, Boswell et al., 2017), and early models (Anderson et al., 2014, Garapati and Anderson, 2014, White and Suk Lee, 2014) that serve as comparison to the work presented here. Second, the reported results that probe this injection strategy are contradictory and not well understood, which necessitates a more systematic analysis like the one presented here. Third, the phase behavior in a H_2O-CH_4-CO_2-N_2 system is simpler than it is for the system that characterizes thermogenic gas ascent, so the simulation of the injection process is a logical first step towards understanding multiple hydrate-forming systems. Fourth, fluid flow in CO_2-N_2 subsurface injection is also much simpler since it is sufficient to model a 1-dimensional, horizontal domain with isothermal and isobaric pressure-temperature conditions whereas a model for thermogenic gas ascent requires gradients in pressure and temperature across a vertical domain.

The modeling framework was composed in two stages. In the first stage, I replicated state-of-the-art software (Ballard and Sloan Jr, 2002, Ballard and Sloan, 2004a, Jager et al., 2003) widely used to predict hydrate stability that draws on decades of fundamental laboratory research (Sloan Jr and Koh, 2007), but was previously not incorporated into dynamic models due to various cumbersome characteristics. With this replicated thermodynamics simulator, I constructed various phase diagrams and developed techniques that integrate them into dynamic models through computationally fast simplifications (Rannou et al., 2013). In the second stage, I simulated the evolution of multiple, hydrate-forming components by borrowing ideas from 'Theory of Gas Injection Processes' (Orr, 2007) that have been used to study enhanced oil recovery (Welge et al., 1952, Pope et al., 1980) and enhanced coalbed methane recovery (Seto et al., 2009, Jessen et al., 2008).

While this modeling framework is not nearly as sophisticated as other hy-

drate models composed of only methane (Liu and Flemings, 2007, Moridis, 2003, Frederick and Buffett, 2014), it is a viable, flexible framework that can be extended to include additional components or physics. In particular, it seems to be the most promising framework to model the ascent of thermogenic gas through marine sediment or the evolution of multi-component hydrate layers contained within icy planetary bodies (Liu et al., 2016, Kieffer et al., 2006).

In the rest of this thesis, I present three chapters that progressively build towards the modeling framework for simulating the evolution of multiple, hydrate-forming components.

In Chapter 2, I show results from a multi-component, multi-phase fluid and heat flow simulator that considers only methane as a hydrate-former where I simulate the impact of ocean warming on marine methane hydrate deposits. These results provide an example of how phase behavior and fluid flow are coupled in hydrate systems. In particular, I show that the interaction between methane hydrate and salinity is quite complex and can lead to interesting physical behavior, including a phenomena I refer to as *transient venting*.

In Chapter 3, I describe how multiple, hydrate-forming components modify the phase behavior of hydrate systems. I present compositional phase diagrams that are both useful for understanding the fundamental interaction of multiple hydrate-forming components and novel since they have not been previously presented in the study of hydrate systems. These phase diagrams are essential components of the modeling framework developed here, which parallels the work in enhanced oil recovery. Furthermore, these phase diagrams alone are sufficient to clearly demonstrate the hydrate de-stabilizing effect of nitrogen that agrees well with laboratory and field observations.

In Chapter 4, I introduce multi-phase, fluid flow equations and describe how those equations are coupled to the phase diagrams presented in Chapter 3. I then simulate CO_2-N_2 subsurface injection described above and compare the results with other previously published laboratory, field, and modeling results. I argue that N_2 drives all the dynamics during the injection even though this injection strategy has been repeatedly and emphatically referred to as a simple CO_2-CH_4 exchange. In particular, I show that the local N_2 concentration impacts the reservoir dynamics very similarly to the way salt impacts marine methane hydrate deposits

presented in Chapter 2. This finding adheres to observations in the laboratory and in the field, but has previously been under-explored in previous models of the system (Anderson et al., 2014, White and Suk Lee, 2014). I additionally show how the injection procedure conceptualized as simultaneous exchange of carbon dioxide for methane on a mole-to-mole basis can be re-conceptualized has two sequential processes facilitated by nitrogen. In the leading process, nitrogen invades methane hydrate to first temporarily form a multi-component, or mixed, hydrate, that is later dissociated. In the trailing process, nitrogen carries carbon dioxide in a gaseous phase to form a second type of mixed hydrate in the pore space left behind by the leading process.

My work is the first to describe this injection strategy as a set of sequential processes that are mediated by nitrogen; yet, it seems other model results vaguely demonstrate this behavior and either diminish its significance or overlook this effect due to increased focus on hydrate formation mitigation near the injection well.

1.2 Future work

The work presented here explores how multiple phases and multiple components dynamically interact during geological flow processes, but certainly suffers from a few limiting assumptions and additionally only scratches the surface on this topic. Here, I list a few additional directions that could be taken by other workers to advance the concepts explored here.

1. The work presented in Chapter 2 was performed under the assumptions of 1-dimensional flow. One study (Stranne et al., 2016) has since explored similar behavior to show additional differences that exist between multi-phase, multi-component fluid and heat flow models and all others models of methane hydrate deposits. The basic results in Chapter 2 and that paper, which uses a different simulator called TOUGH+HYDRATE (Moridis, 2003), tend to agree, so there is a large degree of confidence in the results presented in Chapter 2. Yet, 2-dimensional simulations also using TOUGH+HYDRATE (Reagan and Moridis, 2008), show that gas released by hydrate dissociation may flow up-dip along the base of the hydrate dissociation front instead of upward, which might eliminate the secondary hydrate formation front de-

scribed in 2. It would be very interesting to understand if the results presented in 2 also appear in 2-dimensional models, and if so, how they are modified.

2. The work presented in Chapter 4 uses isothermal, isobaric P-T conditions, which amounts to a single compositional phase diagram as presented in Chapter 3. These assumptions might be valid for other injection processes where solid phases do not form, but since hydrate formation/dissociation has such a large latent heat this may not be a valid approximation. While there is mixed evidence concerning temperature changes during gas injection into hydrate-forming regions Boswell et al. (2017), Lee et al. (2013), Yonkofski et al. (2016), it would still be fruitful to introduce conservation of energy constraints into the modeling framework presented in Chapter 4. This could be accomplished by tracking the enthalpy of all mixtures in the compositional phase diagrams, and then creating a dense grid of compositional phase diagrams across the range of P-T conditions expected in the simulations. This procedure is discussed in Rannou et al. (2013) and would be possible for hydrate-forming systems.

3. The work presented in Chapter 4 assumes equilibrium thermodynamics with instantaneous mass transfer between the phases with homogeneous distribution of the phases. At present, there is not substantial evidence to suggest that this assumption is invalid, but it still requires validation in the laboratory. The assumption of equilibrium thermodynamics could be probed in the laboratory using flow-through experiments where the interior reservoir was monitored with micro-CT and micro-Raman while the liquid and gas effluent was analyzed using chromatographic procedures. These measurements could then be used to evaluate the distribution of phases and hydrate composition along profile.

4. The work presented in Chapters 3 and 4 addressed the interaction of water, methane, carbon dioxide, and nitrogen for the purpose of understanding one injection strategy. However, the modeling framework is general and can be modified to understand additional geological processes. Future work on thermogenic gas ascent could use this same framework after the construc-

tion of phase diagrams that include water, methane, and ethane, and possibly propane. Then, the system could be modeled with a single compositional phase diagram or with a domain of multiple, connected phase diagrams. The system could be modeled with or without a conservation of energy constraint. This research direction is very under-explored at present, so even highly idealized models of this system might produce results with significant impact on the field.

Chapter 2

Transient seafloor venting on continental slopes from warming-induced methane hydrate dissociation

2.1 Abstract

[1]Methane held in frozen hydrate cages within marine sediment comprises one of the largest carbon reservoirs on the planet. Recent submarine observations of widespread methane seepage may record hydrate dissociation due to oceanic warming, which consequently may further amplify climate change. Here, we simulate the effect of seafloor warming on marine hydrate deposits using a multiphase flow model. We show that hydrate dissociation, gas migration, and subsequent hydrate formation can generate temporary methane venting into the ocean through the hydrate stability zone. Methane seeps venting through the hydrate stability zone on the Eastern Atlantic margin may record this process due to warming begun thousands of years ago. Our results contrast with the traditional view that venting occurs only up-dip of the hydrate stability zone.

2.2 Introduction

Methane hydrate is a compound containing a lattice cage of water molecules surrounding methane molecules that forms naturally in marine sediments (Sloan, 1998). Within the gas hydrate stability zone (GHSZ), hydrate and water are stable while gas and water are stable beneath it. The thickness of the GHSZ depends on water depth, geothermal gradient, gas composition, pore water salinity and seafloor temperature (Sloan, 1998, Duan et al., 1992, Henry et al., 1999). The GHSZ is wedge-shaped in the dip direction of a continental margin. It is thickest in deep-water where pressure is high and pinches out towards the continental margin (*i.e.*

[1]This chapter published as: Darnell, K. N., and P. B. Flemings (2015), Transient seafloor venting on continental slopes from warming-induced methane hydrate dissociation, Geophys. Res. Lett., 42, 10,765-10,772, doi:10.1002/2015GL067012.

I conceived and designed this study, performed the simulations, gathered the data, conducted the analysis, made the figures, and wrote the manuscript. Peter Flemings edited the manuscript for clarity and provided valuable feedback on the manuscript contents.

the feather-edge of stability) as the water shallows and potentially warms. Gas, water, and hydrate can simultaneously coexist in three-phase equilibrium at the base of the gas hydrate stability zone (BHSZ).

Methane gas, released by hydrate dissociation, can potentially vent into the ocean (Biastoch et al., 2011) and the atmosphere (Rehder et al., 2002). Venting from hydrate dissociation may occur when changes in temperature, pressure, or salinity at the seafloor alter the depth or extent of the GHSZ. For instance, significant oceanic warming would dissociate hydrate and vent gas at the warmest and shallowest extent of the GHSZ, shifting the up-dip pinch-out of the GHSZ to deeper water.

Venting has been observed or hypothesized in various marine settings. In the arctic, offshore Svalbard, venting at the feather-edge of stability is prevalent (Westbrook et al., 2009), long-lived (Berndt et al., 2014), and possibly linked to hydrate dissociation from oceanic warming (Thatcher et al., 2013, Marin-Moreno et al., 2013, Marín-Moreno et al., 2015); however, venting in deepwater at Vestnesa Ridge, offshore Svalbard, appears to result from localized thermogenic processes unrelated to oceanic warming (Smith et al., 2014b, Johnson et al., 2015). In the Atlantic Ocean, hydrate dissociation may source active (Skarke et al., 2014) and future vents (Brothers et al., 2014, Skarke et al., 2014, Phrampus and Hornbach, 2012). Significant future venting is predicted below the Gulf Stream where seismic data reveal hydrate below, as well as up-dip of, the estimated GHSZ (Phrampus and Hornbach, 2012). Widespread venting is also predicted in the Beaufort Sea (Phrampus et al., 2014) and along the Cascadia margin (Hautala et al., 2014) as contemporary warming penetrates and dissociates hydrate deposits.

Numerous mechanisms have been proposed to explain gas migration into vents at the feather-edge of hydrate stability. Westbrook et al. (2009) proposed venting results from up-dip migration of gas along the BHSZ or within dipping strata much deeper than the BHSZ. Reagan and Moridis (2009) simulated that during warming gas migrates up-dip along the BHSZ and vents at the feather-edge of stability. Berndt et al. (2014) proposed episodic venting offshore Svalbard results from migration of gas just below the seafloor when seasonal warming dissociates hydrate. Skarke et al. (2014) proposed venting along the Atlantic Margin results from combined lateral and vertical gas migration that may be sourced by

warming-induced hydrate dissociation. These mechanisms suggest gas migration and venting are influenced by the dynamic location of the GHSZ.

Here, we seek a mechanistic model to describe the evolution of the GHSZ and the subsequent vertical migration of hydrate-dissociated gas during warming. We simulate the response of the methane hydrate system to bottom water temperature change. We extend previous work (Liu and Flemings, 2007, Smith et al., 2014a) and show that seafloor warming can drive episodic venting as a result of the interactions among heat flow, gas flow, and hydrate formation and dissociation. We establish a simple criterion to determine the conditions for vertical venting at the up-dip limit of the GHSZ that can be applied to generic hydrate systems. The model provides insight into how hydrate systems might respond to warming over geological time scales at the feather-edge of stability as may have occurred on continental margins since the last glacial maximum (Skarke et al., 2014, Brothers et al., 2014).

2.3 Methods

We simulate the methane hydrate system with a 1-dimensional model of multiphase fluid flow (Liu and Flemings, 2007) that includes latent heat (Smith et al., 2014a). Initially, seafloor temperature is 3 °C and it increases linearly with depth at 40 °C / km. Above 130 mbsf (the initial BHSZ, B_i), hydrate and water are stable, while gas and water are stable below 130 mbsf (Fig. 2.1).

Methane hydrate occupies 10% of the pore volume ($S_h = 10\%$) between 20 and 130 meters below the seafloor (Fig. 2.1c,d); above and below this, the pores are saturated with seawater. Hydrate is absent between 0 and 20 meters below the seafloor to account for biogeochemical processes that consume methane near the seafloor.

Pressure is hydrostatic with an overlying water column of 550 meters. At the upper boundary, the salt concentration is fixed through time at a constant (seawater) salinity of 3.5 w.t. %, and the pressure is fixed through time to the hydrostatic pressure. The temperature is increased by ΔT at $t = 0$ to simulate the effect of abrupt ocean bottom water warming. At the basal boundary, the salinity is assumed equal to seawater salinity, the heat flux is equal to 40 mW m^{-2}, and the

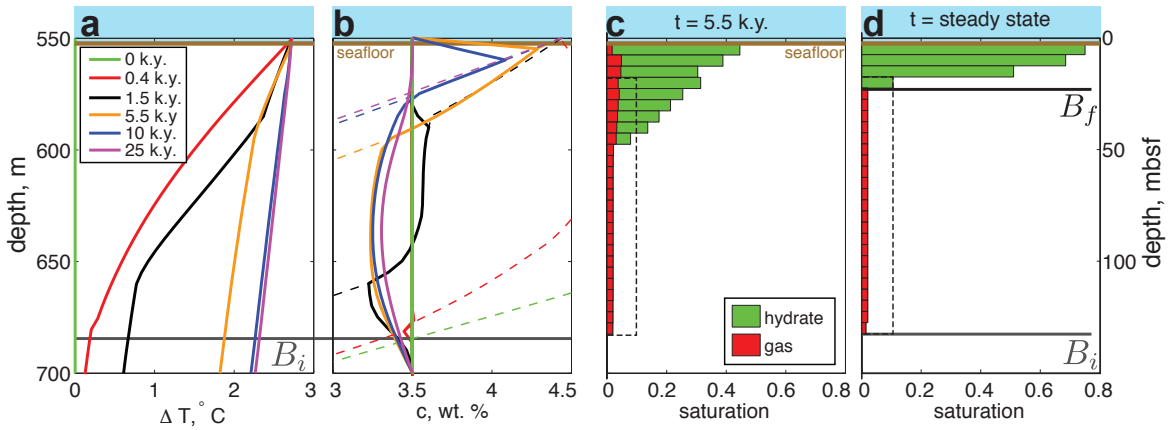

Figure 2.1: Temperature, salinity, and saturation response of sub-seafloor hydrate system subject to seafloor warming of 2.7 °C. (a) Change in temperature from initial profile versus depth. (b) Salinity versus depth (solid lines) with corresponding three-phase equilibrium salinity curves (dashed lines). (c) Gas and hydrate saturations at 5.5 k.y. Gas is venting through the gas pathway and into the ocean. Initial hydrate saturation is shown in dotted line. (d) Steady-state. B_i (initial BHSZ) and B_f (final BHSZ) are marked for reference.

pressure is equal to the hydrostatic pressure. All other parameters are listed in the supplemental file (Table A.3). We use the temperature, salinity, and pressure throughout the simulation to determine the instantaneous thermodynamic phase equilibrium of methane hydrate (Duan et al., 1992, Henry et al., 1999).

We generally choose model parameters that characterize mid-latitude, continental slopes. However, we choose a high hydrate saturation ($S_h = 10\%$) to present the end-member response to warming. In the supplemental text, we demonstrate similar behavior for a 5% hydrate saturation (Fig. A.1).

2.4 Dynamic warming simulation

We simulate the response to a seafloor temperature increase of 2.7 °C, which is a sufficient warming to produce the behavior described below. There are three distinct stages in the resultant model behavior: 1) *warm-up* (0-0.4 k.y.), 2) *gas propagation* (0.4-5.4 k.y.), and 3) *venting and dissipation* (5.4-35 k.y.). During *warm-up*, the sediment warms by heat conduction due to the seafloor temperature increase (red line, Fig. 2.1a). *Warm-up* ends at 0.4 k.y. when hydrate at the BHSZ warms causing

hydrate dissociation, which produces a sharp drop in salinity (red line at B_i, Fig. 2.1b) as fresh water held in hydrate enters the pore space. Hydrate dissociation or formation is controlled by the three-phase equilibrium surface, which is a function of temperature, pressure, and salinity.

We present the thermodynamic state of the system by plotting the instantaneous salinity (c) (solid lines, Fig. 2.1b, 2.2b) with the equilibrium salinity (c_{eq}); equilibrium salinity is the salinity required to achieve three-phase equilibrium at the temperature and pressure present (dashed lines, Fig. 2.1b, 2.2b). Hydrate and liquid water are stable when $c < c_{eq}$, while free gas and liquid water are stable when $c > c_{eq}$. Hydrate, liquid water, and free gas are in equilibrium when $c = c_{eq}$. Therefore, the BHSZ is the lowermost point where $c < c_{eq}$. We mark the initial BHSZ (B_i) and final BHSZ (B_f) for reference (Fig. 2.1).

During *gas propagation* (0.4 k.y.-5.4 k.y.), a zone of three-phase equilibrium propagates upward towards the seafloor (Fig. 2.2c). The three-phase equilibrium zone is initially present in one grid cell when warming partially dissociates the hydrate present; this liberates free gas and fresh liquid water into the pore space, which produces a sharp decrease in salinity (Fig. 2.1b). Since dissociation is an endothermic process, the temperature remains fixed at the local three-phase equilibrium temperature, and a sharp deviation in the temperature profile is visible (Fig. 2.1a, 2.2a). Once free gas produced by dissociation reaches the critical gas saturation ($S_g \approx 2\%$), the free gas buoyantly migrates upward and reforms into hydrate (secondary hydrate formation) where only liquid water and hydrate are stable (Fig. 2.2c,d). The formation of secondary hydrate is self-limiting since hydrate formation consumes fresh water and excludes salt thereby increasing the salinity of the remaining liquid water in the pore space. Secondary hydrate formation locally ceases when $c = c_{eq}$, which allows additional free gas to fill the pore space extending the zone of three-phase equilibrium upward. Any gas produced by dissociation migrates through the three-phase equilibrium zone (Fig. 2.2c) and reforms as hydrate at the top of the three-phase equilibrium zone (Fig. 2.2d). We call this zone a gas pathway because gas originating at the base (dissociation front) travels upward through the pathway and spills out at the top as hydrate (secondary hydrate formation front). Therefore, the gas pathway separates the otherwise coincident base of hydrate stability (dissociation front) from the top of gas stability

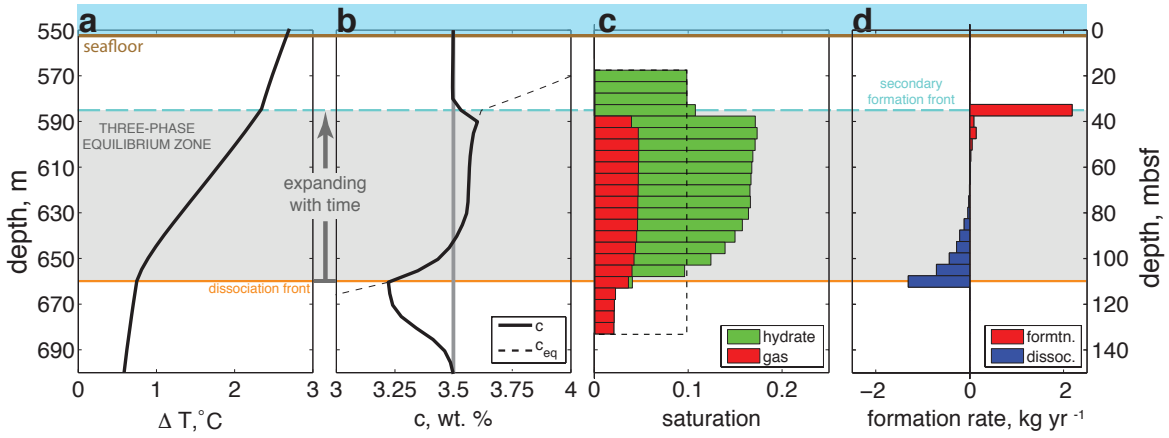

Figure 2.2: Expanded simulation results at 1.5 k.y. (black lines in Fig. 2.1) for sub-seafloor hydrate system subject to seafloor warming of 2.7 ° C. (a) Change in temperature from initial profile versus depth. (b) Salinity versus depth (solid line) with corresponding three-phase equilibrium salinity curve (dashed line). (c) Gas and hydrate saturations versus depth with initial hydrate saturation (dashed line). (d) Instantaneous hydrate formation (dissociation) rate versus depth. The secondary hydrate formation front is indicated with the dashed cyan line and the hydrate dissociation front is indicated with the solid orange line.

(secondary formation front).

Venting and dissipation begins when the gas pathway propagates to the seafloor (5.4 k.y.) (Fig. 2.1c). Gas produced by dissociation travels upward through the pathway and vents into the ocean. Salt enters the ocean at the seafloor by chemical diffusion and advection. The salinity within the system is highest during venting with the largest salinity at the seafloor (4.3 wt. %) and decreasing salinity with depth (orange and cyan lines, Fig. 2.1b). When dissociation ceases and salinity at the seafloor is sufficiently reduced by chemical diffusion, hydrate formation restarts at the seafloor and venting stops (6.5 k.y.). Hydrate reforms throughout the column converting all gas into hydrate. Hydrate spans from 0- 25 mbsf (Fig. 2.1d) at steady state ($\sim$ 35 k.y.), and the three-phase equilibrium zone disappears.

2.5 Model comparison

We compare our 1-d multiphase, fluid-flow model, presented above, with a 1-d conductive heat flow model, since such models are widely used in hydrate studies (Hautala et al., 2014, Berndt et al., 2014, Brothers et al., 2014, Phrampus and Hornbach, 2012). We simulate the conductive heat flow model with Equation (2.1):

$$\frac{\partial T}{\partial t} - \alpha \frac{\partial^2 T}{\partial z^2} = 0, \tag{2.1}$$

where T is temperature, t is simulation time, z is depth below the seafloor, and α is thermal diffusivity.

We assume a constant thermal diffusivity (α) of 2.2×10^{-7} m^2 s^{-1} calculated from bulk-averaged thermal properties of the initial conditions in the multiphase fluid flow model (Table A.3). We impose the same basal heat flux, initial seafloor temperature, and temperature perturbation imposed in the multiphase fluid flow simulation. As a result, the initial temperature profiles are slightly different between models because the conductive heat flow model has uniform thermal properties, while the multiphase fluid flow model has phase-dependent thermal properties. We solve the temperature evolution according to Equation (2.1) using an implicit finite-difference approximation. We use the temperature evolution to calculate the base of hydrate stability throughout the simulation assuming constant salinity of 3.5 wt. % and hydrostatic pressure.

We compare how hydrate stability evolves in each model (Fig. 2.3). Since salinity and pressure are fixed in the conductive heat flow model, the base of the hydrate stability zone is bounded by a sharp interface (black line, Fig. 2.3) where hydrate and liquid water are stable above and gas and liquid water are stable below. Thus, the base of hydrate stability and the top of gas stability coincide throughout the simulation. In contrast, in the multiphase fluid flow model, a three-phase equilibrium zone develops (gray zone, Fig. 2.3) that separates the base of hydrate stability (orange line, Fig. 2.3) from the top of gas stability (cyan line, Fig. 2.3).

In both models, the base of hydrate stability shoals from ≈150 mbsf to 25 mbsf over thousands of years. In the conductive heat flow model, the base of hydrate stability quickly shoals, and then equilibrates to 25 mbsf within 20 k.y. The

base of hydrate stability in the multiphase model follows a similar trajectory, but is slowed by hydrate dissociation, which absorbs heat and freshens the pore water. In contrast, the top of gas stability in the multiphase fluid flow model shoals very rapidly because gas transits through the three-phase zone and reforms as hydrate above the three-phase zone, which releases heat and excludes salt from the hydrate cage. The top of gas stability reaches the seafloor, and then retreats back toward the base of hydrate stability. The base of hydrate stability and top of gas stability converge at 19 k.y., at a depth above their steady state position due to excess heat and salinity generated by hydrate formation. This phase transition slowly deepens as salt and heat diffuse away to background values. At steady state, both models predict a sharp interface at 25 mbsf marking the phase transition between hydrate and gas stability, or simply the base of hydrate stability. The multiphase model predicts that approximately 1% of the initial methane mass is vented into the ocean (Table A.3).

2.6 Generalized venting behavior

We repeat the dynamic simulations for temperature increases that range from 0 to 5 °C while holding all other initial and boundary conditions the same as in the first example (Table A.3). *No venting* occurs and all hydrate remains for small temperature increases (< 2.5 °C), while *complete venting* occurs and no hydrate remains for large temperature increases (> 3.16 °C). *Transient venting* occurs as it did in the example with partial venting of hydrate for the intermediate temperature increases (2.5-3.16 °C). The methane fraction vented increases with increasing warming (Table A.3). The end-member responses either (i.) have a temporary three-phase zone that propagates, then stops and disappears at a depth below the seafloor (*no venting*), or (ii.) have a three-phase zone that propagates and stays at the seafloor until all hydrate dissociates and the GHSZ vanishes (*complete venting*).

We derived an analytical model to generalize our numerical modeling results and describe the conditions necessary for gas venting through the GHSZ on continental margins (A.1). We calculate the depth of the BHSZ after complete warming (B_f) . We assume that all hydrate beneath B_f dissociates, that no hydrate is initially above B_f, and that any salt transport is negligible . We estimate the

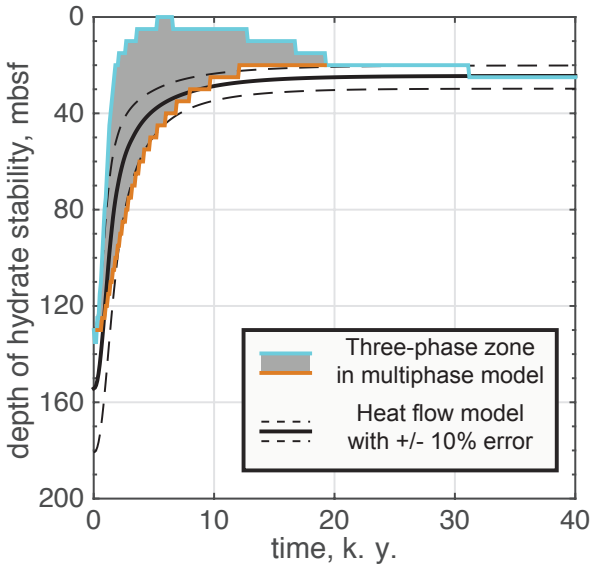

Figure 2.3: Depth of hydrate stability as a function of time for multiphase fluid flow simulation results from Figures 2.1,2.2 compared with a 1-d conductive, heat flow model. We mark the top of gas stability (cyan line), the base of hydrate stability (orange line), and the three-phase equilibrium zone (gray) from the multiphase fluid flow model as we have in Figure 2.2. We mark the base of hydrate stability in heat flow model (solid black line) and provide an error envelope from a +/- 10% change in the bulk-averaged thermal properties (dashed black line). We use $\lambda = 1.09$ W m^{-2}, c =2700 J/kg, $\rho = 1800$ kg/m^3 as bulk-averaged properties.

mass of gas supplied by dissociation (β) as,

$$\beta = A\theta_g\rho_h \int_{B_f}^{B_i} S_h^{(i)}(z)\,\mathrm{d}z, \tag{2.2}$$

where, z is depth below the seafloor, $S_h^{(i)}$ is initial hydrate saturation, ρ_h is hydrate density, A is the nominal area (1 m^2), and θ_g is the fraction of methane contained in hydrate ($\theta_g = 0.14$ by assuming a hydration number of 6) . We then calculate how much gas (γ) is necessary to establish a three-phase equilibrium zone from B_f to the seafloor.

$$\gamma = A\theta_g\rho_h \int_0^{B_f} S_h^{eq}(z)\,\mathrm{d}z = A\theta_g\rho_h \int_0^{B_f} \left(1 - c_0/c^{eq}(z)\right)\mathrm{d}z, \tag{2.3}$$

where S_h^{eq} is the hydrate saturation corresponding to three-phase equilibrium salinity (see A.1 for derivation), c_0 is the initial salinity (3.5 w.t. %), and c^{eq} is the three-phase equilibrium salinity after complete warming. Then, the potential for transient venting, Λ, is the ratio of gas supplied (β) to the amount of hydrate needed to form a vent (γ):

$$\Lambda = \beta\gamma^{-1} \tag{2.4}$$

Transient venting occurs when $\Lambda > 1$ and when a GHSZ remains after warming ($B_f > 0$). *Complete venting* occurs when the GHSZ vanishes after warming ($B_f \leq 0$), and *no venting* occurs under all other scenarios. This analytical approach predicts similar behavior to the multiphase flow model. As additional validation, we run two multiphase simulations at greater water depths and with 10 % hydrate saturation (Table A.3). These simulations produce *transient venting* within the expected *transient venting* temperature range of the analytical model (filled circles, Fig. 2.4).

We use equation (2.4) to analyze venting for an idealized continental margin (Fig. 2.4a,b) that has the same initial seafloor temperature and geothermal gradient as our previous simulations. A bottom water temperature increase of 2.5 °C shoals the base of the hydrate stability zone upward approximately 80 meters (Fig. 2.4a, dashed lines). Complete venting occurs over a lateral distance of 400 meters, where the GHSZ vanishes ($B_f \leq 0$)). *Transient venting* occurs over a finite distance down-dip of the GHSZ pinch-out. According to the linear relationship between $S_h^{(i)}$ and Λ in equations (2.2-2.4), the width of the transient venting zone is dependent on the concentration of hydrate within the dissociated layer (thick lines, Fig. 2.4b). For instance, a few percent hydrate saturation causes venting for only tens of meters seaward of the GHSZ pinch-out, while nearly 100% hydrate saturation would be necessary to cause venting several kilometers seaward of the pinch-out (between vertical white lines, Fig. 2.4a,b). If we assume 5% hydrate saturation, then the *transient venting* region spans approximately 200 m down-dip of the apparent pinch-out of the GHSZ (between vertical white lines, Fig. 2.4a,b).

We evaluate the sensitivity of the analytical model (Fig. 2.5) by perturbing the model from a base state. For this sensitivity, we perturb the water depth, seafloor temperature, magnitude of warming, geothermal gradient, and initial hy-

drate saturation. We include one base state that matches the conditions present in the example of *transient venting* (Fig. 2.5a) and a second base state that does not produce venting (Fig. 2.5b). Water depth and seafloor temperature (combined temperature from T_{sf} and ΔT) have the most dramatic effect on the results (Fig. 2.5), since they control the locations of the BGHSZ before and after warming. In addition, the initial hydrate saturation has a significant effect on the results where greater initial hydrate increases the potential for venting (Fig. 2.5). These basic relationships are corroborated in the multiphase model (Fig. A.1). We provide code at *https://github.com/kdarnell/TransientVenting* that calculates Λ for a given set of input parameters. We encourage the use of this code for assessment of possible *transient venting* sites.

2.7 Evidence for transient venting

We compare our venting predictions with a database of seeps identified by Skarke et al. (2014) (Fig. 2.4c). We use their published water depths and geographical coordinates to calculate bottom water temperature using CTD data from the World Ocean Database (A.1). These temperatures compare well with the Atlantic Ocean thermocline (Fig. 2.4c) identified by Phrampus and Hornbach (2012).

We plot the seeps in a temperature versus water depth hydrate phase diagram (Fig. 2.4c) assuming seawater salinity (3.5 wt. %) and converting water depth to a hydrostatic pressure (with $\rho = 1030$ kg m^{-3}). We identify three types of seeps (Fig. 2.4c). *Type 1* seeps (blue circles, Fig. 2.4c) are located outside of the hydrate stability zone. *Type 2* seeps (red triangles, Fig. 2.4c) are located within the hydrate stability zone, but would require warming of less than two degrees centigrade to destabilize hydrate. *Type 3* seeps (black asterisks, Fig. 2.4c) are well within the hydrate stability zone.

We interpret that the *Type 2* seeps (29 of 577 seeps) could be *transient vents*, but additional field data is needed for confirmation. We base our interpretation on the fact that these *Type 2* seeps are located where gas should not be stable (red triangles; Fig. 2.4c) for the calculated seafloor temperature and assumed seawater salinity. Therefore, temperature or salinity at these seeps must be locally increased to explain their presence if thermodynamic equilibrium is assumed. The seeps

may even be at three-phase equilibrium as has been shown for seeps in the Gulf of Mexico (Smith et al., 2014a). If only salinity is elevated, we calculate the elevated salinity required for local three-phase equilibrium ranges from 3.55 wt. % to 6.1 wt. % depending on the temperature and water depth of each seep. Thus, *transient venting* induced by past warming, as might have occurred since the Last Glacial Maximum, could produce three-phase conditions and explain the present-day gas venting at these seeps. Precise bottom water temperature, seafloor salinity, and gas composition will test this interpretation.

2.8 Conclusion

We described *transient venting* where gas flows upward through the hydrate stability zone and into the ocean from hydrate-dissociated deposits. In this process, gas passes upward through the hydrate stability zone by progressively building a temporary three-phase equilibrium zone towards the seafloor. Hydrate systems near the feather-edge of stability may exhibit *transient venting* when hydrate deposits are warmed above a critical threshold. We established a hydrate venting criterion that can be applied to continental margins around the globe to assess potential venting and to infer subsurface hydrate concentration where venting is observed.

We compared our multiphase fluid flow model with a conductive heat flow model, and we showed that venting is predicted only in the multiphase fluid flow model. The result between models differ because the multiphase model includes phase changes, gas flow, and salinity changes. This model disparity is most pronounced at the feather-edge of stability, where *transient venting* occurs. Thus, dramatic, down-dip shifts in the hydrate stability zone as predicted by conductive, heat flow models (Berndt et al., 2014, Hautala et al., 2014, Phrampus and Hornbach, 2012) may inaccurately predict when and where venting occurs along the margin.

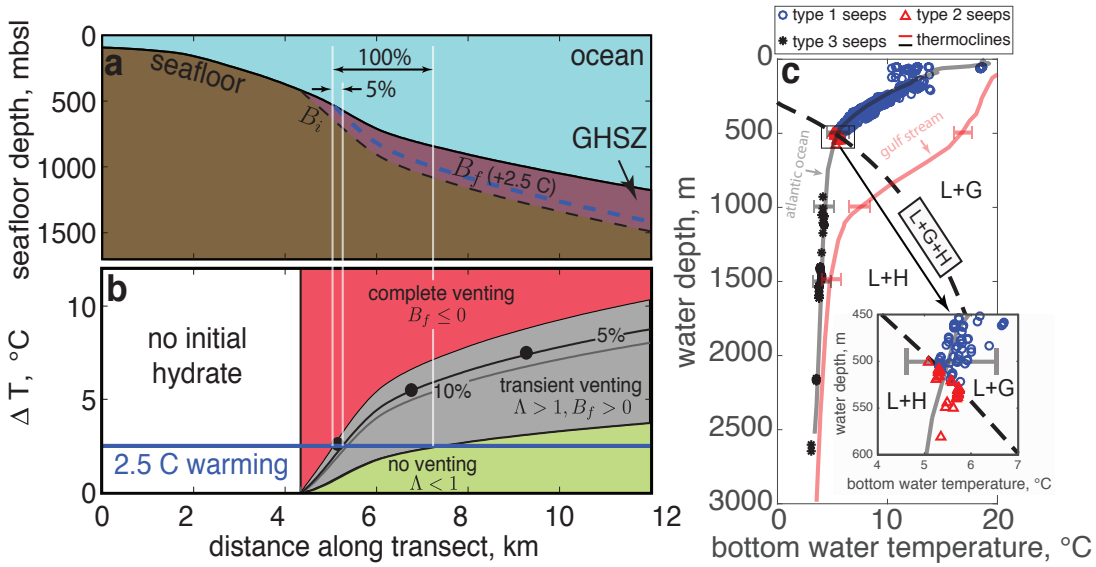

Figure 2.4: Venting predictions for an idealized continental margin using simple analytical model (Equations (2.2)-(2.4)) and venting observations from a seep database. (a) Dip-section of continental margin taken from Eastern Atlantic. Black dashed line denotes initial BHSZ (B_i), and blue dashed line denotes warmed BHSZ (B_f) e. (b) Modeled warming response for initial 3 °C seafloor temperature with 40 °C/km thermal gradient and initial salinity of 3.5 wt. %: *complete venting* (red region) for a large warming, *no venting* (green region) for a small warming, and *transient venting* (gray region) for warming in between end-member responses. *Transient venting* at a given temperature change occurs at hydrate saturation greater than saturation curve. Black, filled circles denote multiphase simulation results (Fig. 2.2,2.3; Table A.3) that record *transient venting* at 10% hydrate saturation. Vertical white lines denote region where *transient venting* is expected at warming of 2.5 °C for 5% and 100% hydrate saturation. (c) Hydrate phase diagram of calculated bottom water temperature using CTD from World Ocean Database (Levitus et al., 1998) versus reported water depth for the 577 seeps observed by Skarke et al. (2014). Faint black and red lines denote the Atlantic Ocean and Gulf Stream thermoclines identified by Phrampus and Hornbach (2012). Dashed line denotes the three-phase equilibrium (L+G+H) boundary for a salinity of 3.5 wt. % and a density of 1030 kg m^{-3}. Hydrate stability (L+H) occurs below L+G+H boundary. Twenty-nine *Type 2* seeps (red triangles) are estimated to lie within the present day hydrate stability zone, but less than 2 °C from destabilization.

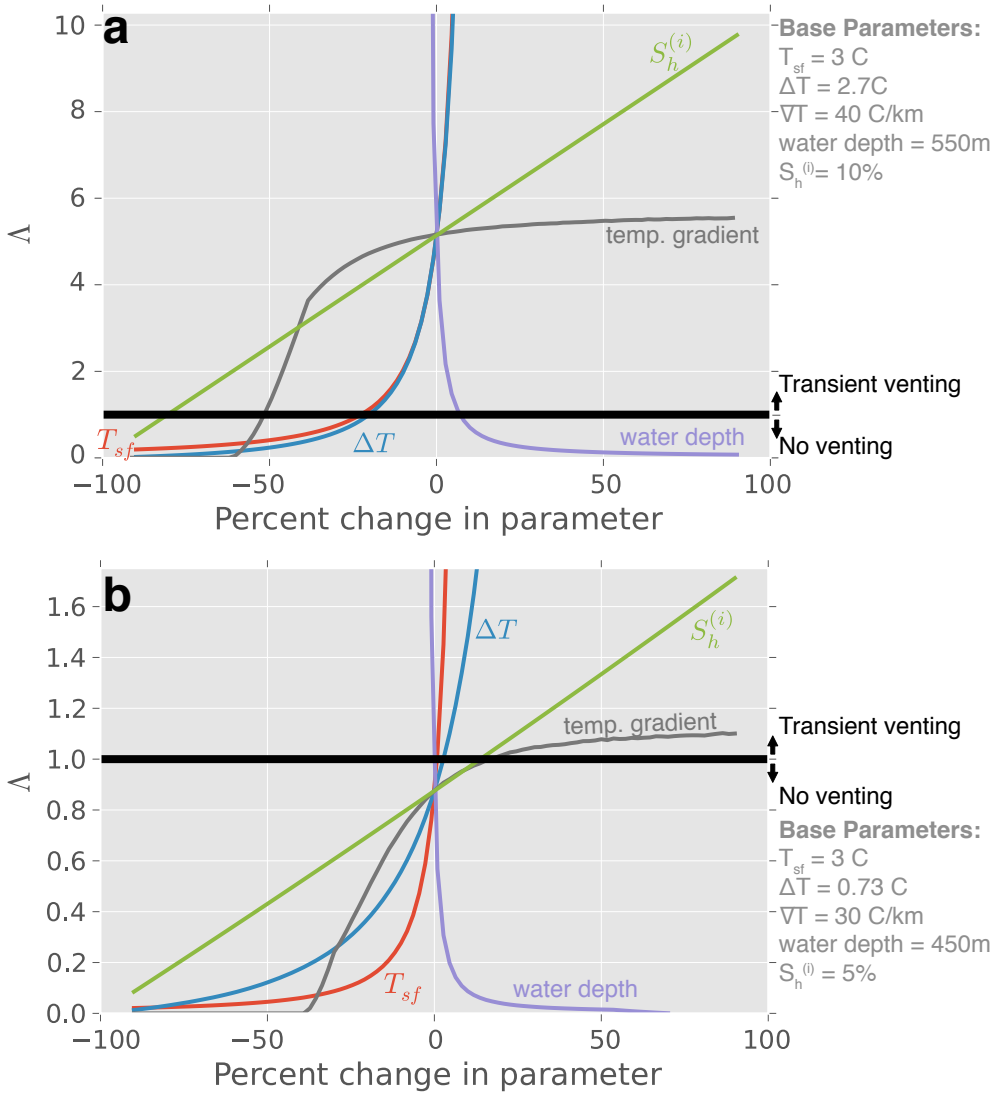

Figure 2.5: Sensitivity analysis of analytical model with variations to the seafloor temperature (T_{sf}), seafloor warming (ΔT), seafloor temperature gradient (∇T), water depth, and initial hydrate saturation ($S_h^{(i)}$). Each parameter is adjusted in isolation as a percentage change of its base value while all other parameters remain fixed. The resulting Λ value calculated from equation (2.4) is used to determine whether or not transient venting occurs. (a) The base parameters are the same as those used in the example of the main text, which produced *transient venting*. (b) Arbitrary base parameters that are different parameters from (a), and where the base parameters produce *no venting*.

Chapter 3

Subsurface injection of combustion power plant effluent as a solid-phase carbon dioxide storage strategy

3.1 Abstract

[1]Long-term geological storage of CO_2 may be essential for greenhouse gas mitigation, so a number of storage strategies have been developed that utilize a variety of physical processes. Recent work shows that injection of combustion power plant effluent, a mixture of CO_2 and N_2, into CH_4 hydrate-bearing reservoirs blends CO_2 storage with simultaneous CH_4 production where the CO_2 is stored in hydrate, an immobile, solid compound. This strategy creates economic value from the CH_4 production, reduces the pre-injection complexity since costly CO_2 distillation is circumvented, and limits leakage since hydrate is immobile. Here, we explore the phase behavior of these types of injections and describe the individual roles of H_2O, CO_2, CH_4, and N_2 as these components partition into aqueous, vapor, hydrate, and liquid CO_2 phases. Our results show that CO_2 storage in sub-permafrost or sub-marine hydrate-forming reservoirs requires co-injection of N_2 to maintain two-phase flow and limit plugging.

3.2 Introduction

Hydrates, or hydrate clathrates, are non-stoichiometric, ice-like solid compounds that form at low temperatures and high pressures (Sloan Jr and Koh, 2007). The hydrate unit cell consists of hydrogen-bonded H_2O molecules organized as cages of various sizes and structures that enclose gas molecules, called guest-molecules (Sloan Jr and Koh, 2007). Simple hydrates are composed of a single

[1]This chapter published as: Darnell, K. N., P. B. Flemings, and D. DiCarlo (2017), Subsurface injection of combustion power plant effluent as a solid-phase carbon dioxide storage strategy, Geophys. Res. Lett., 44, 5521-5530, doi:10.1002/2017GL073663.

I conceived and designed this study, wrote the code to perform calculations, conducted the analysis, made the figures, and wrote the manuscript. Peter Flemings edited the manuscript for clarity and provided valuable feedback on the manuscript contents. David DiCarlo also edited the manuscript for clarity and provided valuable feedback on the figures and the analysis.

guest-molecule (*e.g.*, CH_4 hydrate, CO_2 hydrate, H_2S hydrate), while mixed hydrates are composed of multiple guest-molecules. On Earth CH_4 hydrates form in sediment buried below the seafloor throughout the world's oceans and below permafrost in the arctic (Wallmann et al., 2012, Milkov, 2004b). Mixed hydrates of CH_4 and heavier hydrocarbons likely form where natural gas buoyantly ascends towards the seafloor (Smith et al., 2014c, Paganoni et al., 2016), and mixed hydrates of CO_2 and H_2S naturally form pipe-like structures on the seafloor near CO_2 vents (Swart et al., 2000).

Hydrates provide ideal storage for gas molecules because they are dense, immobile solids. For example, massive deposits of naturally occurring CH_4 hydrates sequester CH_4 with an energy density exceeding that of natural gas for a suite of pressure-temperature conditions (Boswell and Collett, 2011). For this reason, CH_4 production of hydrates is a possible future energy resource (Boswell, 2007), and significant research has been undertaken to understand how and where CH_4 hydrates could be produced (Collett et al., 2012, Moridis et al., 2007, Moridis and Reagan, 2011). The natural storage potential of CH_4 hydrates motivated several hydrate-based CO_2 storage strategies (House et al., 2006, You et al., 2015, Sun and Englezos, 2017). Storage of CO_2 as hydrate would limit fluid leakage into the surrounding environment (House et al., 2006) and would sequester the carbon for thousands of years (House et al., 2006). While these strategies demonstrate CO_2 hydrate storage is possible in deep (House et al., 2006) or shallow (You et al., 2015) marine environments, they require injection of pure CO_2 and do not provide any useful by-product.

Hydrate-based "guest-molecule exchange" is a technique in which fluid/gas injections into CH_4 hydrate-bearing reservoirs induce simultaneous CH_4 production and CO_2 storage (Ohgaki et al., 1996, Kang et al., 2014, Boswell et al., 2017). The process exchanges CH_4 held in hydrate cages for the injected components resulting in CH_4-enriched gas and mixed hydrate enriched in the injected gas (Park et al., 2006, Lee et al., 2013, Boswell et al., 2017). Early work (Ohgaki et al., 1996, Ota et al., 2005b, Lee et al., 2003, Graue et al., 2008) suggested pure CO_2 injection because it is more stable than CH_4 as a hydrate-former and because injection of additional components could reduce CO_2 storage capacity. However, evidence from the laboratory (Park et al., 2006, Birkedal et al., 2015, Seo et al., 2015) and the

field (Schoderbek and Boswell, 2011, Boswell et al., 2017) show that co-injections of N_2 and CO_2 such as combustion power plant effluent, or flue gas (*i.e.,* 80 mol.% N_2 and 20 mol.% CO_2), may be necessary to achieve exchange under water-rich field conditions, which conveniently circumvents pure CO_2 distillation from flue gas.

However, fluid and heat flow models of multi-component hydrate systems are currently primitive (White and Suk Lee, 2014, Anderson et al., 2014), so the dynamics within the interior of the reservoir are still ambiguous. At present, research on hydrate-based guest-molecule exchange relies on effluent histories from core-scale experiments (Youn et al., 2016, Birkedal et al., 2015, Seo et al., 2015) using theoretical (Sun and Englezos, 2017, Birkedal et al., 2015) or experimental (Sun et al., 2016) mixed hydrate stability curves at specific compositional mixtures. For instance, effluent histories from laboratory experiments demonstrate exchange is possible by injection of flue gas into sandstone cores (Birkedal et al., 2015), sand-packed columns (Seo et al., 2015, Yonkofski et al., 2016), and glass bead-packed columns (Youn et al., 2016). Effluent histories from a field-scale production test on the northern Alaskan slope also show successful exchange from flue gas injection into a reservoir overlain by 500 m of permafrost (Schoderbek and Boswell, 2011, Boswell et al., 2017).

The exact mechanism responsible for the improved efficiency of flue gas injections over pure CO_2 injections is unclear (Kang et al., 2014, Koh et al., 2012, Birkedal et al., 2015). In pure CO_2 injections into water-limited systems, a solid-solid exchange process occurs in which hydrate cages remain intact as CH_4 diffuses out of hydrate into the vapor and CO_2 diffuses out of vapor into the hydrate (Ota et al., 2005a). In pure CO_2 injections into water-rich systems, excessive CO_2 hydrate formation restricts fluid flow and limits exchange (Birkedal et al., 2015). The input of N_2 (or O_2) facilitates a thermodynamically favorable workaround to these issues (Kang et al., 2014, Birkedal et al., 2015) that is fundamentally different from pure CO_2 injections. Boswell et al. (2017) interpreted the field test results of flue gas injection as a "bulk exchange" of CH_4 for CO_2 that combined mixed hydrate formation with hydrate dissociation. Kang et al. (2014) similarly described co-injections as a "replacement and decomposition" process, while pure CO_2 injections were exclusively a "replacement" process. The ambiguity of co-injection dynamics is compounded because pure N_2 injections have also been invoked as a

hydrate dissociation mechanism for hydrate-plugged pipelines in a method called "nitrogen-purging" (Panter et al., 2011). It is therefore unclear how co-injections of N_2 and CO_2 into water-rich CH_4 hydrate-bearing reservoirs result in "bulk exchange" of CO_2 for CH_4 or how the dynamics of a "bulk exchange" (Boswell et al., 2017) differ from original descriptions of solid-state "guest molecule exchange" (Ohgaki et al., 1996, Ota et al., 2005a).

To elucidate dynamical compositional changes that occur in mixed hydrate systems, we focus on the compositionally-dependent thermodynamic stability of mixed and simple hydrates of $H_2O/CH_4/CO_2/N_2$ mixtures. We analyze the system using a pressure versus temperature phase diagram (Fig. 3.1), compositional ternary phase diagrams (Fig. 3.2), and compositional quaternary phase diagrams (Figs. 3.3,3.4). We directly compare (Fig. 3.4) a N_2-rich injection to a CO_2-rich injection and show that the emergence of three-phase equilibrium in N_2-rich injections maintain two mobile phases in addition to the immobile hydrate phase. This allows phase-wise partitioning of the components where N_2 dissociates CH_4 hydrate and CO_2 forms mixed hydrate. Our findings fundamentally explain the role N_2 plays in the conflicting, ambiguous processes present during injection of N_2 and CO_2 mixtures into CH_4 hydrate-bearing sediment. We restrict our analysis to a fresh water system for simplicity, so these results are directly applicable to hydrate-forming, sub-permafrost environments like the field site, Ignik Sikumi on Alaska's northern slope (Boswell et al., 2017). However, these results are equally applicable to hydrate-forming saline systems since salt impacts hydrate stability through freezing-point depression. Thus, our results hold for hydrate-based CO_2 storage in sub-marine environments where CH_4 hydrate is abundant (Boswell and Collett, 2011).

3.3 Methods

We simulate thermodynamic stability of mixed and simple hydrates using a flash-type computational framework (Sloan Jr and Koh, 2007, Ballard and Sloan, 2004a) coupled with equations of state that are accurate and suitable for hydrates (Ballard and Sloan Jr, 2002, Jager et al., 2003). We compare individual flash calculations to the thermodynamic simulator CSMGem (Ballard and Sloan,

2004b) (Table S2,S3), which was experimentally validated for $H_2O/CH_4/CO_2/N_2$ mixtures (Sun et al., 2016). However, we cannot directly compare our ternary or quaternary diagrams with CSMGem because CSMGem does not have this capability. Small differences in the calculations potentially change minor things about the presented phase diagrams, but would not eliminate the fundamental finding of three-phase equilibrium regions in the composition space.

We focus our analysis primarily on a single thermodynamic condition, 50 bar and 4 °C (black circle, Fig. 3.1) to describe the details of the phase diagrams. We simulate various other thermodynamic conditions (squares and diamonds, Fig. 3.1) and present the variability of the phase diagrams as a function of pressure and temperature (Fig. B.4,B.5). Our simulated thermodynamic conditions are comparable to the experimental conditions of other studies (cross marks, Fig. 3.1) summarized in Table B.1, including the field test at Ignik Sikumi (Schoderbek and Boswell, 2011, Boswell et al., 2017), on the northern slope of Alaska, USA (≈85 bar, ≈4 °C).

We consider the possibility of an aqueous phase (Aq), a vapor phase (V), a liquid CO_2 phase (L), and a hydrate phase (H). We restrict the calculation to temperatures above 0 °C (*i.e.,* no ice phase) and consider only structure 1 hydrate.

These results apply to fresh water systems since we do not explicitly model the impact of salt on the phase diagrams. However, it is well-known that salt impacts hydrate stability through freezing point depression, similar to the freezing of water. Thus, our results also apply to saline systems.

3.4 Results and Discussion

We present numerous phase diagrams at various thermodynamic conditions that span the pressure-temperate regime most relevant for hydrate-based CO_2 storage. At 50 bar and 4 °C (black circle, Fig. 3.1), we show ternary phase diagrams (Fig. 3.2) where one of the four components is absent. At these conditions, simple (*i.e.,* a single guest) CH_4 hydrate (brown line, Fig. 3.1) and simple CO_2 hydrate (purple line, Fig.3.1) are stable, while simple N_2 hydrate (teal line, Fig. 3.1) is not stable. Liquid CO_2 (dashed purple line, Fig. 3.1) is stable, but vaporizes when combined with sufficient N_2 and/or CH_4. Hydrate stability curves

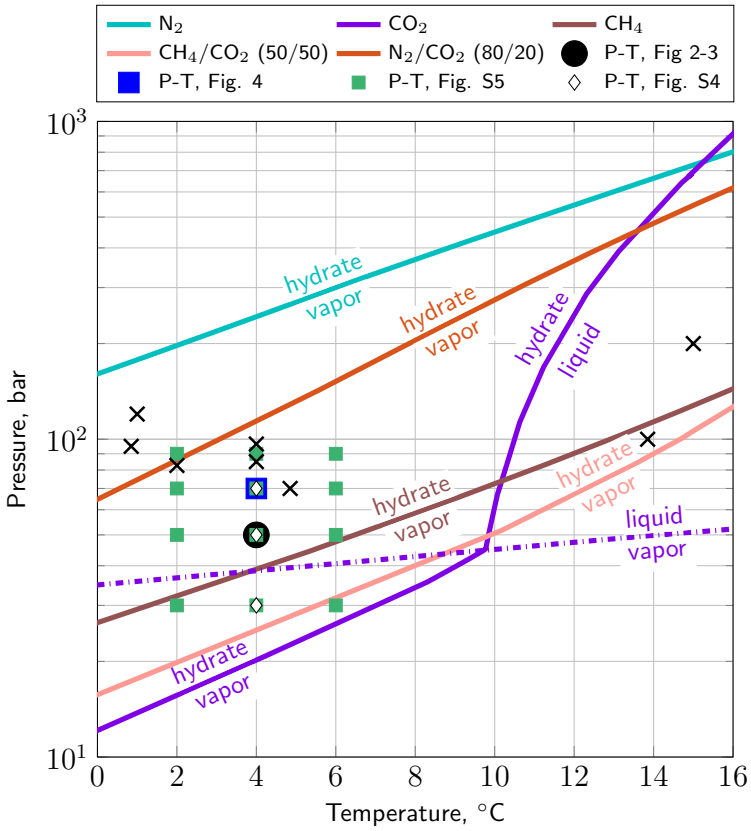

Figure 3.1: Pressure-temperature phase diagram for simple (single guest) hydrates, mixed hydrates (multiple guests), and vapor-liquid equilibrium of CO_2. Mixtures are reported in mole percent. Stable phases are labeled above and below phase boundaries. Colored markers indicate pressures and temperatures analyzed in subsequent figures. Black crosses designate experimental conditions reported in Table B.1.

for an infinite number of mixtures with these components could also be plotted. For reference, we show the stability curves for a 50 mol.% CH_4 and 50 mol.% CO_2 mixture (pink line, Fig. 3.1) and an 80 mol.% N_2 and 20 mol.% CO_2 mixture (red line, Fig. 3.1). We explore additional thermodynamic conditions (squares and diamonds, Fig. 3.1) with ternary (Fig. 3.2, Fig. B.4,B.5) and quaternary (Figs. 3.3,3.4, Fig. B.4) phase diagrams.

3.4.1 Ternary Diagrams at 50 bar and 4 °C

The ternary phase diagrams (Fig. 3.2) show the compositionally-dependent phase stabilities when one of the four components is absent. The aqueous (Aq) single-phase zone occurs near the H_2O vertices at compositions below the mixture solubility. The vapor (V) single-phase zone occurs near the H_2O-free ternary edge at compositions below the vapor saturation of H_2O. The liquid CO_2 (L) single-phase zone occurs near the CO_2 vertex.

In all ternary diagrams (Fig. 3.2), an abrupt phase transition separates the hydrate-vapor (H-V) two-phase zone from the aqueous-hydrate (Aq-H) two-phase zone. This transition is visible in the blow up of the ternary diagrams (Figs. 3.2b,d,f) and occurs for both mixed and simple hydrates (*e.g.*, along H_2O-CH_4 ternary edge of Figure 3.2a). It is commonly referred to as the transition separating the excess-water zone (*i.e.*, Aq-H zone) from the excess-gas zone (*i.e.*, V-H zone). Between these two-phase zones, a single-phase hydrate zone (orange shaded area, Fig. 3.2) is present such that the hydrate composition is identical to the overall composition.

Two distinct types of three-phase zones occur within these ternary diagrams. In the $H_2O/CH_4/N_2$ (Figs. 3.2c,d) and $H_2O/CO_2/N_2$ (Figs. 3.2e,f) ternary diagrams, an aqueous-hydrate-vapor (Aq-H-V) three-phase zone occurs near the middle of the ternary diagrams. The Aq-H-V zones separate the aqueous-vapor (Aq-V) two-phase zone from the hydrate stable zones. At low N_2 abundance relative to the other guests hydrate is stable, while hydrate is not stable at high N_2 abundance relative to the other guests (gray regions, Fig. 3.2). In the $H_2O/CH_4/CO_2$ (Figs. 3.2a,b) and $H_2O/CO_2/N_2$ (Figs. 3.2e,f) ternary diagrams, a liquid-hydrate-vapor (L-H-V) three-phase zone occurs near the ternary edge connecting CO_2 and H_2O. This zone separates the liquid-hydrate (L-H) zone from the hydrate-vapor (H-V) zone. At high CO_2 abundance relative to the other guests, liquid CO_2 is stable, while vapor is stable at low CO_2 abundance relative to the other guests.

3.4.2 Quaternary Diagrams at 50 bar and 4 °C

The ternary diagrams (Fig. 3.2) are equivalent to exterior faces of a larger quaternary diagram of the complete $H_2O/CH_4/CO_2/N_2$ system, so the information contained in the ternary diagrams can be extrapolated to the quaternary dia-

grams. We highlight the two most important features of the ternary diagrams: the hydrate unstable zone (gray zone, Figs. 3.2c-f) and the Aq-H-V three-phase zone (teal tie triangle, Figs. 3.2c-f). We show how these zones project onto the exterior of the quaternary diagram (Fig. 3.3a) and extend through the interior of the quaternary diagram (Figs. 3.3b-d).

The Aq-H-V three-phase zone is not simply a tie triangle on the exterior faces, but instead a sequence of tie triangles that spans from the $H_2O/CH_4/N_2$ exterior face to the $H_2O/CO_2/N_2$ exterior face. The interior tie triangles have continuous composition variations in the aqueous, hydrate (orange line, Figs. 3.3,3.4), and vapor phases (red line, Figs. 3.3,3.4). The complete Aq-H-V three-phase zone within the quaternary diagram is a three-dimensional volume bounded by surfaces connecting the vapor and aqueous phases (teal surface, Fig. 3.3b), the aqueous and hydrate phases (teal surface, Fig. 3.3c), and the hydrate and vapor phases (teal surface, Fig. 3.3d). Each surface of the Aq-H-V three-phase zone represents a family of tie triangle edges (thin, black lines Fig. 3.3).

The one-, two-, and three-phase zones of the ternary diagrams are defined analogously in the quaternary diagram. Hydrate is unstable at compositions whose N_2 fraction exceeds the N_2 fraction on the surface of the Aq-H-V zone connecting the aqueous and vapor phases (gray zone, Fig. 3.3), and compositions in this zone fall on tie lines connecting the aqueous and vapor phases. Three-phases (Aq-H-V) are stable for compositions inside the Aq-H-V bounded volume, and each composition has a corresponding tie triangle that connects the three phases (thin, black lines on teal surfaces, Fig. 3.3). Hydrate is stable at compositions whose N_2 fraction does not exceed the N_2 fraction on any surface of the Aq-H-V three-phase zone. Hydrate stable compositions with a H_2O fraction below $\approx$86 mol.% fall on tie lines in the H-V zone. Likewise, hydrate stable compositions with a H_2O fraction above $\approx$86 mol.% fall on tie lines in the Aq-H zone. Although not pictured, compositions near the CO_2 edge of the quaternary diagram form a liquid CO_2 phase. Thus, there are L, L-H, and L-H-V zones near the CO_2 edge that span the interior of the quaternary diagram between the analogous zones of the exterior faces in the ternary diagrams. We exclude the liquid CO_2 zones from the quaternary diagram because they are not relevant for the rest of the discussion.

3.4.3 Injection Comparison

Our results show how variations in composition of a hydrate system containing N_2 lead to changes in phase stability and the potential for three-phase equilibrium. These results illuminate how the dual function of N_2 as a hydrate-inhibitor at high abundance and a hydrate-former at low abundance combine to produce a Aq-H-V three-phase equilibrium zone. Previous work suggests that N_2 is either a hydrate-inhibitor (Panter et al., 2011) or a hydrate-former (Youn et al., 2016, Park et al., 2006), both not both. Yet, laboratory results (Birkedal et al., 2015, Kang et al., 2014) and the Ignik Sikumi field test (Schoderbek and Boswell, 2011, Hauge et al., 2014, Boswell et al., 2017) hinted that the system evolved in a more complex way than this mutually exclusive binary categorization. Simulations of hydrate exchange at Ignik Sikumi (White and Suk Lee, 2014, Anderson et al., 2014, Hauge et al., 2014) may demonstrate three-phase stability; however, neither the simulations (Anderson et al., 2014) nor the thermodynamic underpinning (Garapati and Anderson, 2014) directly addresses three-phase equilibrium. Furthermore, pseudo-ternary diagrams of the $H_2O/CH_4/CO_2/N_2$ system (Garapati and Anderson, 2014) suggest that only Aq-H or H-V two-phase stability is possible.

Our analysis explains how phase stability is impacted by overall mixture composition, but gas injections are dynamic processes in which local compositions constantly change due to the flow of one or more phases (Anderson et al., 2014, Youn et al., 2016). Enhanced oil recovery is another dynamic injection process that couples multi-phase flow with phase behavior and is often modeled with the aid of a graphical visualization to analyze the evolution of the reservoir (Orr, 2007). Here we borrow the graphical techniques of enhanced oil recovery to understand the first order response of gas injections into CH_4 hydrate reservoirs. In particular, we compare injections rich in CO_2 (J_1, Fig. 3.4a) with those rich in N_2 (J_2, Fig. 3.4b). We use the graphical analysis to show how phases stabilities change (area plots, Fig. 3.4) when either injection is linearly combined with a hypothetical reservoir composition (I, Fig. 3.4) along a mixing line connecting the injections to the reservoir (J_1-I and J_2-I, Fig. 3.4). Along each mixing line, the compositions of each stable phase also change (line plots, Fig. 3.4), which has implications for the transport of each component.

The CO_2-rich injection (J_1-I, Fig. 3.4a) is initially a single-phase vapor, but

small increases in H_2O fraction form hydrate in the two-phase H-V zone (yellow portion of mixing line, Fig. 3.4a). Along the mixing line from J_1 to I, the H_2O fraction increases and more hydrate forms within the two-phase H-V zone (area plot, Fig. 3.4a). When the H_2O fraction exceeds the H_2O fraction within the hydrate phase, the mixing line abruptly transitions into a two-phase Aq-H zone (black portion of mixing line, Fig. 3.4a). Thus, all compositions along the mixing line are hydrate stable with excess material in only one other phase. This is characteristic of the current conceptual picture for guest-molecule exchange. In this type of injection, the injected gas forms mixed hydrate whose composition is different than the initial CH_4 hydrate, but the injection does not induce hydrate dissociation. We suspect that these type of injections are solid-solid, diffusion-based transport processes (Ota et al., 2005a). Furthermore, the constant hydrate stability along the mixing line might lead to plugging of the reservoir as the injected material forms hydrate with H_2O initially in the pore space, eventually restricting fluid flow.

Conversely, the N_2-rich injection (J_2-I, Fig. 3.4b) is initially a single-phase vapor and does not form hydrate when the H_2O fraction is moderately increased. Instead, mixtures with small H_2O fractions are located in the two-phase Aq-V zone (gray portion of mixing line, Fig. 3.4b). Mixtures with a substantial H_2O fraction are in the three-phase Aq-H-V zone (teal portion of mixing line, Fig. 3.4b), and mixtures with large H_2O fraction are in the two-phase Aq-H zone (black portion of mixing line, Fig. 3.4b). This means the injected composition could dissociate the initial CH_4 hydrate or form mixed hydrate depending on the local mixture. In addition, most mixtures along the mixing line have aqueous and vapor phase stabilities, so two-phase flow is possible. Therefore, the local mixtures will constantly change as the flowing phases move downstream at different speeds and with different compositions. The difference in compositions between the vapor and hydrate phases (line plots, Fig. 3.4b) will have a significant impact on the internal dynamics of the reservoir, since the vapor and aqueous phases are mobile, but the hydrate phase is not. Based on this analysis, CO_2 (dot-dashed-line plots, Fig. 3.4b) preferentially enters the hydrate phase and, thus, slowly penetrates the reservoir because hydrate is immobile. In addition, N_2 (solid-line plots, Fig. 3.4b) preferentially enters the vapor phase, and thus, quickly penetrates the reservoir due to the high mobility of the vapor phase. At three-phase equilibrium (teal por-

tion of mixing line, Fig. 3.4b), CH_4 (dashed-line plots, Fig. 3.4b) and N_2 (solid-line plots, Fig. 3.4b) enrich the vapor phase, while CO_2 (dot-dashed-line plots, Fig. 3.4b) enriches the hydrate and aqueous phases. This phase-wise fractionation may lead to highly mobile, N_2-rich vapor that dissociates the initial CH_4 hydrate deep into the reservoir, while most of the injected CO_2 forms immobile, mixed hydrate close to the injection. We surmise that these type of injections are the types that maintain injectivity (*i.e.,* prevent plugging) (Birkedal et al., 2015) and allow for a combination of guest-molecule exchange and hydrate dissociation (Kang et al., 2014, Boswell et al., 2017) that has been called a "bulk exchange" (Boswell et al., 2017). Therefore, the mechanism responsible for the improved efficiency of flue gas injections compared to CO_2-rich injections is the partitioning into hydrate stable/unstable zones, which transports each component through the reservoir at different speeds and in different phases.

A dynamic analysis that includes fluid flow would likely show that the injection and reservoir compositions do not connect linearly, but instead connect along a complicated non-linear path. This type of analysis is beyond the scope of this work; however, extensive gas injection analyses (Orr, 2007) indicate that the linear mixing/dilution line provides a first-order approximation to the phase stability and flow behavior of reservoir injections.

3.5 Implications and Other Applications

Our injection comparison suggests there may be optimal conditions for storage of CO_2 as hydrate and/or production of CH_4 hydrates. Optimal CO_2 storage occurs when the injection mixture is at or near three-phase equilibrium. Such mixtures avoid excessive hydrate build-up near the injection and also store CO_2 in the aqueous and hydrate phases. The amount of mixed CO_2 hydrate formation depends on the local mixture everywhere within the reservoir, which is impacted by fluid and heat flow in addition to the reservoir characteristics. Optimal CH_4 hydrate production occurs when the injection is very unstable to hydrate formation such as pure N_2, N_2-rich mixtures of N_2 and CO_2, or air (Kang et al., 2014). While most studies of injections at hydrate-forming conditions focus on simultaneous storage of CO_2 as hydrate and production of CH_4 hydrates (*i.e.,* 'guest-molecule

exchange'), our work implies that the maximum exchange of guests may be a two-stage process. In stage one, pure N_2 injection produces methane hydrates (*i.e.* 'nitrogen-induced production'). In stage two, co-injection of N_2 and CO_2 mixtures store CO_2 in hydrates (*i.e.* 'nitrogen-assisted storage'). We outline these individual processes below.

3.5.1 Nitrogen-induced Production

Methane hydrate production by N_2 injection likely behaves similarly to the injections of N_2 and CO_2 mixtures we presented, but with more dissociation and less exchange. While one appeal of guest-molecule exchange for CH_4 hydrate production is that it maintains structural integrity of the reservoir during production, itâĂŹs not clear that a reservoir will actually collapse due to rapid dissociation from any production technique (Terao et al., 2014). Therefore, it's reasonable to directly inject a cheap hydrate-inhibitor, such as N_2, to produce hydrate and bypass the exchange process altogether. Our analysis shows that mixed hydrate may still form, which could provide more structural integrity during production than would occur from depressurization alone. In addition, laboratory experiments of nitrogen-purging in hydrate-plugged pipelines already show that N_2 injection is an efficient technique for hydrate dissociation (Panter et al., 2011), so it would likely perform equally well in natural reservoirs.

3.5.2 Nitrogen-assisted Storage

CO_2 storage as hydrate is possible without CH_4 hydrate production (House et al., 2006, Rochelle et al., 2009, You et al., 2015) in various marine and arctic settings due to the favorable thermodynamic conditions for CO_2 hydrate formation. The limiting factor on CO_2 storage as hydrate is the possibility of excessive hydrate buildup (House et al., 2006) near the injection or anywhere else within the reservoir. An efficient technique for CO_2 storage would need to deal with this issue by sufficiently limiting CO_2 hydrate formation. Our analysis shows that N_2 acts as a hydrate-inhibitor that buffers hydrate formation, so flue gas injection into fresh or saline water may avoid the plugging issues associated with hydrate-based pure CO_2 storage. This type of storage could be applied in reservoirs first depleted in

CH_4 hydrate by any production technique or in aquifers at hydrate-forming conditions.

3.6 Conclusion

Our results show that three-phase equilibrium is a prevalent feature of hydrate systems that include N_2 at thermodynamic conditions unfavorable to simple N_2 hydrate stability. This type of three-phase equilibrium demonstrates that, even at fixed temperature and pressure, N_2 behaves as a hydrate-inhibiting substance, as well as a hydrate-forming substance depending on its relative abundance. Furthermore, the three-phase equilibrium conditions that occur in hydrate systems consisting of $H_2O/CH_4/CO_2/N_2$ are likely the reason that injections of N_2 and CO_2 mixtures (*i.e.,* flue gas) have successfully produced CH_4 hydrate and stored CO_2 as hydrate in the lab and in the field through a "bulk exchange". Injections rich in N_2 combine mixed hydrate formation with hydrate dissociation thereby limiting massive hydrate formation that otherwise causes plugging. Injections of this type contrast with pure CO_2 and CO_2-rich injections in which hydrate formation will approach 100% saturation, if sufficient water is supplied. Since injection composition significantly impacts phases stabilities, results from one injection composition cannot be applied to another injection composition without a phase behavior analysis. An optimal strategy for combined CO_2 storage as hydrate and CH_4 hydrate production may be a two-stage process. In stage one, injection of pure N_2 or air into CH_4 hydrate-bearing reservoirs produces all CH_4 in the reservoir through dissociation. In stage two, injection of flue gas, which is at or near three-phase equilibrium, into the CH_4-depleted reservoir stores CO_2 in the reservoir within all stable phases including hydrate, while limiting hydrate formation near the injection.

Our results apply to all environments with hydrate-forming thermodynamic conditions, such as sub-permafrost and sub-marine CH_4 hydrate-bearing reservoirs. Further heat and flow modeling work is required to understand the specific partitioning that occurs during hydrate-related gas injection processes. While this work is directly related to hydrate-based exchange by flue gas injection, the implications of multi-phase stability may be applicable to other mixed hydrate systems.

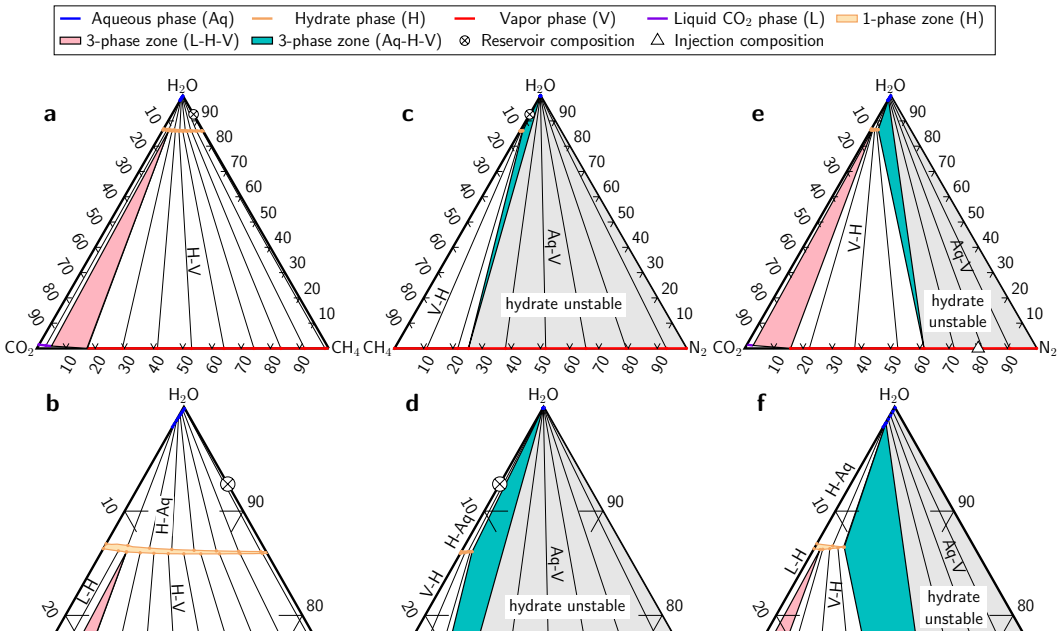

Figure 3.2: Ternary phase diagrams for $H_2O/CH_4/CO_2$ mixtures (a-b), $H_2O/CH_4/N_2$ mixtures (c-d), and $H_2O/CO_2/N_2$ mixtures (e-f) at 4 °C, 50 bar, (black circle, Fig. 3.1). Top row (a,c,e): Complete ternary diagram. Bottom row (b,d,f): Enlarged ternary diagrams near H_2O vertex. Mole percent of lower-right component, lower-left component, and H_2O are labeled along bottom, left, and right axes, respectively. Two-phase zones (*e.g.*, H-V, Aq-H, H-L) have tie lines connecting stable phases drawn with thin, black lines. Three-phase zones (L-H-V, Aq-H-V) are indicated by shaded tie triangles. A single-phase hydrate is shaded in orange. The two-phase zone Aq-V is shaded in gray. A hypothetical reservoir composition of 50 mol.% of methane hydrate and 50 mol.% fresh water is marked with a crossed-circle, and an injection composition of 80 mol.% N_2 and 20 mol.% CO_2 is marked with a white triangle.

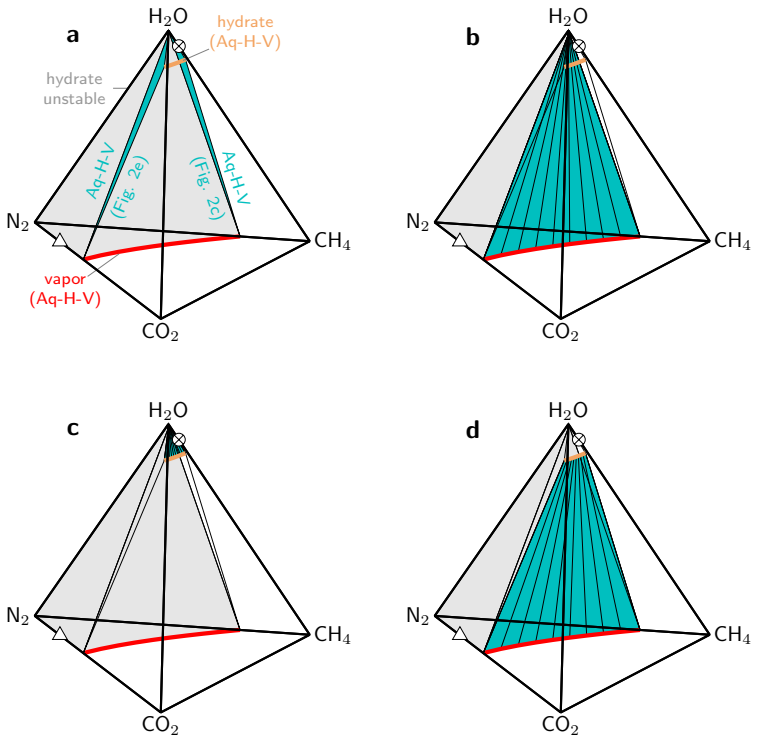

Figure 3.3: Quaternary phase diagrams for $H_2O/CH_4/CO_2/N_2$ mixtures at 4 °C, 50 bar (black circle, Fig. 3.1) with four different perspectives of teal-shaded Aq-H-V three-phase zone. Compositions inside the bounding surfaces of Aq-H-V zone are at three-phase equilibrium. Vapor (red line), hydrate (orange line), and aqueous (not drawn) compositions vary throughout the interior of three-phase zone. Hypothetical reservoir composition (crossed-circle) and potential injection composition (white-filled triangle) from Figure 3.2 are marked for reference. a) Exterior faces of Aq-H-V zone shown in Figure 3.2c-f shaded in teal. b) Interior surface of Aq-H-V zone connecting vapor and aqueous phases shaded in teal. c) Interior surface of Aq-H-V zone connecting hydrate and aqueous phases shaded in teal. c) Interior surface of Aq-H-V zone connecting vapor and hydrate phases shaded in teal.

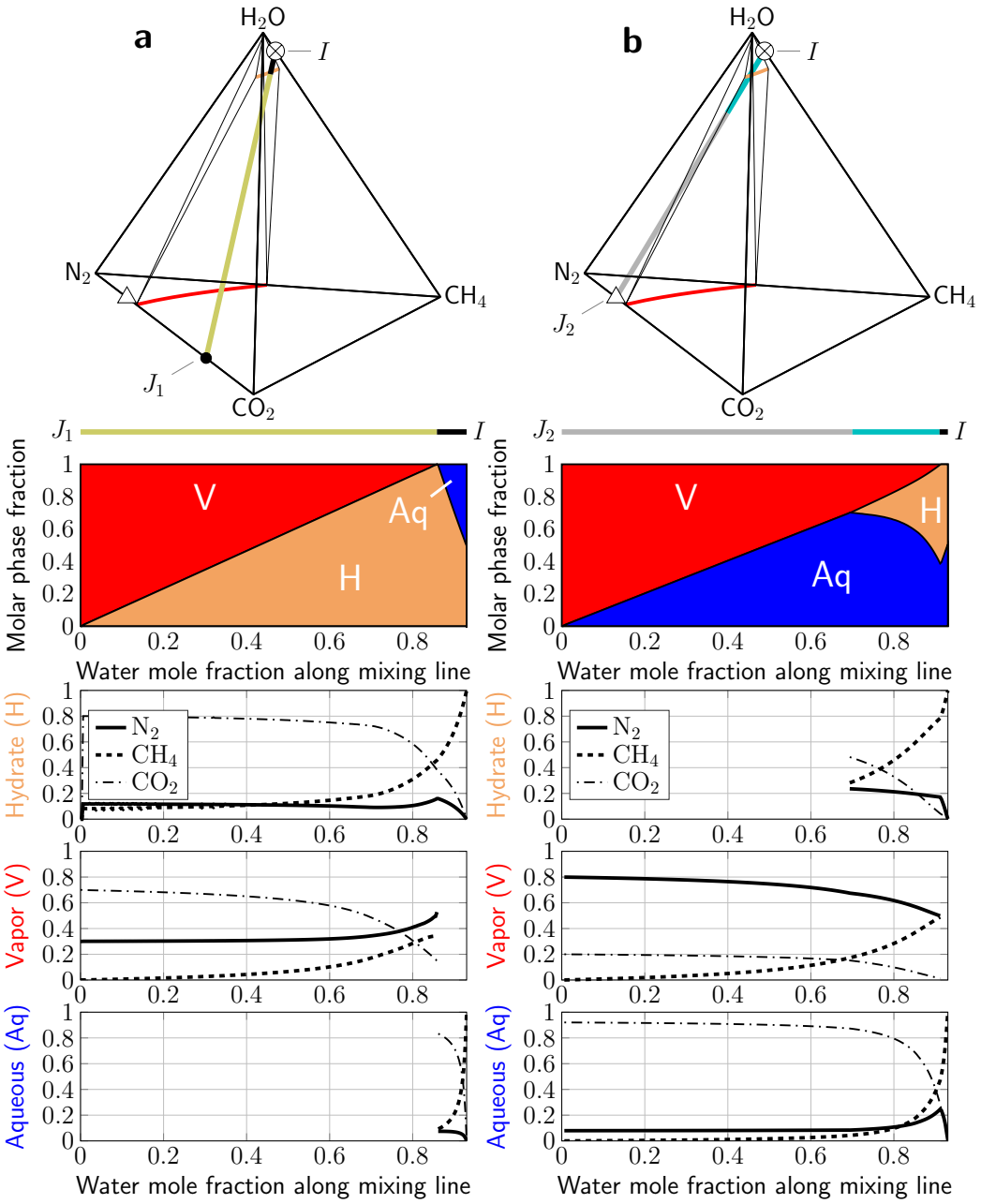

Figure 3.4: Comparison of injections at 4 ◦ C, 70 bar (blue square, Fig. 3.1). Qua-ternary diagrams show mixing lines (J_1-I, J_2-I) that linearly connect injections to a hypothetical reservoir composition I (93/07 mol.% (H_2O/CH_4)). Shaded plots show molar phase fraction as a function of H_2O mole fraction. Line plots show phase-wise, guest-only composition as a function H_2O mole fraction. a) CO_2-rich injection (30/70 mol.% (N_2/CO_2)) J_1 is a vapor phase. Yellow portion of mixing line J_1-I is in the H-V two-phase zone, and black portion (above 86 mol.% H_2O) is in the Aq-H two-phase zone. b) N_2-rich injection (80/20 mol.% (N_2/CO_2)) J_2 is a vapor phase. Gray portion of mixing line J_2-I is hydrate unstable (Aq-V), teal portion is at three-phase equilibrium (Aq-H-V), and black portion is hydrate stable (Aq-H).

Chapter 4

Nitrogen-driven chromatographic separation during gas injection into hydrate-bearing sediments

4.1 Abstract

[1]Hydrates are solid phases primarily composed of water cages enclosing gas molecules that may host large quantities of recoverable natural gas and may serve to sequester carbon dioxide on geological time scales. Most hydrate studies focus on hydrates containing a single gas component, such as methane or carbon dioxide, but there are several settings in which multiple components form hydrate mixtures, or mixed hydrates, including a promising subsurface injection technique that claims to simultaneously recover methane and sequester carbon dioxide called 'guest molecule exchange'. Here, we combine multi-component phase behavior for hydrate-forming systems with a multi-phase fluid flow simulator to understand the evolution of hydrate and non-hydrate phases during subsurface injection. We simulate various scenarios for systems composed of water, methane, carbon dioxide, and nitrogen. Our study probes the impact of the injection composition, the initial reservoir composition, and the transport of each component through the model domain. We observe chromatographic separation, or a compositional profile along the domain, from the combined effect of compositional partitioning in each phase, variable flow speed of each phase, and compositional dependence of phase stabilities. Our results provide insight into the reservoir dynamics during guest molecule exchange that we apply to a field test on the northern Alaskan slope and various laboratory studies. We show that nitrogen drives the chromatographic separation to create a methane-free zone and a carbon dioxide-free zone that are connected by a continuous nitrogen-dominated vapor phase. These results imply that guest molecule exchange acts more like two sequential processes rather than as a simultaneous process. These results also show that injections into reservoirs with and without free water have vastly different behaviors, which has implications for the interpretation of other studies.

[1]This chapter to be submitted to Water Resources Research in May 2018

4.2 Introduction

'Guest molecule exchange' is a subsurface injection technique in which gas (i.e., vapor), composed of carbon dioxide or a carbon dioxide and nitrogen mixture, is injected into a reservoir containing methane to sequester carbon dioxide with simultaneous methane recovery (Boswell et al., 2017). This technique is similar to enhanced coalbed methane recovery (White et al., 2005), but the setting, physical mechanism, and pressure-temperature condition vary significantly between the two techniques. Enhanced coalbed methane recovery leverages the adsorption of molecules onto coal surfaces at high pressures, high temperatures, and in reservoirs occupied by coalbeds (White et al., 2005). In contrast, guest molecule exchange leverages hydrate clathrate (*i.e.,* hydrate), a solid phase that forms at high pressures, low temperatures, and in the presence of water (Boswell et al., 2017). Hydrate is characterized by water cages that enclose guest molecules such as methane or carbon dioxide (Sloan Jr and Koh, 2007). In both techniques, the injection of carbon dioxide is designed to alter either the adsorption of methane (White et al., 2005) or the hydrate stability of methane such that carbon dioxide replaces methane originally within the reservoir (Ohgaki et al., 1996, Park et al., 2006). In fact, the name 'guest molecule exchange' comes from the intended exchange of methane for carbon dioxide within hydrate cages (Ohgaki et al., 1996). In both techniques, carbon dioxide has a greater affinity than methane to either adsorb onto coal surfaces (White et al., 2005) or form a hydrate phase (Park et al., 2006, Sloan Jr and Koh, 2007). The two techniques have differing levels of commercial interest, technical feasibility, and physical understanding, but the similarity between the transport physics suggests analytical tools used for enhanced coalbed methane recovery may advance our understanding of guest molecule exchange.

Guest molecule exchange is commercially attractive because massive methane hydrate deposits naturally occur in subpermafrost and submarine environments (Boswell et al., 2017, Milkov, 2004a) and may be technically feasible as demonstrated by several laboratory experiments (Birkedal et al., 2015, Kang et al., 2014, Park et al., 2006) and a field test on the northern slope of Alaska at a site called 'Ignik Sikumi' (Boswell et al., 2017). However, the economic benefit of the technique is unclear because uncertainty in estimates of methane hydrate inventories (Boswell and Collett, 2011, Milkov, 2004a) and because uncertainty in the cost as-

sociated with subsurface injection of carbon dioxide in addition to the pre-injection carbon dioxide purification and transportation. More importantly, the feasibility of the technology is hindered by a lack of understanding concerning the exchange mechanism (Salamatin et al., 2015), exchange efficiency (Birkedal et al., 2015), and the impact of the injection composition (Birkedal et al., 2015, Kang et al., 2014). In particular, there is ongoing ambiguity concerning the role nitrogen plays in the feasibility of guest molecule exchange. For example, the exact mixture injected at Ignik Sikumi was ≈77% N_2 and ≈23% CO_2, yet guest molecule exchange is often conceptualized as a direct exchange of CO_2 for CH_4 with limited mention of N(Anderson et al., 2014, Birkedal et al., 2015, Boswell et al., 2017).

In contrast to most studies, Darnell et al. (2017) hypothesized that, during guest molecule exchange, nitrogen drives dissociates of methane hydrate within the reservoir independent of carbon dioxide and that additional flow modeling similar to that performed for enhanced coalbed methane recovery (Seto et al., 2009, Jessen et al., 2008) could test this hypothesis. This hypothesis was motivated by multi-component compositional phase diagrams (Darnell et al., 2017) of water, methane, carbon dioxide, and nitrogen mixtures at pressure-temperature conditions in which methane or carbon dioxide form single component hydrates with water but nitrogen does not. The phase diagrams showed that mixtures of all the components produce multicomponent hydrates, or mixed hydrates, but only under mixtures conditions with limited nitrogen content. Above a certain nitrogen threshold, hydrate was not stable and all the components partitioned into a vapor and an aqueous (*i.e.,* liquid water) phase. Darnell et al. (2017) also showed that the compositional phase diagrams indicated the potential for chromatographic separation of the components, since each component partitioned into each equilibrium phase (i.e., aqueous, vapor, hydrate) with different compositions. The hypothesized consequence was the rapid transport of some components in the most mobile phases and vice versa, which is the mechanism that drives enhanced coalbed methane recovery (White et al., 2005). This hypothesis was not tested in the laboratory and few simulators can predict the system evolution (Anderson et al., 2014, White and Suk Lee, 2014). However, results from those simulators have been applied to P-T conditions where all components form hydrate by themselves (White and Suk Lee, 2014, Yonkofski et al., 2016) or with additional geological complex-

ities to mimic the Ignik Sikumi field test (Anderson et al., 2014). Thus, no work has shown whether chromatographic separation is possible when injections into hydrate-bearing reservoirs are performed such that at least one component doesn't form hydrate by itself. Yet, chromatographic separation is a key aspect for analyses of enhanced coalbed methane recovery (Seto et al., 2009, Jessen et al., 2008), which shares many physical similarities with guest molecule exchange.

Here, we seek to understand the evolution of mixed hydrate systems during flow when the system contains multiple components whose individual hydrate stability varies significantly. In particular, we are interested in chromatographic separation of each component by phase partitioning, so we formulate a modeling framework that captures the evolution of hydrates during multi-phase, multi-component flow. Our motivation is to test recent hypotheses about guest molecule exchange (Darnell et al., 2017), provide context for field (Boswell et al., 2017) and laboratory studies of guest molecule exchange (Birkedal et al., 2015, Yonkofski et al., 2016), and illuminate geological flow processes of multiple hydrate-forming hydrocarbon systems (Paganoni et al., 2016). We adapt a modeling framework that has been used for enhanced coalbed methane recovery (Jessen et al., 2008, Seto et al., 2009), enhanced oil recovery (Orr, 2007), and various geological flow processes (Helfferich, 1989, Sathaye et al., 2016) including the evolution of pure methane hydrates during gas injection (You et al., 2015). In this modeling framework, we assume 1-d horizontal flow and solve equations that govern fluid flow through porous media while coupling flow to a flash simulator that predicts phase stabilities as a function of the total composition. Our results indicate that mixed hydrate systems do exhibit chromatographic separation and that the chromatographic separation may explain observations in the field and laboratory. More specifically, nitrogen strongly partitions into the vapor phase, while carbon dioxide strongly partitions into the aqueous and hydrate phases. The net consequence of this partitioning is that nitrogen drives the dissociation of methane hydrate far downstream in a fast-moving front, while nitrogen also combines with carbon dioxide to form a mixed hydrate upstream in a slow-moving front. Remarkably, this causes a complete separation of methane and carbon dioxide, which indicates guest molecule exchange does not operate as one continuous and simultaneous process. Instead, we observe two sequential processes that require nitrogen. In

addition, our results establish benchmark compositional injection and initial condition pairs for future laboratory experiments of guest molecule exchange. While our simulations are idealized, they provide insight into how multiple components interact in nonlinear ways when phase stability is coupled to fluid flow.

4.3 Methods

We simulate multiphase fluid flow in a 1-d, horizontal domain with mixtures composed of water, methane, carbon dioxide, and nitrogen. We inject one composition from the left of the domain into an initial composition that fills the entire model domain. The injection is continuous and constant. We impose an open boundary condition on the right of the domain. We additionally assume no dispersion, no diffusion, homogenous and fixed properties of the porous media (*i.e.,* constant porosity, constant permeability), and negligible capillary and gravity forces.

We conserve mass according to equation 4.1,

$$\frac{\partial G_i}{\partial t} + \frac{\partial H_i}{\partial x}, \text{ for } i = 1, ..., N_c \tag{4.1}$$

where G is the molar concentration of component i, H is the molar flux of component i, t is time, x is the horizontal flow direction, and N_c is the number of components. We define G as

$$G_i = \phi \sum_{j=1}^{N_p} x_{ij} \rho_j S_j, \text{ for } i = 1, ..., N_c \tag{4.2}$$

where ϕ is the porosity, x_{ij} is the molar fraction of component i in phase j, ρ_j is the molar density of phase j, S_j is the volumetric saturation of phase j, and N_p is the number of phases. We define H as

$$H_i = u(1 - S_H)^2 \sum_{j=1}^{N_p} x_{ij} \rho_j f_j, \text{ for } i = 1, ..., N_c \tag{4.3}$$

where f_j is the fractional flow of phase j defined as $f_j = u_j/u$ where u is the total local flow velocity, and u_j is the local flow velocity of phase j.

We non-dimensionalize equation 4.1, which produces

$$\frac{\partial G_{Di}}{\partial \tau} + \frac{\partial H_{Di}}{\partial \xi}, \text{ for } i = 1, ..., N_c \tag{4.4}$$

where $\tau = tu_{inj}/(\phi L)$, $\xi = x/L$, $u_D = u/u_{inj}$, $\rho_{Dj} = \rho_j/\rho_{inj}$, $G_{Di} = G_i/\rho_{inj}$, $H_{Di} = H_i/(u_{inj}\rho_{inj})$ such that L is the length of the domain, u_{inj} is the volumetric flux of the injection, and ρ_{inj} is the molar density of the injection.

We simulate two-phase flow by a simplified Corey's model (Brooks and Corey, 1964) for relative-permeability using a Corey exponent equal to 2 for the vapor phase and 4 for the aqueous phase (equations 4.5-4.10. We express these equations as

$$k_{rV} = (S_V^* - S_{Vc})^2, S_{Vc} < S_V^* < 1 - S_{Aqr} \tag{4.5}$$

$$k_{rV} = 0, S_V^* < S_{Vc} \tag{4.6}$$

$$k_{rV} = 1, S_V^* > 1 - S_{Aqr} \tag{4.7}$$

$$k_{rAq} = (S_{Aq}^* - S_{Aqr})^4, S_{Vc} < S_V^* < 1 - S_{Aqr} \tag{4.8}$$

$$k_{rAq} = 1, 1 - S_V^* > 1 - S_{Vc} \tag{4.9}$$

$$k_{rV} = 0, 1 - S_V^* < S_{Aqr} \tag{4.10}$$

where k_{rV} is the relative permeability of the vapor phase, k_{rAq} is the relative permeability of the aqueous phase, S_{Vc} is the critical vapor phase saturation, S_{Aqr} is the residual aqueous phase saturation, and S_j^* is the normalized saturation of phase j. The normalized saturation accounts for the hydrate phase in a simplified way and is expressed as

$$S_j^* = \frac{S_j}{1 - S_h}, j \in V, Aq \tag{4.11}$$

We transform the relative permeabiliites into a fractional flow representation as

$$f_V = \frac{k_{rV}}{k_{rV} + k_{rAq}/M} = 1 - f_{Aq} \tag{4.12}$$

where M is the fluid mobility. The mobility represents the ratio of mobile phase viscosities, which we express as

$$M = \mu_V / \mu_{Aq} \tag{4.13}$$

where μ_V is the viscosity of the vapor phase and μ_{Aq} is the viscosity of the aqueous phase.

Initial and boundary conditions are given by,

$$z_i(\xi, \tau = 0) = \begin{cases} z_i^{inj}, \xi = 0 \\ z_i^{init}, \xi > 0 \end{cases} \tag{4.14}$$

$$u_D(\xi = 0, \tau) = 1, \tau > 0 \tag{4.15}$$

We simulate flow at a fixed temperature and pressure condition of 70 bar, 4 °C (blue square, Fig. 4.1). At this P-T condition, methane and carbon dioxide form hydrate, but nitrogen does not (Fig. 4.1). However, mixtures of nitrogen and the other components do form hydrate depending on the local mixture. Darnell et al. (2017) show compositional phase diagrams that fully describe the system at this P-T condition.

During flow, the local composition along the domain is a function of time and space. We determine the phase stabilities of each local composition with a fast lookup table calculation that queries a pre-computed phase diagram. These pre-computed phase diagrams are identical to those presented in (Darnell et al., 2017) but with additional information to fully determine all tie lines and tie triangles in the compositional space. A detailed discussion of the construction of the lookup table is presented in Appendix A. For simplicity we assume that the phase density is not a function of composition. Instead, the phase densities are constant for each phase and are listed in Table 1. In addition, we restrict the initial and injection compositions to zones where liquid carbon dioxide is not stable. Thus, the follow-

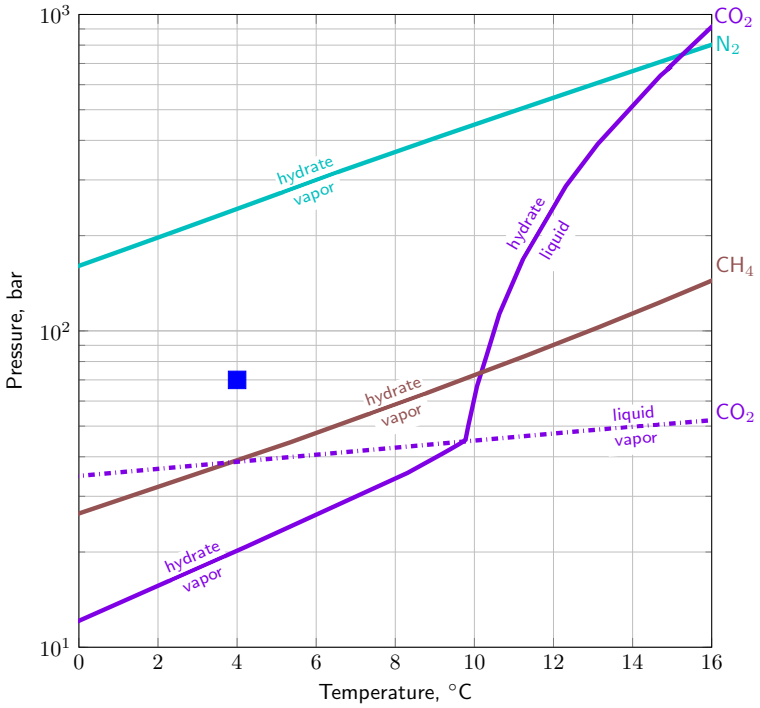

Figure 4.1: Pressure-temperature phase diagram for simple (single guest) hydrates and vapor-liquid equilibrium of CO_2. Stable phases are labeled above and below phase boundaries. Blue square denotes P-T condition (70 bar, 4 °C) we model.

Table 4.1: Model parameters

Parameter	Symbol	Value	Unit
Mobility ratio	M	65	–
Critical vapor phase saturation	S_{Vc}	0.02	–
Residual aqueous phase saturation	S_{Aqr}	0.1	–
Corey exponent for aqueous phase	–	4	–
Corey exponent for vapor phase	–	2	–
Non-dimensionalized molar density of vapor phase	ρ_{DV}	1	–
Non-dimensionalized molar density of aqueous phase	ρ_{DAq}	5.3	–
Non-dimensionalized molar density of hydrate phase	ρ_{DH}	5	–

ing three phases can appear or disappear anywhere within the domain if the total composition predicts their stability: an aqueous phase (Aq), a vapor phase (V), or a hydrate phase (H). These phases may exist in single-phase zones (Aq, H, or V), two-phase zones (Aq-V, H-V, or Aq-H), or three-phases zones (Aq-H-V).

We solve equation 4.4 numerically using the finite volume method with an explicit time-stepping algorithm and a discretization of 300 grid blocks. For each time step, we must solve for u_D such that mass is conserved. We use the method of Dindoruk (1993) that ensures mass conservation by comparing the expected average density according to phase saturations with the average density computed by molar concentrations G_D that result from the time step advancement. We ensure numerical stability by choosing a time step with cfl=0.025.

All additional parameters used in the model are listed in Table 4.1.

4.4 Results

Nine numerical simulations (sim1 through sim9) span a variety of initial and injected compositions. The injected compositions are chosen to demonstrate the impact of increasing nitrogen content such that some injection compositions are hydrate stable (sim4 and sim8), while others are not (sim1, sim2, sim5, sim6, sim9). The remaining simulations (sim3 and sim 7) are very near to three-phase stability (Aq-H-V) conditions. The initial conditions are chosen to represent field conditions (sim1-sim4, sim9) and laboratory conditions (sim5-sim8). The initial conditions

Table 4.2: Initial and injection composition pairs for sim1-sim9

Simulation	injection, $\mathbf{Z}^{inj}$	initial, $\mathbf{Z}^{init}$
sim1	$\mathbf{Z}^{j1}$	$\mathbf{Z}^{i1}$
sim2	$\mathbf{Z}^{j2}$	$\mathbf{Z}^{i1}$
sim3	$\mathbf{Z}^{j3}$	$\mathbf{Z}^{i1}$
sim4	$\mathbf{Z}^{j4}$	$\mathbf{Z}^{i1}$
sim5	$\mathbf{Z}^{j1}$	$\mathbf{Z}^{i2}$
sim6	$\mathbf{Z}^{j2}$	$\mathbf{Z}^{i2}$
sim7	$\mathbf{Z}^{j3}$	$\mathbf{Z}^{i2}$
sim8	$\mathbf{Z}^{j4}$	$\mathbf{Z}^{i2}$
sim9	$\mathbf{Z}^{j2}$	$\mathbf{Z}^{i3}$

representative of the field are methane-limited, so the pore space is occupied by hydrate and excess water. The initial conditions representative of the laboratory are water-limited since methane hydrate is often formed in sediment cores with an unlimited supply of methane, so the pore space is occupied by hydrate and excess vapor. We explicitly model both sets of initial conditions to compare and contrast the results. The matrix of simulations and their characteristics are shown in Table 4.2.

The injection compositions z^{inj} are labeled with superscripts $j1$, $j2$, $j3$, and $j4$ and their compositions are summarized in Table 4.3. Injections z^{j1} and z^{j2} are not hydrate stable, while z^{j4} is hydrate stable. Injection z^{j3} is nearly at the vapor composition of three-phase stability (Aq-H-V) conditions.

The initial compositions z^{init} are labeled with superscripts $i1$, $i2$ and $i3$. Initial composition z^{i1} produces a reservoir where S_H=50% and S_{Aq}=50%. Initial composition z^{i2} produces a reservoir where S_H=50% and S_V=50%. Initial composition z^{i3} produces a reservoir where S_{Aq}=100%.

We first focus on detailed simulation results of sim2 (Figure 4.2) since many features in sim2 appear in other simulations. In sim2, we inject N_2 and CO_2 at a 4:1 mixture (z^{j2}) into a reservoir initially saturated with 50% hydrate and 50% aqueous phases at composition z^{i1}. The injected composition is a hydrate unstable composition. At $\tau = 0.1$, the flow behavior is fully developed (Fig. 4.3), so we focus on this time step first. We observe three distinct zones (circled numbers, Fig. 4.3)

Table 4.3: Reference compositions

Composition	z_{H_2O}	z_{CH_4}	z_{CO_2}	z_{N_2}
$\mathbf{Z}^{i1}$	0.93	0.07	0.0	0.0
$\mathbf{Z}^{i2}$	0.64	0.26	0.0	0.0
$\mathbf{Z}^{i3}$	1.0	0.0	0.0	0.0
$\mathbf{Z}^{j1}$	0.0	0.0	0.0	1.0
$\mathbf{Z}^{j2}$	0.0	0.0	0.2	0.8
$\mathbf{Z}^{j3}$	0.0	0.0	0.25	0.75
$\mathbf{Z}^{j4}$	0.0	0.0	0.3	0.7

in the simulation that are connected by various points in the compositional space (Fig. 4.4). The zones are demarked by sharp boundaries (vertical dashed lines, Fig. 4.3) where there are jumps in compositions on either side of the boundary. The initial state z^{i1} exists farthest downstream with constant phase saturations and phase compositions. Zone 1 is also a constant state z^A (Fig. 4.3b, Fig. 4.4) that spans from the downstream side of the interface between z^{i1} and z^A to the upstream side of the interface between z^A and z^B. It is at three-phase equilibrium (Aq-H-V) with constant phase saturations (Fig. 4.3) and phase compositions (Fig. 4.3c-f). Hydrate saturation in zone 1 is greater than the initial hydrate saturation (Fig. 4.3a). Zone 2 spans from z^B to z^C (Fig. 4.3b, Fig. 4.4) and is also in three-phase equilibrium (Aq-H-V) with constant hydrate saturation but has varying vapor and aqueous saturations (Fig. 4.3a). Hydrate saturation is less than the initial hydrate saturation (Fig. 4.3a). Vapor saturation increases, and consequently aqueous saturation decreases, upstream in zone 2. Zone 3 spans from point z^D to z^E (Fig. 4.3b, Fig. 4.4) and is in two-phase equilibrium (Aq-V) with increasing vapor saturation upstream. Carbon dioxide is absent in zone 1, while methane is absent in zones 2 and 3 (Fig. 4.3c). Nitrogen is present in all zones. The hydrate in zone 1 is a mixed hydrate composed of methane and nitrogen at a constant ratio of 5:1 (Fig. 4.3f), while the hydrate in zone 2 is a mixed hydrate composed of nitrogen and carbon dioxide at a constant ratio of 5:2 (Fig. 4.3f).

Much like the composition path traced in sim2 (Fig. 4.4), there is a path from z^{inj} to z^{init} that is traced in composition space for all simulations. This path is approximately constant throughout the simulation but becomes more apparent

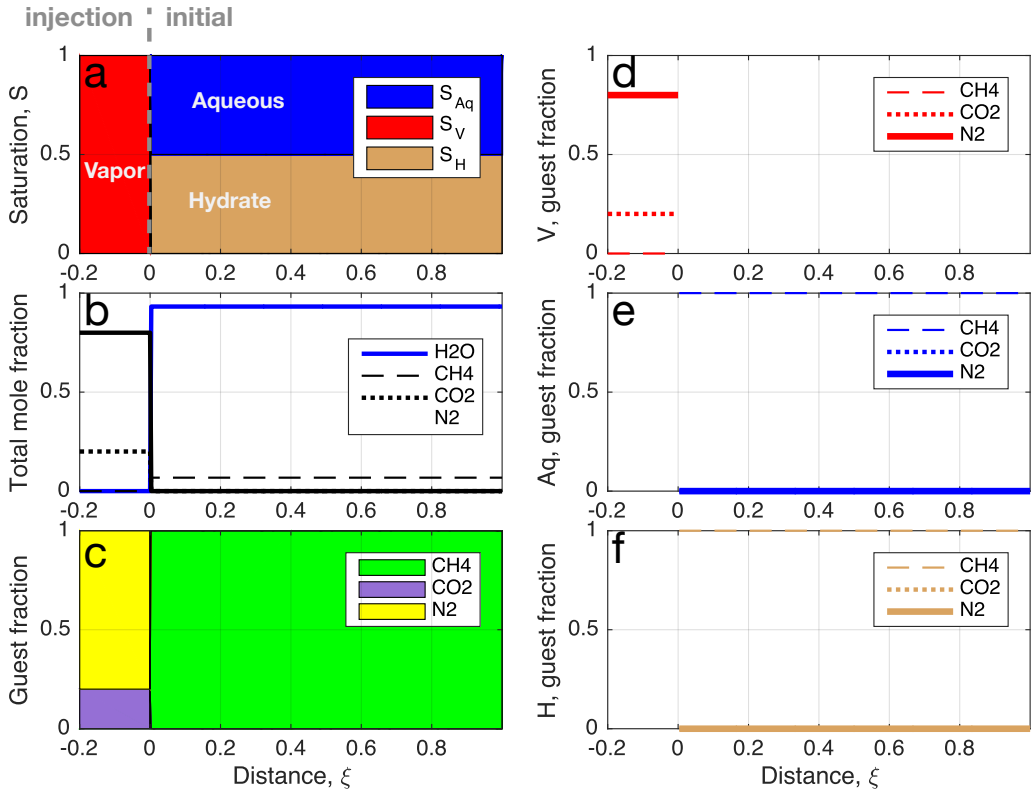

Figure 4.2: Initial and boundary condition for sim2. a) Saturation profile as function of distance downstream from injection at $\xi = 0$. Mixed vapor is injected from left and all material flows to right. Model domain does not exist where $\xi < 0$ but is shown in plots for illustrative purposes. b) Total composition profile of all components in molar fraction. c) Composition of guest molecule molar fraction in all phases. d) Normalized vapor composition profile of guest molecules (i.e., non-water molecules) in molar fraction. e) Normalized aqueous composition profile of guest molecules in molar fraction. f) Normalized hydrate composition profile of guest molecules in molar fraction.

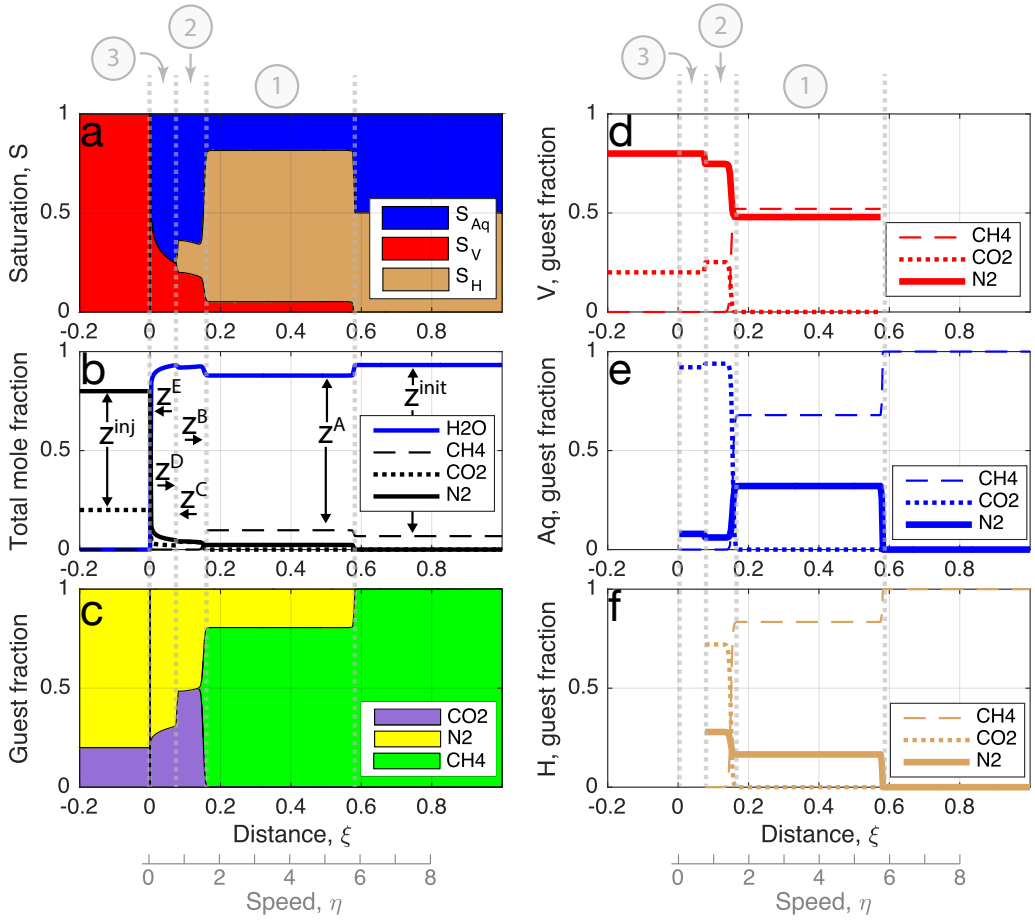

Figure 4.3: Detailed simulation results at $\tau = 0.1$ for sim2. Three distinct zones (*i.e.*, zone 1, zone 2, and zone 3) are labeled with circled numbers and delineated in all plots with vertical gray dashed lines. a) Saturation profile as a function of distance and speed. b) Total mole fraction profile as a function of distance and speed. Seven distinct mole fractions are labeled in black with their positions indicated by arrows. c) Guest mole fraction profile as a function of distance and speed. d) Vapor phase guest mole fraction profile as a function of distance and speed. e) Aqueous phase guest mole fraction profile as a function of distance and speed. f) Hydrate guest mole fraction profile as a function of distance and speed.

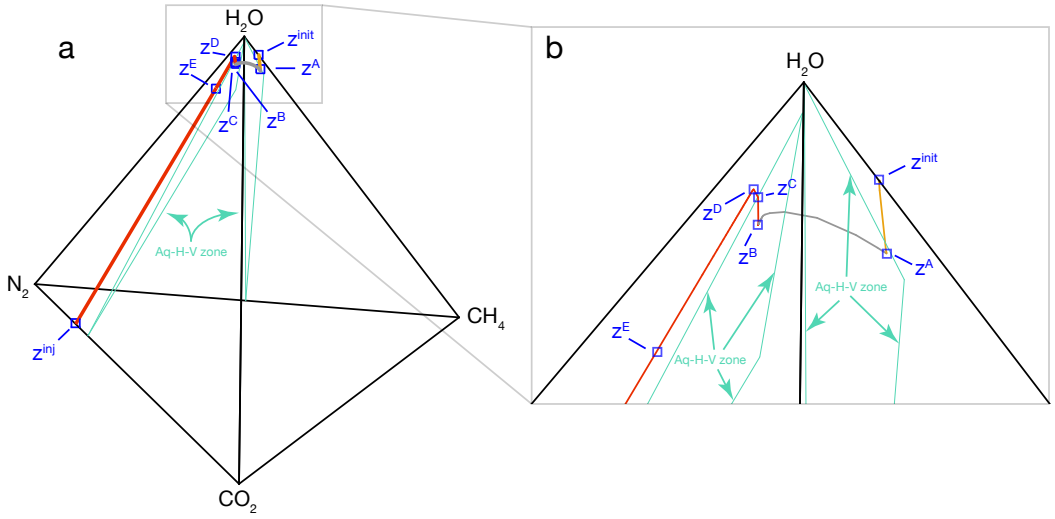

Figure 4.4: Composition path of sim2 in the quaternary diagram at $\tau = 0.1$. a) Full quaternary phase diagram with composition path in a red line when on H_2O-CO_2-N_2 external face, an orange line when on H_2O-CH_4-N_2 external face, and a gray line when all components are present. The composition points described in Figure 4.3c are also shown here as blue squares and labeled the same as before. The three-phase (Aq-H-V) equilibrium zone on the H_2O-CH_4-N_2 and H_2O-CO_2-N_2 external faces of the quaternary diagram are denoted with teal lines. The three-phase equilibrium zone extends throughout the interior of the quaternary diagram between these external faces along the gray line. b) Composition path in the quaternary phase diagram near the H_2O vertex.

as the injection invades additional grid blocks in the domain. For example, the saturation and guest molar fraction profiles in sim2 at four different time snapshots clearly show advection of all material (Fig. 4.5) but also show that the profiles are simply being stretched over time (Fig. 4.5). This behavior is characteristic of self-similar, hyperbolic partial differential equations (Helfferich, 1989, Seto et al., 2009) that has been observed in the simulation of similar injection processes such as in enhanced coalbed methane recovery (Seto et al., 2009). An in-depth discussion of the hyperbolic behavior of this system is beyond the scope of this work. However, this behavior allows us to compare each simulation regardless of the time step by assuming that each composition along the profile has a fixed speed η, which we express as $\eta = \xi/\tau$.

We compare the zones present in sim2 (Fig. 4.3, 4.6) with those present in the other simulations that represent field conditions (Fig. 4.6a,c,d) where there is initially free water in the pore space (sim1, sim3, and sim4). Only nitrogen is injected in sim1 and as a result zone 1 is present but zone 2 is absent (Fig. 4.6a). In addition, there is a zone near the injection that is similar to zone 3 that we denote as zone 3*. Zone 3 and zone 3* are both two-phase (Aq-V) stable with increasing vapor saturation upstream; however, the compositions in these zones differ since only nitrogen is injected in sim1. In general, the character of sim1 and sim2 are similar since both injection compositions are hydrate unstable. In sim3, zone 1 and zone 2 are present, but zone 3 is absent and/or of negligible thickness (Fig. 4.6c). This is because the injection composition is very close to the vapor composition of vapor at three-phase (Aq-H-V) equilibrium. In sim4, zone 1 and zone 2 are present, but zone 3 is replaced by a different zone, which we denote as zone 4 (Fig. 4.6d). Zone 4 is two-phase (H-V) stable with decreasing vapor phase saturation upstream. Contrary to sim1-sim3, the injection composition in sim4 is within the hydrate stability zone. Thus, hydrate immediately forms with free water. Hydrate saturation in sim4 near the injection reaches very high saturations (Fig. 4.6d) that might shut down, or 'plug', flow.

We now compare (Fig. 4.7) the zones identified in the excess water simulations (i.e., sim1-sim4) representative of field conditions (Fig. 4.3, 4.6b) with zones present in the excess vapor simulations (*i.e.*, sim5-sim8) representative of most laboratory conditions where all water in the pore space is initially held in hydrate. In

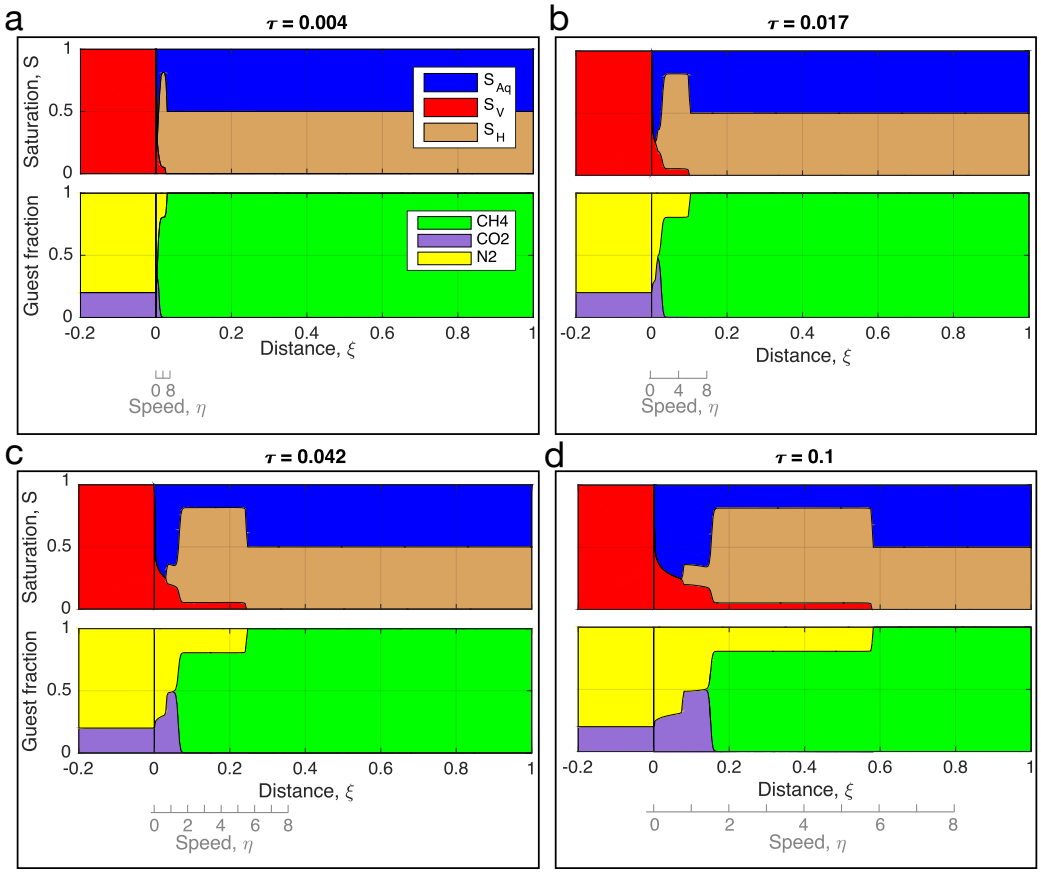

Figure 4.5: Evolution of saturation and guest mole fraction for sim2 at four snapshots with the speed horizontal axis displayed below the distance horizontal axis. a) Profiles at $\tau = 0.0044$. b) Profiles at $\tau = 0.017$. c) Profiles at $\tau = 0.042$. d) Profiles at $\tau = 0.1$.

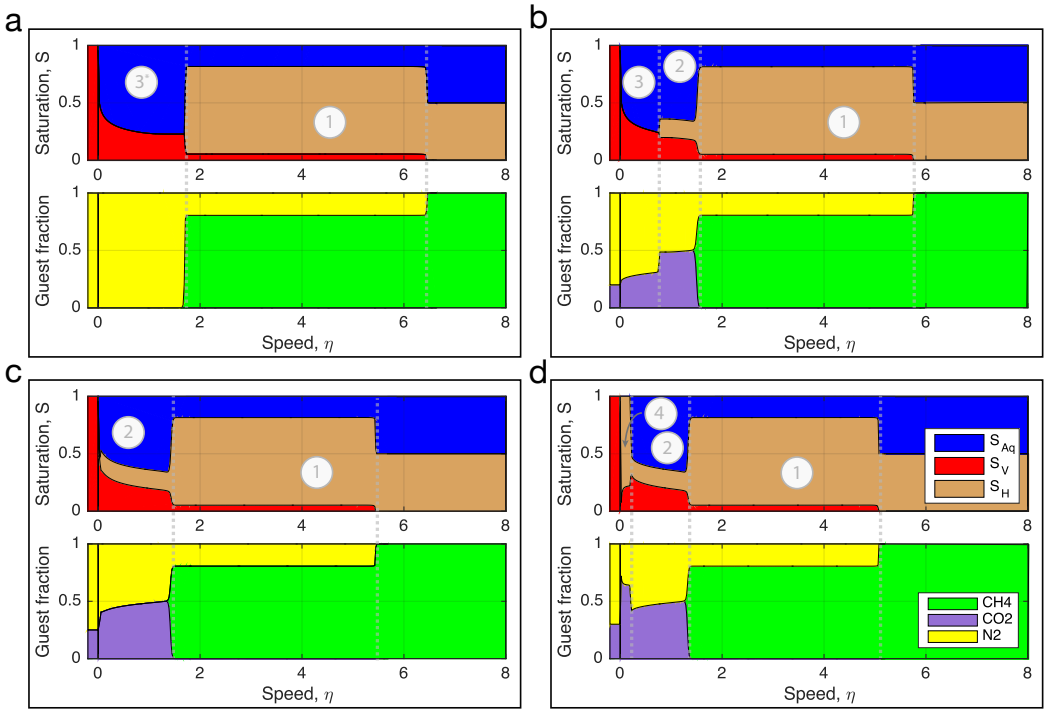

Figure 4.6: Saturation and guest mole fraction profiles for excess-water simulations as a function of speed. Results are shown for sim1 (a), sim2 (b), sim3 (c), and sim4 (d). Legend in (d) applies to whole figure. Phase and composition zones are labeled with circled numbers. Carbon dioxide fraction of the injection increases from (a) to (d).

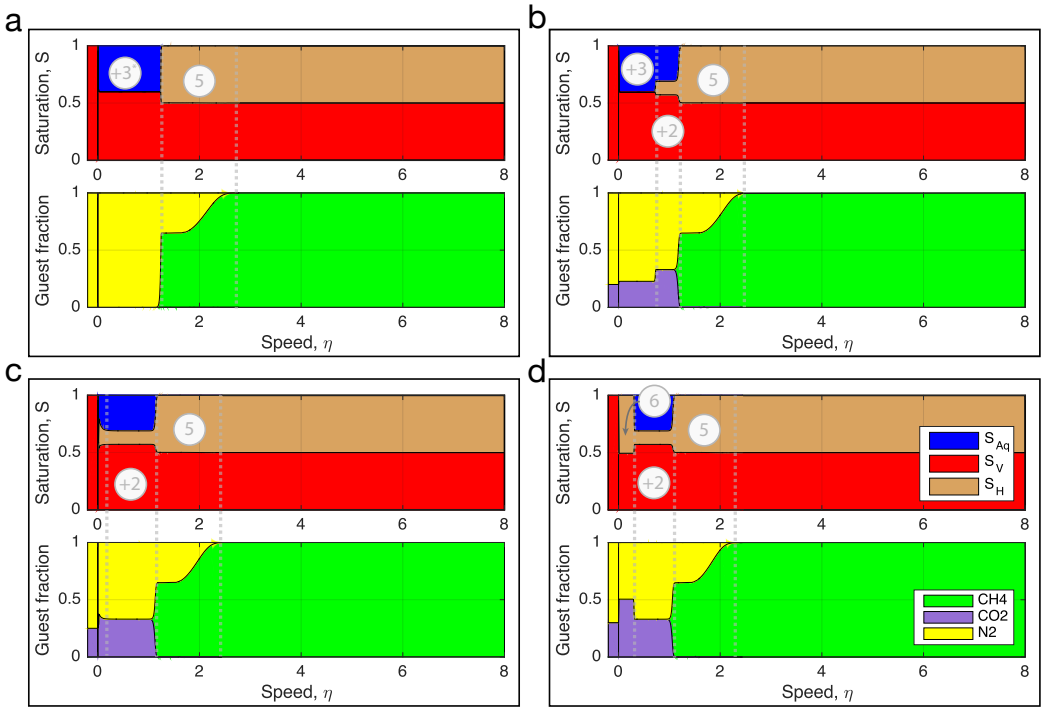

Figure 4.7: Saturation and guest mole fraction profiles for water-limited simulations as a function of speed. Results are shown for sim5 (a), sim6 (b), sim7 (c), and sim8 (d). Legend in (d) applies to whole figure. Phase and composition zones are labeled with circled numbers. Carbon dioxide fraction of the injection increases from (a) to (d).

particular, we compare each excess vapor simulation with the excess water simulation that has an identical injection composition (e.g. sim5 and sim1; sim6 and sim2), which are reported in Table 2. In sim5 we inject 100 mol.% N_2 like we do in sim1 and, consequently, observe zones comparable to those observed in sim1. There is a zone denoted as zone 5 (Fig. 4.7a) of mixed hydrate downstream composed of only methane and nitrogen, which is similar to zone 1 found in sim1-sim4 (Fig. 4.6). Zone 5 is two-phase stable (H-V) with constant saturations much like zone 1. However, unlike zone 1, the phase compositions in zone 5 follow a smooth curve with increasing nitrogen content upstream (Fig. 4.7a). In addition, zone 5 does not display hydrate saturations greater than the initial hydrate saturation. Instead, the hydrate saturation in zone 5 is always equal to the initial hydrate saturation. Farther upstream of zone 5, there is another zone that we denote as +3* (Fig. 4.7a), which is similar to zone 3* found in sim1 (Fig. 4.6a). Zone +3* is two-phase (Aq-V) stable like zone 3* but the phase saturations are constant. In sim6 we inject 80 mol.% N_2 and 20 mol.% CO_2 like we do in sim2. Zone 5 is present in sim6 and there are zones that we denote as zones +2 and +3 (Fig. 4.7b), which are comparable to zones 2 and 3 found in sim2. Zone +2, like zone 2, is three-phase stable (Aq-H-V) with constant phase compositions and hydrate composed of only nitrogen and carbon dioxide. However, unlike zone 2, zone +2 has constant phase saturations. Zone +3, like zone 3, is two-phase stable (Aq-V) and devoid of methane, but unlike zone 3 has constant phase saturations. In sim7 we inject 75 mol.% N_2 and 25 mol.% CO_2 like we do in sim3. Zone 5 and zone +2 are present, and there is a region very close to the injection that appears to have increased hydrate saturation (Fig. 4.7c). However, this region looks progressively more like zone +2 as the simulation evolves, so the increased hydrate saturation is likely an effect of our grid size. In sim8 we injection 70 mol.% N_2 and 30 mol.% CO_2 like we do in sim4. Zone 5 and zone +2 are present, and a new zone that we denote as zone 6 appears near the injection (Fig. 4.7d), which is similar to zone 4 found in sim4 (Fig. 4.6d). Zone 6 is two-phase (Aq-H) stable like zone 4 and devoid of methane. Unlike zone 4, zone 6 has constant phase saturations such that the hydrate saturation is identical to the initial hydrate saturation.

4.5 Discussion

The numerical flow simulations bracket the possible behavior of mixed hydrate systems in which vapor is injected into a reservoir when the injected composition is different than the initial composition. These simulations are performed at pressure-temperature conditions where one of the components, nitrogen, does not form hydrate by itself, which allows us to probe how the hydrate stability of the injection composition impacts the reservoir evolution. In addition, we vary the initial conditions to show a set of simulations representative of field conditions with free water initially in reservoir and a second set of simulations representative of laboratory conditions with all free water initially held in hydrate. The behavior of the system has unique characteristics that we interpret below. In addition, we apply our interpretations to other published work and the field test at Ignik Sikumi. Finally, we describe a series of laboratory tests that could prove the validity of our results.

4.5.1 Interpretation of results

Separation of methane and carbon dioxide

In our simulations, we observe distinct zones separated by sharp interfaces in which abrupt compositional jumps occur across the interfaces. In all of the simulations that contain nitrogen and carbon dioxide, we observe complete separation of methane and carbon dioxide at one of these interfaces (*e.g.,* between zone 1 and zone 2 in Fig. 3, Fig. 4.6b; between zone 5 and zone +2 in Fig. 4.7b). We interpret that this observation is the result of two sequential processes that are joined together at the interfaces. Here, we first focus on that separation in the excess water simulations.

The first, leading, process is the invasion of fast-flowing, low-saturation vapor into the initial state (*i.e.,* interface between initial state and zone 1, Fig. 4.3, 4.6). The vapor is composed of a methane and nitrogen mixture (sim1-sim4, Fig. 4.6b-d). The invading vapor combines with the initial methane hydrate and free water to form additional hydrate composed of methane and nitrogen until the total nitrogen content in all phases is sufficient to create three-phase equilibrium condi-

tions. Thus, the leading front is a hydrate formation front that is self-limiting due to three-phase equilibrium conditions. The high flow speed of the vapor is due to the functional form of equation 4.11, which treats increased hydrate saturation as a reduction in the total pore space.

The second, trailing, process is the invasion of slower-flowing, high-saturation vapor into zone 1 (i.e., interface between zone 1 and zone 3*, Fig. 4.6a; interface between zone 1 and zone 2, Fig. 4.6b-d). The vapor is composed of nitrogen (sim 1, Fig. 4.6a) or a carbon dioxide and nitrogen mixture (sim2-sim4, Fig. 4.6b-d). The total amount of nitrogen flowing into zone 1 at this interface exceeds the nitrogen threshold for three-phase equilibrium conditions present in zone 1, so the hydrate at the upstream extent of zone 1 dissociates. The vapor produced by dissociation at this interface is the source for the mixed methane and nitrogen vapor that invades the initial state in the leading front. Thus, the trailing front is a hydrate dissociation front that strips methane from the system and sweeps it downstream.

This two-stage sequential process is modified in the excess vapor simulations, but sufficiently similar to indicate that methane hydrate dissociation is entirely controlled by the presence of nitrogen and the unique chromatographic separation that occurs in hydrate systems. In the excess vapor simulations (sim5-sim8, Fig. 4.7), the leading hydrate formation front is replaced by another nitrogen-dominated vapor invasion front. Since there is no initial free water to form hydrate, this front alters the composition of the hydrate and vapor phases (zone 5, Fig. 4.7). The observed separation of methane from carbon dioxide in all simulations implies that carbon dioxide does not directly interact with methane, but instead carbon dioxide sequentially flows into the space left behind by the nitrogen-induced hydrate dissociation.

Mixed carbon dioxide hydrate formation

One surprising consequence of chromatographic separation in our simulations is mixed hydrate formation from injections that are hydrate unstable. For instance, neither the 100 mol.% N_2 injection of sim1 nor the 80 mol.% N_2 and 20 mol.% CO_2 injection of sim2 should form hydrate based on thermodynamics, yet there is additional hydrate formation in both simulations and even two types of mixed hydrates in sim2 (i.e., upstream CH_4-free hydrate and downstream CO_2-

free hydrate). This implies that it may be possible to safely and predictably store CO_2 in hydrate without "plugging" if the injection is hydrate unstable, which is counter-intuitive. We investigate the cause of the CH_4-free mixed hydrate formation in sim2 by focusing on the chromatographic separation of the same injection composition of sim2 (4:1, N_2:CO_2) into pure water (Fig. 4.8). We call this simulation sim9 and compare it to both sim1 and sim2.

In sim9 (Fig. 4.8), the injection composition is identical to the injection composition of sim2, but hydrate does not form, which is expected strictly from thermodynamics. However, there is still a general chromatographic separation that is characterized by a leading front of pure nitrogen vapor at low saturation denoted as zone 7 (Fig. 4.8), followed by an upstream zone of carbon dioxide and nitrogen mixtures with variable phase compositions and phase saturations (zone 3, Fig. 4.8), which resembles zone 3 of sim1 (Fig. 4.6a) and sim2 (Fig. 4.3, 4.6b). Since there is no hydrate formation in sim9, the system is governed by the multi-phase flow and phase partitioning of only the vapor and aqueous phases. Carbon dioxide trails nitrogen in sim9 because its solubility in the aqueous phase is much larger than nitrogen (i.e., $\approx$15:1) and because the aqueous phase is much slower than the vapor phase at vapor saturations above 10%. The consequence of this phase partitioning and multi-phase flow is the enrichment of carbon dioxide near the injection with a maximum carbon dioxide fraction midway through profile (downstream extent of zone 3, Fig. 4.8). As a result, there is also enrichment of nitrogen far from the injection site, and even pure nitrogen vapor at the leading front of sim9 (between point O and P, Fig. 4.8). This means that the leading front of sim9 is identical to the injection composition of sim1. Thus, the most downstream portion of sim9 might exhibit behavior similar to sim1 if it were re-injected into methane hydrate.

Since chromatographic separation manifests as a sequence of compositions connected in series, we could broadly conceptualize sim2 as two stages where we first inject the 4:1 N_2:CO_2 mixture into pure water (i.e., sim9), then re-inject the effluent into methane hydrate and aqueous phases to produce results equivalent to sim1. A sequential, two-stage, simulation of this type is conceptually similar to sim2 since the compositions farthest upstream are identical in sim9 and sim2 (z^{j2}, Fig. 4.9a) and the compositions farthest downstream are identical in sim1 and sim2 ($z^{i}1$, Fig. reffig:sim2sketchb, c). Therefore, we might expect the intermediate

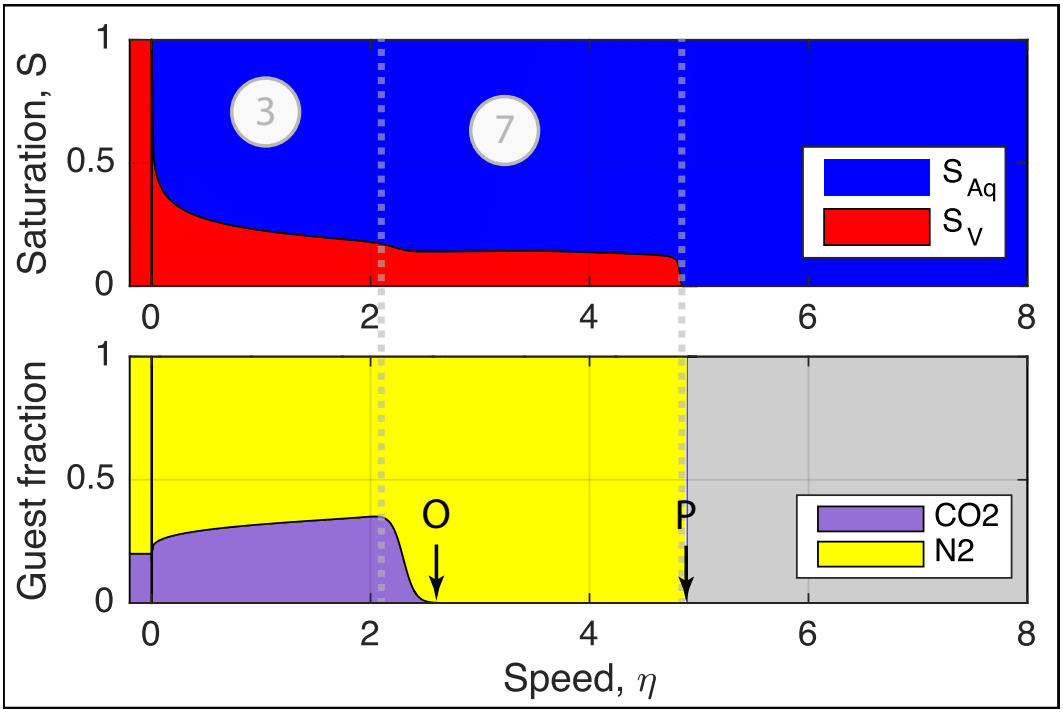

Figure 4.8: Saturation and guest mole fraction profiles for sim9 as a function of speed. Gray region in guest mole fraction profile denotes absence of guest molecules (i.e., only water is present).

phase and compositional profile between these two end-members compositions in sim2 (Fig. reffig:sim2sketchc) to look like a sequential stacking of sim9 (Fig. reffig:sim2sketcha) followed by sim1 (Fig. reffig:sim2sketchb) in which no CH_4-free mixed hydrate forms. However, this conceptual representation does not include the time/speed information of the simulations. If we do consider the speed information of the simulations, then it is possible that the profiles of sim9 and sim1 interfere and destroy intermediate portions of the compositional profiles. We hypothesize that sim1 could sequential follow sim9 without compositional interference if the following two conditions hold: 1) the speed of the leading front in sim9 (point P, Fig. 4.8, 4.9a) exceeds the speed of the dissociation front in sim1 (upstream extent of zone 1, Fig. 4.6a, 4.9b) so that a pure nitrogen vapor manifests, and 2) the speed of the dissociation front of sim1 exceeds the speed of the upstream extent of pure nitrogen vapor in sim9 (point O, Fig. 4.8, 4.9a) so that compositions containing carbon dioxide are much slower than the nitrogen-driven dissociation front of sim1 (upstream extent of zone 1, Fig. 4.6a, 4.9b). Inspection of the speed profiles in sim9 (Fig. 4.9a) and sim1 (Fig. 4.9b), show that condition #1 does hold, but condition #2 does not hold. Consequently, sim2 is not simply a sequential stacking of sim9 followed by sim1. Instead, a new zone appears in sim2 (zone 2, Fig. 3, 4.6b, 4.9c) that is slower than the dissociation front of sim1.

As a result of the compositional speed conditions outlined above, compositions containing carbon dioxide in sim9 that exceed the speed of the dissociation front in sim1 are not possible in sim2. Instead, compositions with even slower speeds manifest (zone 2, Fig. 4.3, 4.6b, 4.9c), which incidentally contain mixed hydrates composed of carbon dioxide and nitrogen. These compositions are slower than the fastest compositions that contain carbon dioxide in sim9 because hydrate is immobile, the carbon dioxide fraction in hydrate is greater than the nitrogen fraction (i.e., 5:2), and the total carbon dioxide fraction in the hydrate phase is greater than in the aqueous phase (i.e., 25:2). The combined effect is that most of the carbon dioxide in zone 2 is temporarily stranded in immobile hydrate (zone 2, Fig. 4.3, 4.6b, 4.9c) such that zone 2 in sim2 contains the largest fraction of carbon dioxide within the profile and a larger carbon dioxide fraction than any of the compositions in sim9. Therefore, we conclude that formation of mixed hydrate composed of carbon dioxide and nitrogen in sim2 is a consequence of the slow-moving methane

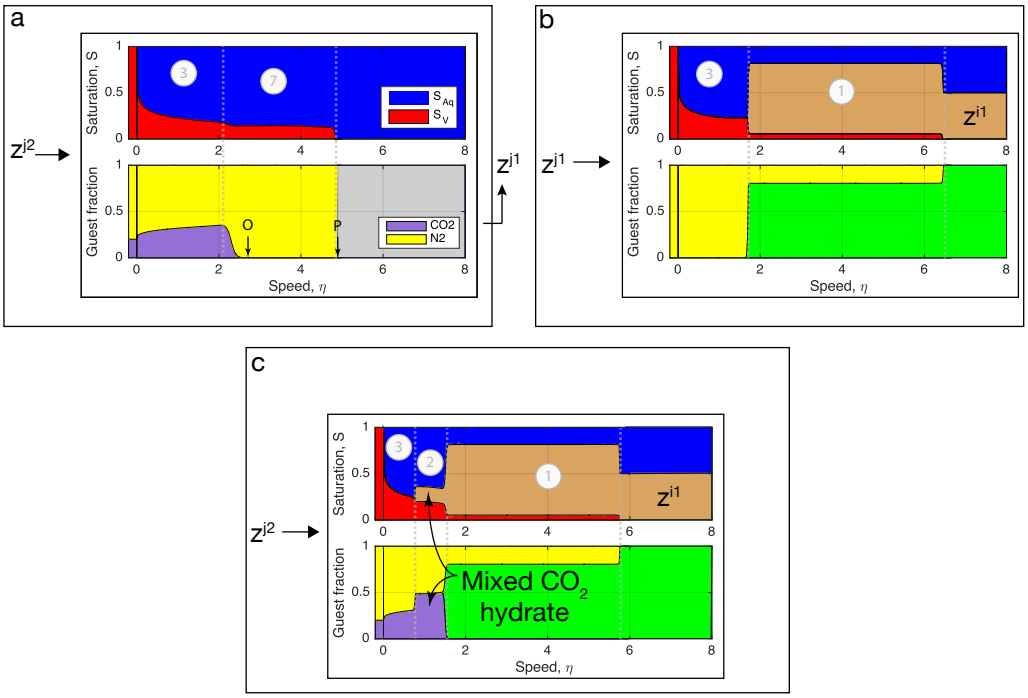

Figure 4.9: Comparison of (a) sim9, (b) sim1, and (c) sim2. Injection compositions are labeled with arrows pointing from the left of the profiles toward the profiles. Initial compositions are labeled on top of profiles where injection has not invaded.

hydrate dissociation front that allows carbon dioxide to accumulate behind the front as hydrate.

4.5.2 Implications for existing work

Our simulations show the following four behaviors that may alter the interpretation of previous work: 1) chromatographic separation of each component in mobile and immobile phases; 2) methane hydrate dissociation and downstream flow of methane vapor that is facilitated by the injection of nitrogen not carbon dioxide; 3) mixed hydrate formation composed of carbon dioxide and nitrogen that forms upstream of methane hydrate dissociation; 4) reservoir "plugging" only when free water is initially present.

From these results, we suggest a new conceptual model for “guest molecule exchange” characterized by two sequential processes that contrasts with the histor-

ical conceptual model of a single simultaneous process Ohgaki et al. (1996), Park et al. (2006). In the historical conceptual model, there is a single interface where methane exits hydrate cages and carbon dioxide and/or nitrogen simultaneously enter hydrate cages. In our new conceptual model, a nitrogen-dominated vapor destroys methane-occupied hydrate cages through dissociation and then carbon dioxide follows behind to create new hydrate cages that are occupied by carbon dioxide and nitrogen. This new conceptual model, driven by chromatographic separation, is the result of varying hydrate stabilities of each gas molecule in addition to significant compositional differences in each phase. A conceptual model similar to the one suggested here was proposed by Boswell et al. (2017) where mole-to-mole "guest molecule exchange" was replaced by an ambiguous series of processes that resulted in a "bulk exchange". Our results clarify in detail how dynamics processes might connect in series to produce such a "bulk exchange".

Our results also suggest that injection composition cannot be evaluated independently of the initial composition, since identical injection compositions (e.g., sim4 and sim8) produce drastically different reservoir behavior when the initial conditions are changed. This has been acknowledged by others Birkedal et al. (2015), Hauge et al. (2014) but has not been systematically evaluated through laboratory experiments nor numerical modeling. Yet, our finding indicates that internal reservoir dynamics are far more sensitive to the injection composition if the reservoir initially contains free water, which is the most probable initial condition for natural settings. This further implies that water-limited laboratory experiments of "guest molecule exchange" that report successful exchange under various injection compositions, including pure carbon dioxide (Park et al., 2006, Graue et al., 2008, Ersland et al., 2009), are not good representations of the field and are misleading because "plugging" is not possible under those conditions. In fact, all laboratory experiments with initial free water have required substantial co-injection of nitrogen to limit hydrate "plugging" Birkedal et al. (2015). Thus, laboratory experiments performed under water-limited initial conditions represent only a subset of the system behavior and should not be used as indicators of the field behavior.

In addition, our results indicate that "guest molecule exchange" tends to displace methane downstream and accumulate carbon dioxide near the injection. This suggests that optimal methane production and carbon dioxide storage is achieved

with constant injection at an upstream well and constant production at a second downstream well. Since Ignik Sikumi had only one well, the methane production and carbon dioxide storage might represent a lower bound because most of the methane was likely displaced farther into the reservoir and most of the carbon dioxide was close to the production well.

Finally, evidence for chromatographic separation during "guest molecule exchange" does seem to exist in other modeling studies despite a lack of explicit discussion of chromatographic separation. For example, Boswell et al. (2017) show two sets of simulated hydrate saturation and temperature profiles during injection. They show "plugging" near the injection when the injection composition is 65 mol.% N_2 and 35 mol. % CO_2, but no "plugging" when the injection composition is 77.5 mol.% N_2 and 22.5 mol.% CO_2, which agrees with the "plugging" we show only for the injection composed of 70 mol.% N_2 and 30 mol. % CO_2 (Fig. 4.6d). Furthermore, they show a finite-width transient zone of increased hydrate formation that propagates downstream over time in both cases, which agrees with the increased hydrate zones that appear in most of our simulations (zone 1, Figs. 4.3, 4.6, and 4.8). Additional comparison is not possible because Boswell et al. (2017) do not report any of the compositional changes that occur. However, White and Suk Lee (2014) present 2-dimensional simulations of the Ignik Sikumi field test that do show compositional changes. Those results exhibit depletion of methane near the injection, increased nitrogen penetration into the reservoir relative to carbon dioxide, and mixed hydrate formation with a composition that varies downstream of the injection. Those findings all agree with the simulations we presented. Therefore, our results augment these earlier simulation results to provide a fundamental description of the spatial and temporal evolution of the reservoir.

4.6 Model Limitations

Our model does not consider mass transfer by diffusion, temperature or pressure changes due to hydrate formation/dissociation, 2-dimensional flow behavior, or heterogeneous geological properties. In addition, we assume that hydrate formation/dissociation is instantaneous, which neglects rate-limiting mass transfer and/or kinetic effects. However, other models of mixed hydrates that do

include these effects show results that our qualitatively similarly to ours. This implies that none of the physics we exclude would completely eliminate the reservoir dynamics we show. Instead, they would likely be superimposed onto our results to reduce or increase the speed of the fronts we show or smear the sharpness of the fronts to create smoother gradients in the phase compositions.

4.7 Design for laboratory experiments

We suggest validation of our results by a series of flow-through experiments where in-situ Micro-Raman measures the change in composition of hydrate and vapor phases and a Micro CT-scanner evaluates the bulk phase changes. This type of experimental apparatus is the only way to understand how composition affects hydrate stability and whether or not equilibrium thermodynamics is valid during fluid flow past hydrate phases.

4.8 Implications for other mixed hydrate systems

Our results show chromatographic separation of multiple hydrate-forming components during multi-phase flow that may apply to other hydrate-forming systems. In particular, we expect similar behavior to occur for systems in which at least one component is hydrate unstable such as natural systems composed of multiple hydrocarbons. In natural marine sedimentary systems, temperature and pressure increase with depth so all hydrates are eventually unstable below some depth. However, each component and, therefore, each mixture has a different depth where this transition occurs. For a system composed of water, methane, and ethane, ethane hydrate is stable at depths where it is too deep to stabilize methane hydrate. However, mixed hydrates of methane and ethane are conditionally stable at depths below the methane hydrate stability zone and above the ethane hydrate stability zone. Gas mixtures composed of methane and ethane would likely originate far below the hydrate stability zone of either component but may ascend under buoyancy into the hydrate stability zone. Thus, the ascending gas mixtures would first encounter the ethane hydrate stability zone before the methane hydrate stability zone. This progressive transport through different

hydrate stability zones may explain the depth-dependent hydrate composition observed in sediment cores recovered offshore NW Borneo (Paganoni et al., 2016) that display increasing ethane and heavier hydrocarbon with depth. Our model could be adapted to a system composed of hydrocarbons to understand how compositional changes during multiphase flow lead to chromatographic separation. The first order physics leading to chromatographic separation would likely manifest in a framework identical to the one we show here where flow is 1-d, horizontal and the phase behavior is assumed to be isothermal and isobaric. Direct comparison with field observations would require vertical flow along pressure and temperature gradients and may also require non-isothermal, non-isobaric phase behavior. Yet, the non-isothermal, non-isobaric phase behavior could be approximated as a series of connected depth-dependent isothermal, isobaric phase diagrams.

4.9 Conclusions

We show that nitrogen drives chromatographic separation when injected into methane hydrate-bearing sediments. This chromatographic separation illuminates the mechanism that enhances guest molecule exchange when compared to pure carbon dioxide injections. In particular, the hydrate de-stabilizing effect of nitrogen and its strong partitioning in the vapor phase create a fast pathway for nitrogen to transit through the domain and dissociate the initial methane hydrate. When injected with carbon dioxide, nitrogen and carbon dioxide form a mixed hydrate of low saturation in a front that follows the nitrogen-driven dissociation. In contrast, injection compositions within the hydrate stability zone, like pure carbon dioxide or carbon dioxide-rich mixtures, form hydrate of high saturations near the injection point that have the potential to completely block flow. However, this specific behavior is only possible when there is free water initially in the domain. These results provide insight into the reservoir dynamics during the Ignik Sikumi field test and suggest that additional field scale tests could be enhanced with a two-well design, instead of the single well design used at Ignik Sikumi.

Our results additionally highlight the difference in behavior that occurs when free water is or is not initially present in the reservoir. Reservoirs with initial free water have the potential to block flow, whereas reservoirs without initial free

water do not. Thus, it is necessary to carefully constrain the injection composition when free water is initially present, but far less important when free water is not initially present. For this reason, laboratory experiments must closely match field conditions to be meaningful or predictive.

Chromatographic separation during injection into hydrate-bearing sediments may be applicable to other physical settings beyond guest molecule exchange, but additional laboratory work is necessary to validate our findings. We suggest validation of our findings by flow-through experiments where the composition is continuously measured and the interior domain is continuously monitored with micro-CT and micro-Raman to evaluate the phase and compositional profiles throughout the domain. These experiments can demonstrate whether or not chromatographic separation does indeed occur and whether or not there are any mass transfer limitations that violate the assumptions of equilibrium thermodynamics.

Our modeling framework is general and can be re-formulated to investigate the dynamic evolution of other multi-component hydrate-forming systems such as the buoyant ascent of thermogenic gas in marine sediments. During ascent, thermogenic gas would pass through multiple hydrate stability zones in which each component would form hydrate at different depths. The net consequence would be a gradient in hydrate composition with the heaviest hydrocarbons at the deepest depths. While the actual geological setting exists within pressure and temperature gradients, simple 1-d, horizontal flow like the results we present here could provide a first-order control on the expected chromatographic behavior.

Appendix A

Supplemental material for Chapter 2

We derive the analytical model discussed in the Chapter 2 (A.1), compare the sensitivity analysis of the analytical model to the multiphase model (A.2), and discuss the Skarke et al. (2014) seep analysis (A.3).

We provide a summary table of the simulations discussed in the paper (Table A.3), a table of model parameters used in the multiphase fluid flow simulations A.3. Tabulated output from our seep analysis can be found in Darnell and Flemings (2015).

A.1 Analytical model derivation

In Chapter 2, we described an analytical model to account for the hydrate threshold that produces transient venting. Our derivation is provided below.

S_w, S_h, and S_g are volumetric pore space saturations of water, hydrate and gas. We assume no gas is present before or after warming, so $S_g = 0$. Thus,

$$S_w + S_h = 1 \tag{A.1}$$

We compare the initial thermal state (B_i) with the warmed or final state (B_f). Superscripts (i or f) will be used to denote the thermal state for the other variables.

We also assume no hydrate is initially present above B_f, and that all hydrate below B_f dissociates during warming. We express this as follows:

$$S_h^{(i)} = \begin{cases} 0, & z < B_f, \\ 1 - S_w^{(i)}, & B_f \leq z \leq B_i, \\ 0, & z > B_i. \end{cases} \tag{A.2}$$

$$S_h^{(f)} = 0, \text{ if } z > B_f \tag{A.3}$$

We define the salinity in the water (c) as the following:

$$c = \frac{M_{salt}}{\phi \rho_w S_w V} \tag{A.4}$$

where ϕ is porosity, ρ_w is water density, V is volume of a grid cell, and M_{salt} is the mass of salt within the grid cell. The saturations of water and hydrate are similarly defined as such:

$$S_w = \frac{V_w}{\phi V} \tag{A.5}$$

$$S_h = \frac{V_h}{\phi V} \tag{A.6}$$

The change in hydrate saturation and salinity between thermal states is:

$$\Delta S_h = S_h^{(f)} - S_h^{(i)} \tag{A.7}$$

$$\Delta c = c^{(f)} - c^{(i)} \text{ where } c^{(i)} = 3.5 \text{ wt. \%} \tag{A.8}$$

And, since $S_h^{(i)} = 0$ where $z < B_f$,

$$\Delta S_h = S_h^{(f)} \text{ for } z < B_f \tag{A.9}$$

We combine equations (4-8), and solve for the change in salinity.

$$\Delta c = \frac{M_{salt}}{\phi \rho_w V} \left(\frac{1}{S_w^{(f)}} - \frac{1}{S_w^{(i)}} \right) = c^{(i)} \left(\frac{S_w^{(i)}}{S_w^{(f)}} - 1 \right) \tag{A.10}$$

And since, $S_w^{(i)} = 1$ for $z < B_f$,

$$\Delta c = c^{(i)} \left(\frac{1}{1 - S_h^{(f)}} - 1 \right) \text{ for } z < B_f \tag{A.11}$$

The change in salinity required to achieve three-phase equilibrium at the final state (c^{eq}) is:

$$\Delta(c^{eq}) = c^{eq} - c^{(i)} \tag{A.12}$$

Now, we set the salinity change to be the salinity change required for three-phase

equilibrium as follows:

$$\Delta c = \Delta(c^{eq}) \tag{A.13}$$

We combine equations (11-13) and solve for the final hydrate saturation, which we call the hydrate saturation required for three-phase equilibrium (S_h^{eq}).

$$S_h^{eq} = S_h^{(f)} = 1 - c^{(i)}/c^{eq} \tag{A.14}$$

If we integrate this hydrate saturation within the final GHSZ ($0 < z < B_f$), we have the total additional hydrate required to produce *transient venting*. In the main text, we call this parameter γ. We then compare γ with the available hydrate that dissociates due to warming (β).

A.2 Comparison of analytical and dynamic, multiphase models

We compare the sensitivity analysis of the analytical model (Fig. 2.5) to results from the multiphase simulation. We show three additional simulations. The model parameters of the first simulation (Fig. A.1b) are identical to the example of the main text except hydrate saturation has been decreased from 10% of the pore volume to 5% of the pore volume. This decrease in hydrate saturation does not produce venting as suggested from our sensitivity analysis. We then decrease the water depth by 10 meters (Fig. A.1a) and increase the seafloor warming by 0.2 °C (Fig. A.1c). Both of these small variations in model parameters produce *transient venting*.

A.3 Analysis of seeps

Skarke et al. (2014) provides water depth and geographical location for each seep in their database. We use the CTD cast collection downloaded from the World Ocean Database (Levitus et al., 1998) to calculate the bottom water temperature for each seep. We calculate the bottom water temperature of each seep as follows:

1. We select all CTD casts where the terminal water depth of the CTD is at least as deep as the seep.

2. We locate the three CTD casts closest to the seep.

3. We use all three CTD casts for analysis unless, (i) a CTD cast is further than 100 km from the seep, or (ii) the mean difference in temperature between the closest and 2nd or 3rd closest CTD cast is greater than 4 ∘C (see *Note 1* below). At a minimum, we use the closest CTD cast for analysis.

4. We linearly interpolate the CTD casts to uniform, 1-meter grids.

5. We average the set of CTD casts on the uniform grid.

6. We fit the output of averaging using a piecewise cubic interpolation.

7. We find the temperature of the fitted data at the water depth of the seep.

These results are shown in Darnell and Flemings (2015), along with the water depths and geographical locations given by Skarke et al. (2014). CTD casts were 16 km from the seep on average with a standard deviation of 27 km.

We determine hydrate stability using the method of Flemings et al. (2006), Liu and Flemings (2007). The stability condition occurs when the solubility of methane in liquid water and hydrate (Duan et al., 1992) equals the solubility of methane in liquid water and free gas (Henry et al., 1999). We specifically solve for the temperature given pressure and salinity. We set salinity to 3.5 wt. % and pressure to the hydrostatic pressure using the water depth of the seep ($\rho = 1030$ kg m^{-3}). This method compares well with other hydrate stability calculations (Sloan, 1998, Flemings et al., 2006, Liu and Flemings, 2007).

Note 1: Phrampus and Hornbach (2012) identified Atlantic Ocean and Gulf Stream thermoclines along the Atlantic Margin. We do not average CTD casts if casts appear to represent different thermoclines. Instead, we simply take the closest CTD casts from a single thermocline.

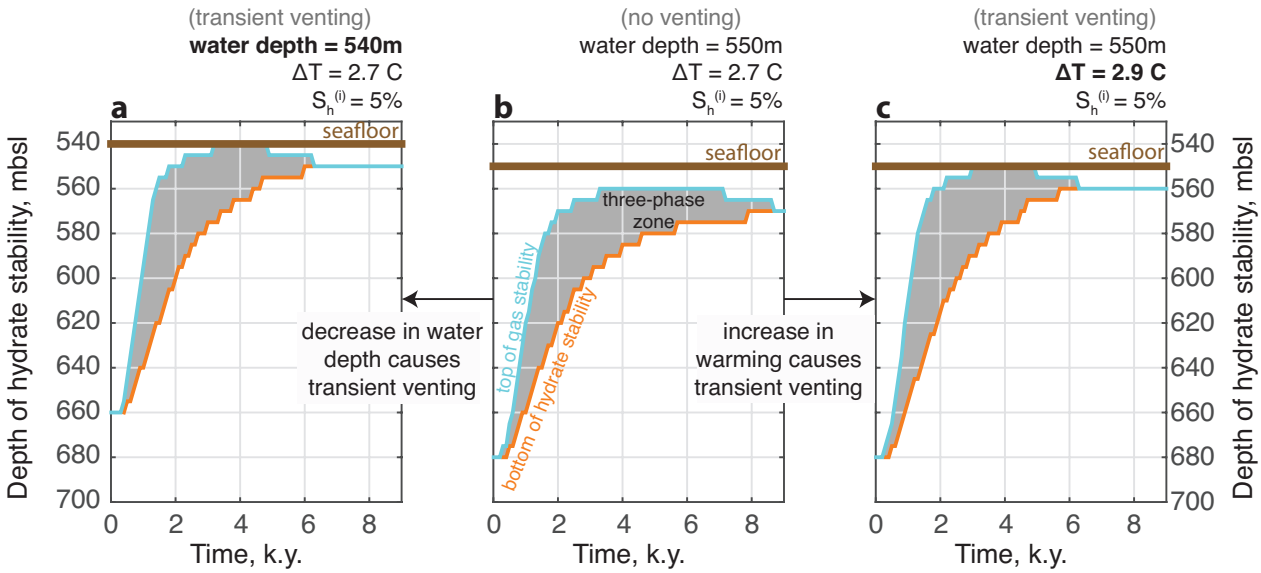

Figure A.1: Comparison of multiphase dynamic simulation for initial hydrate saturation of $S_h^{(i)} = 5\%$ with small variations in model parameters. For all three panels, the temperature gradient (40 °C/km) and initial seafloor temperature (3 °C) are held constant. Middle panel (b) is the base case. (a) Trajectory of hydrate/gas stability as a function of time where the water depth has been decreased by 10 meters from (b). For complete simulation, see movie (Darnell and Flemings, 2015). (b) Trajectory of hydrate/gas as function of time where all parameters are equal to the example in the main text, except $S_h^{(i)}$ has been decreased from 10% of pore volume to 5%. The gray area is the three-phase zone, which is located between the top of gas stability (cyan line) and bottom of hydrate stability (orange line). For complete simulation, see movie (Darnell and Flemings, 2015). (c) Trajectory of hydrate/gas stability as a function of time where the temperature has been increased 0.2 °C from (b). For complete simulation, see movie S4 (Darnell and Flemings, 2015).

Table A.1: Simulation details and outcome

Water depth, mbsl	Hydrate sat., %	Temp. increase,°C	Outcome	Fraction Vented	Figure
550	10	0.5	no venting[1]	0	–
550	10	1.0	no venting[1]	0	–
550	10	2.2	no venting[1]	0	–
550	10	2.5	no venting[1]	0	–
550	10	2.6	transient venting[1]	>0	–
550	10	2.7	transient venting[1]	0.01	Figs. 2.1-2.5
550	10	2.8	transient venting[1]	0.10	Fig. 2.4
550	10	2.9	transient venting[1]	0.27	Fig. 2.4
550	10	3.0	transient venting[1]	0.49	Fig. 2.4
550	10	3.2	complete venting[1]	0.81[5]	–
550	10	5.0	complete venting[1]	0.81[5]	–
800	10	5.8	transient venting[2]	0.03	Fig. 2.4
1000	10	7.8	transient venting[3]	0.02	Fig. 2.4
550	5	2.7	no venting[1]	0	Fig. A.1
540	5	2.7	transient venting[4]	0.06	Fig. A.1
550	5	2.9	transient venting[1]	0.12	Fig. A.1

[1] Hydrate stability zone vanishes at 3.14 °C increase.
[2] Hydrate stability zone vanishes at 6.91 °C increase.
[3] Hydrate stability zone vanishes at 9.09 °C increase.
[4] Hydrate stability zone vanishes at 2.95 °C increase.
[5] All hydrate vanishes, but gas is left behind as residual gas and dissolved gas.

Table A.2: Parameters used in dynamic simulation

Symbol	Parameter	Value [Unit]	Reference
c_g	Heat capacity of methane gas	3500 [J K^{-1} kg^{-1}]	(Liu and Flemings, 2007)
c_h	Heat capacity of hydrate	2100 [J K^{-1} kg^{-1}]	(Liu and Flemings, 2007)
c_s	Heat capacity of grains	1381 [J K^{-1} kg^{-1}]	(Liu and Flemings, 2007)
c_w	Heat capacity of water	4200 [J K^{-1} kg^{-1}]	(Liu and Flemings, 2007)
D_{10}^m	Diffusion coefficient of methane	10^{-9} [m^2 s^{-1}]	(Davie and Buffett, 2001)
D_{10}^s	Diffusion coefficient of salt	10^{-9} [m^2 s^{-1}]	(Davie and Buffett, 2001)
F_b^m	Basal methane flux	0 [kg m^2 yr^{-1}]	–
F_b^t	Basal heat flux	40 [mW m^{-2}]	–
g	Gravitational acceleration	9.81 [m s^{-2}]	–
k	Permeability in absence of hydrate	10^{-15} [m^2]	–
L	Latent heat of hydrate crystallization	421 [kJ kg^{-1}]	(Cathles and Chen, 2004)
n_g	Corey exponent (gas)	2	(Bear, 1972, Liu and Flemings, 2007)
n_w	Corey exponent (water)	4	(Bear, 1972, Liu and Flemings, 2007)
S_{rg}	Irreducible gas saturation	0.02	(Liu and Flemings, 2007, Yousif et al., 1991)
S_{rw}	Irreducible water saturation	0.1	(Liu and Flemings, 2007, Yousif et al., 1991)
λ_g	Thermal conductivity of gas	0.03 [W m^{-1} K^{-1}]	(Sloan, 1998)
λ_h	Thermal conductivity of hydrate	0.5 [W m^{-1} K^{-1}]	(Sloan, 1998)
λ_w	Thermal conductivity of water	0.6 [W m^{-1} K^{-1}]	(Sloan, 1998)
λ_s	Thermal conductivity of grains	1.6 [W m^{-1} K^{-1}]	(Class et al., 2002)
μ_g	Viscosity of gas	P- and T-dependent	(Class et al., 2002)
μ_w	Viscosity of water	P- and T-dependent	(Class et al., 2002)
ρ_g	Density of methane	P- and T-dependent	(Duan et al., 1992)
ρ_w	Density of water	T- and salinity-dependent	(Duan et al., 1992)
ρ_h	Density of hydrate	912 [kg m^{-3}]	(Sloan, 1998)
ρ_s	Density of grains	2650 [kg m^{-3}]	–
ϕ	Porosity in absence of hydrate	0.5	Estimated from Flemings et al. (2006)
θ	Tortuosity	2	Calcualted from porosity (Torres et al., 2004)

Appendix B

Supplemental material for Chapter 3

In this appendix, we include a summary of relevant experimental work (B.1), a comparison between our calculations and CSMGem (B.2), a brief description of compositional phase diagrams (B.3), and additional phase diagrams at various pressures and temperatures (B.4).

B.1 Summary of relevant experimental work

In Chapter 3, we presented a pressure-temperature phase diagram (Fig. 3.1) and indicated several studies performed at pressures and temperatures relevant for our work. Table B.1 summarizes those other studies.

B.2 Comparison of thermodynamic simulations with CSMGem

The Colorado School of Mines: Gibbs energy minimization program (CSMGem) is a widely-used thermodynamic simulator that predicts hydrate stability for mixed and simple hydrates (Ballard and Sloan, 2004b). We base our calculations on the computational framework that comprises CSMGem (Sloan Jr and Koh, 2007, Ballard and Sloan, 2004a). However, we take the analysis further by constructing ternary and quaternary phase diagrams. Since our calculations use a framework similar to CSMGem, we compare our calculations with CSMGem at a few select points. First, we compare our calculations at 50 bar, 4 °C (Tables B.2,) to validate the existence of key components in our diagrams. We demonstrate that three-phase equilibrium of (L-H-V and Aq-H-V) exists for both calculations and that the phase-wise compositions are nearly identical. Second, we compare hydrate stability curves for CH_4 hydrate (Fig. B.1), CO_2 hydrate (Fig. B.2), and N_2 hydrate (Fig. B.3). The code used to perform all flash calculations is available for download at https://github.com/kdarnell/hydrateflash.

Table B.1: Summary of experimental conditions applicable to this study.

Label	P (bar)	T (°C)	Environment	Study
a	85	4	Ignik Sikumi, Alaska, USA	(Birkedal et al., 2015)
b	96.6	4	Ignik Sikumi, Alaska, USA	LBNL Report
c	82.7	2	Ignik Sikumi, Alaska, USA	(Yonkofski et al., 2016)
d	70	4.85	Alaska, USA	(Kang et al., 2014)
e	120	1	n/a	(Park et al., 2006)
f	95	0.85	n/a	(Youn et al., 2016)
g	200	15	East Sea, Korea (UBGH site)	(Kang et al., 2014)
h	100	13.85	Nankai Trough, Japan (NGH site)	(Kang et al., 2014)

Table B.2: Feed descriptions used in Table S3 for CSMGem comparison.

Feed No.	z_{H_2O} (w)	z_{CH_4} (m)	z_{CO_2} (c)	z_{N_2} (n)
1	0.5	0	0.5	0
2	0.95	0	0.05	0
3	0.92	0.08	0	0
4	0.5	0.5	0	0
5	0.98	0.01	0.01	0
6	0.5	0.25	0.25	0
7	0.2	0.08	0.72	0
8	0.5	0.25	0	0.25
9	0.5	0	0.45	0.05
10	0.9	0	0.07	0.03
11	0.9	0.03	0.03	0.04

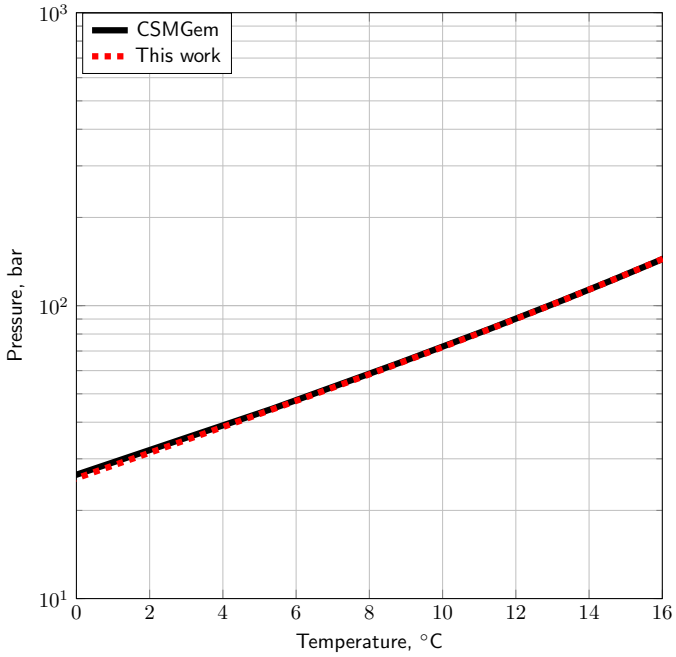

Figure B.1: Pressure-Temperature CH_4 hydrate stability curve comparison with CSMGem.

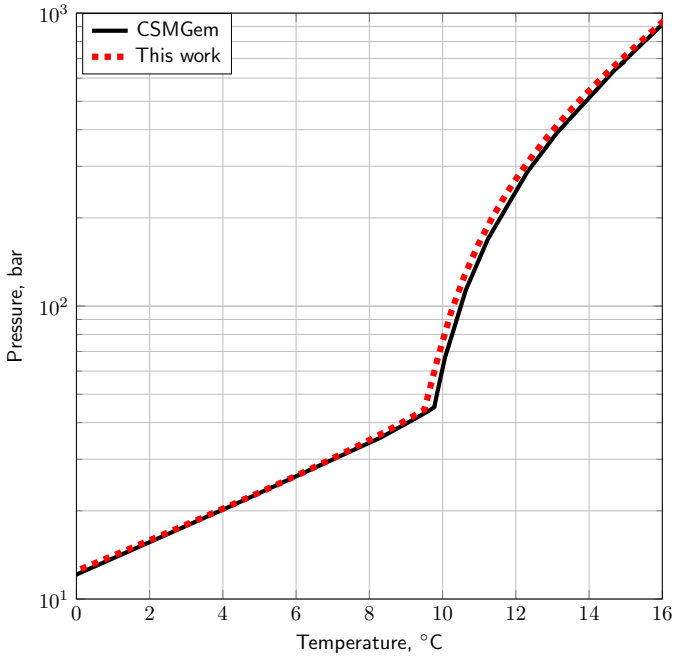

Figure B.2: Pressure-Temperature CO_2 hydrate stability curve comparison with CSMGem.

B.3 Note on compositional ternary diagrams

At a certain pressure and temperature, the phase diagram of a mixture as a function of composition can be shown in ternary (3 component) and quaternary (4 component) diagrams (Orr, 2007, Walas, 2013). For this hydrate system, the ternary and quaternary phase diagrams have multiple zones of one-, two-, and three-phase stability. Single phase regions occur near vertices, edges, and planes, where one or more of the components vanish. Two-phase regions are indicated by families of tie lines. A overall composition falling on a tie line produces two distinct phases with each phase composition represented by the end points of the tie line. The phase fraction is then measured by the lever rule where the fractional distance along the tie line between one end point and the overall composition is linearly proportional to the molar phase fraction (Orr, 2007, Walas, 2013). Three-phase regions are represented by (shaded or unshaded) tie triangles where the composition of each phase is fixed (as a result of Gibbs Phase Rule) at the end-points of the triangle. A two-dimensional lever rule holds for the molar phase fraction within the tie triangle.

B.4 Additional compositional phase diagrams

In Chapter 3, we focused on two thermodynamic conditions: 1) 50 bar and 4 °C (Figs. 3.2,3.3) and 2) 70 bar and 4 °C (Fig. 3.4). Here we supplement our analysis with additional phase diagrams. Furthermore, we highlight the differences in phase composition between hydrate and vapor using pseudo-ternary diagrams, which we describe below.

B.4.1 Pseudo-ternary diagrams

We translate the three-phase equilibrium compositions within the quaternary diagram into a guest-only compositional space called pseudo-ternary diagrams. These pseudo-ternary diagrams show the co-existing hydrate (orange lines, Figs. B.4,B.5) and vapor (red lines, Figs. B.4,B.5) compositions at three-phase equilibrium (Aq-H-V) on the same ternary plot. We construct these diagrams by subtracting out the H_2O fraction and re-normalizing each phase composition by the re-

maining (*i.e.*, guest-only) components. We choose a guest-only plot to enhance the intricacies of the hydrate phase composition that are difficult to see on the quaternary diagram and because each phase has a nearly constant H_2O fraction. Therefore, the pseudo-ternary diagram is equivalent to a superimposed cross-section through H_2O compositions of ≈0 mol.% for the vapor phase and ≈86 mol.% for the hydrate phase. We could make similar diagrams for the other two surfaces of the Aq-H-V zone, but choose this surface because it highlights the dramatic difference in N_2 fraction between the phases.

These diagrams show the difference in phase compositions at three-phase equilibrium and mark the boundary between hydrate stable and hydrate unstable regions. Co-existing phase compositions are connected by the tie triangle edges (thin, black lines, Figs. 3.2), and these two phases are also connected to an aqueous phase composition (thin, black lines, Fig. 3.2b-c) that is not drawn in the pseudo-ternary diagrams. The hydrate phase is preferentially enriched in CO_2 relative to the vapor phase, while the vapor is preferentially enriched in N_2. The position of the vapor guest-only composition marks a separation between zones of hydrate stability. Guest-only compositions above the vapor line (*i.e.*, larger N_2 fraction), will not be hydrate stable at any H_2O fraction, whereas compositions below this line (*i.e.*, smaller N_2 fraction) may be hydrate stable depending on the H_2O fraction.

Note that since these pseudo-ternary diagrams are two separate, superimposed cross-sections, they do not represent absolute boundaries of the Aq-H-V zone at a particular H_2O fraction. Instead, the boundaries of the Aq-H-V zone at a particular H_2O fraction will shift and expand as a function of the H_2O fraction. The extent of the boundaries will increase to a maximum near a H_2O fraction of 86 mol.% and will decrease to a very thin zone near H_2O fractions of 0 mol.% and 100 mol.%. This is analogous to the tie triangles shown in Figures 2-3 where the width of the three-phase zones is greatest at H_2O fractions near the hydrate composition (86 mol.%), but vanish to a point at H_2O fractions of 0 mol.% and 100 mol.%. One consequences of this shifting three-phase zone is that guest-only compositions below the vapor guest-only composition of the Aq-H-V zone may or may not be hydrate stable. However, guest-only compositions, regardless of H_2O fraction, above the vapor guest-only composition will be hydrate unstable.

B.4.2 Pressure and temperature variations

We investigate the pressure and temperature dependencies of the Aq-H-V zone using a few quaternary diagrams (Fig. B.4) and a P-T matrix of the pseudo-ternary diagram (Fig. B.5). Since the vapor guest-only composition (red line, Figs. B.4, B.5) marks the compositions where hydrate is never stable (*i.e.,* above red, vapor composition line), the most useful attribute of the pseudo-ternary diagrams is the position of the vapor guest-only composition. At high temperatures and low pressures (*e.g.,* lower right, Fig. B.5), the vapor guest-only composition approaches the CO_2 vertex, so guest-only compositions with sufficient CH_4 and/or N_2 destabilize hydrate. This is only true when simple CH_4 hydrate is also hydrate unstable. At low temperatures and high pressures (*e.g.,* upper left, Fig. B.5), the vapor guest-only composition approaches the pure N_2 vertex, so most guest-only compositions are hydrate stable except compositions with very high N_2 fractions. At thermodynamic condition where simple CH_4 hydrate is stable, hydrate is stable at compositions consisting of any CO_2 and CH_4 mixture, but is unstable at compositions exceeding a pressure- and temperature-dependent N_2 threshold. For example, at 90 bar and 2 C (upper left, Fig. B.5), hydrate is unstable at N_2 fraction above $\approx$90 mol.% for any guest-only mixture of CH_4 and CO_2, but this threshold decreases to $\approx$80 mol.% as the CO_2 fraction in the guest-only mixture decreases. Below this threshold, hydrate may be stable depending on the H_2O fraction.

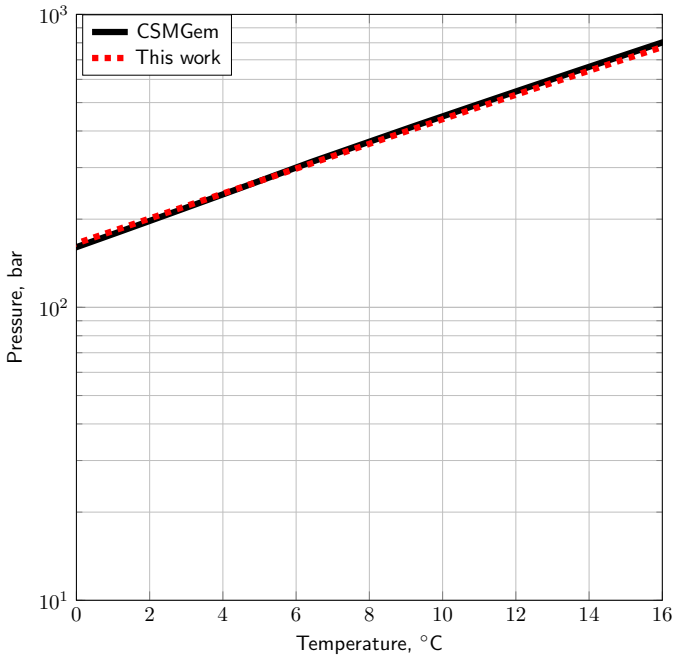

Figure B.3: Pressure-Temperature N_2 hydrate stability curve comparison with CSMGem.

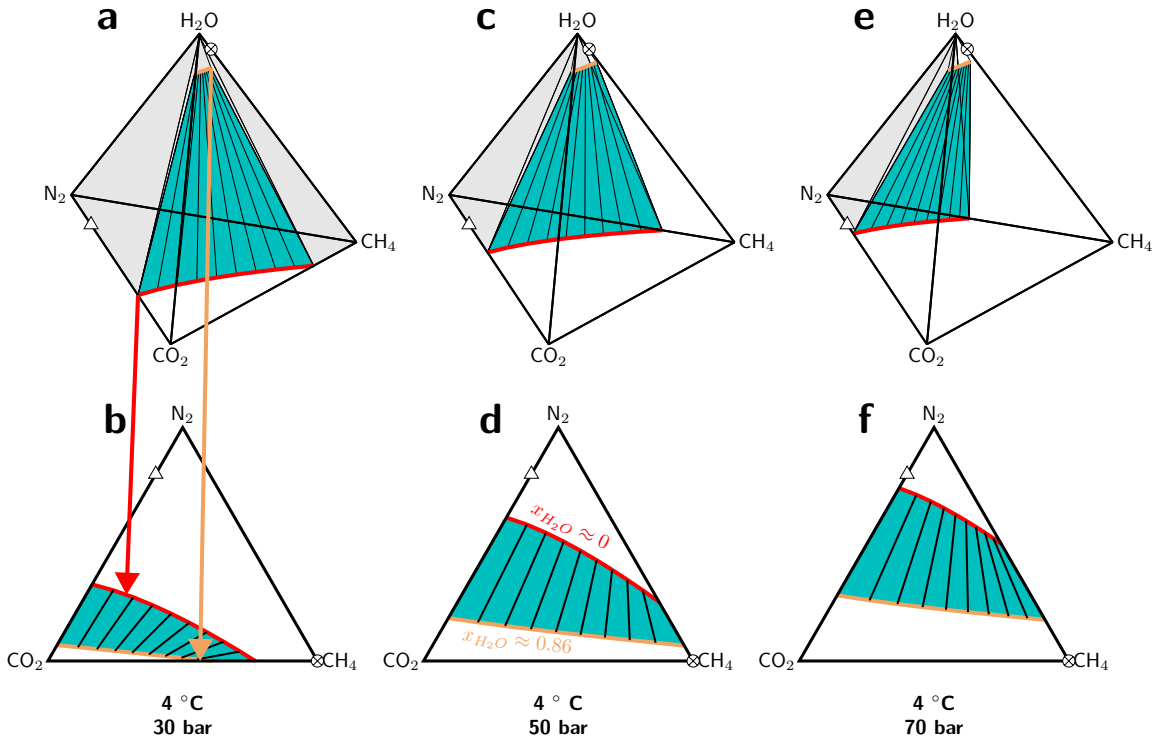

Figure B.4: Variation in three-phase zone as a function of pressure (white diamonds, Fig. 3.1) using quaternary diagrams (a,c,e) and pseudo-ternary diagrams of the normalized guest-only compositions. Top panels (a,c,e) show three-phase zone and hydrate unstable zone within quaternary diagram. Bounding lines, tie lines, and markers are drawn as they are drawn in Figure 3. The interior surface of the three-phase zone connecting the hydrate phase to the vapor phase is shaded in teal. Bottom panels (b,d,f) show ternary diagram of only the guests such that the H_2O fraction is subtracted and the guest composition is normalized by the non-H_2O fraction. The diagram shows the superimposed guest-only composition of hydrate (orange line) and vapor (red line) at three-phase equilibrium. These pseudo-ternary diagrams are not a cross-section of the quaternary diagram since each phase has a different H_2O mole fraction such that the hydrate phase is ≈86 mol.% H_2O and the vapor phase is ≈0 mol.% H_2O, which is true for all presented pseudo-ternary diagrams not just where it is labeled on (d). a-b) Phase diagrams at 4 °C and 30 bar. Arrows show that vapor (red line) and hydrate (orange) compositions appear in both the quaternary and pseudo-ternary diagrams. c-d) Phase diagrams at 4 °C and 50 bar. e-f) Phase diagrams at 4 °C and 70 bar.

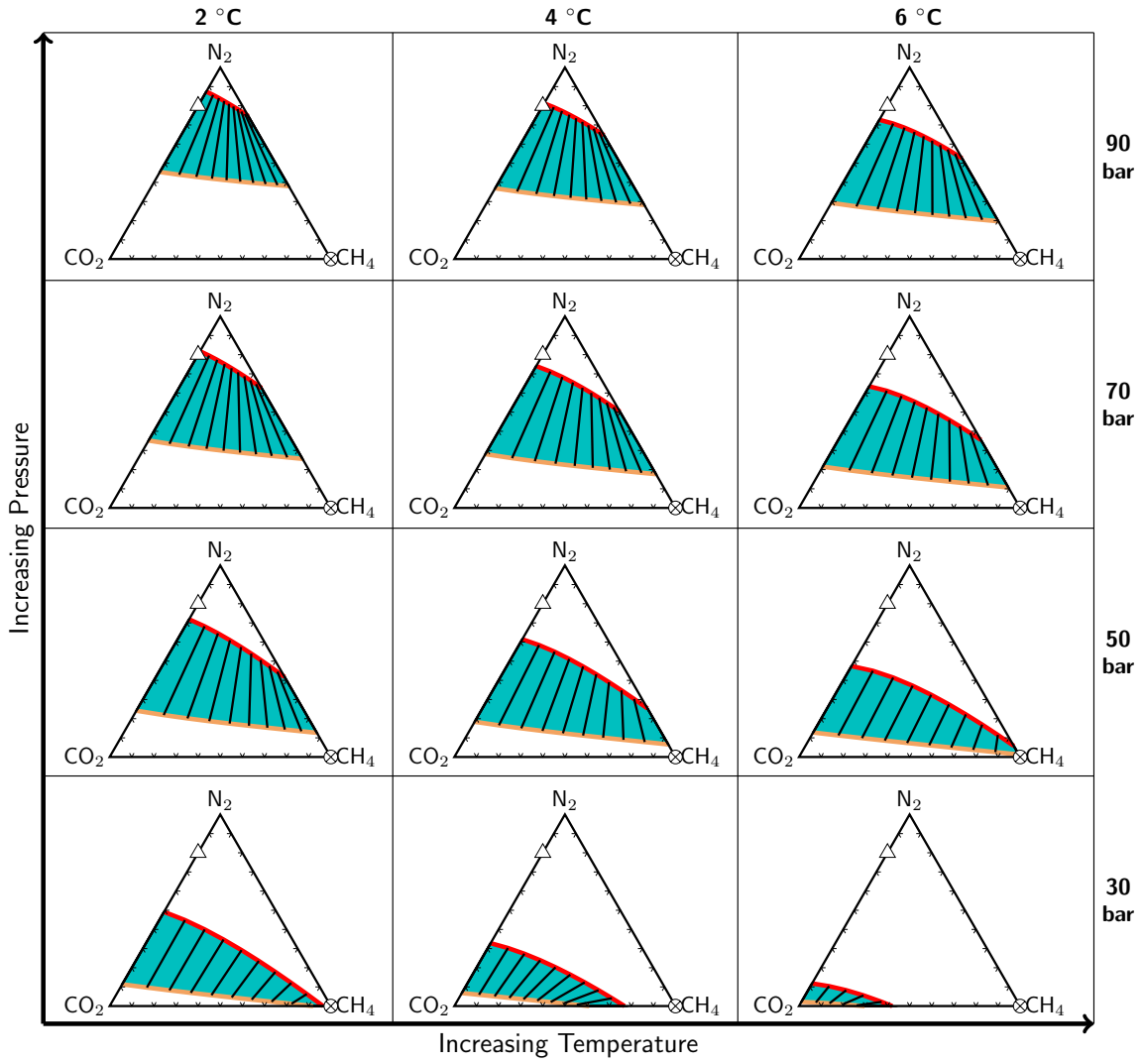

Figure B.5: Matrix of pseudo-ternary diagrams as a function of pressure and temperature (green squares, Fig. 3.1). Pseudo-ternary diagrams show the normalized guest-only vapor (red line) and hydrate (orange line) compositions along the H-V surface of the three-phase zone (shaded in teal). A few tie triangle edges are drawn for reference. Hydrate is unstable above vapor line at all H_2O fractions and stable depending on H_2O fraction below vapor line.

Appendix C

Supplemental material for Chapter 4

C.1 Tie line and tie triangle computations for compositional phase diagrams

In Chapter 4, we simulate the phase stability of water, methane, carbon dioxide, and nitrogen mixtures at 70 bar, 4°C using a pre-computed compositional phase diagram in conjunction with quick interpolation methods. In this phase space, four phases our possible, which we define as an aqueous phase (Aq), a vapor phase (V), a hydrate phase (H), and a liquid carbon dioxide phase (L). However, we restrict the calculations to the sub-space where liquid carbon dioxide is not stable.

We define a composition using the vector

$$\mathbf{z} = \left[z_{\mathrm{H_2O}}, z_{\mathrm{CH_4}}, z_{\mathrm{CO_2}}, z_{\mathrm{N_2}}\right]^T = \left[z_1, z_2, z_3, z_4\right]^T . \tag{C.1}$$

We refer to the descriptive subscripts when discussing special features, but we refer to the numbered subscripts when writing equations.

We define a phase-specific composition using the vector

$$\mathbf{x}_j = \left[x_{\mathrm{H_2O},j}, x_{\mathrm{CH_4},j}, x_{\mathrm{CO_2},j}, x_{\mathrm{N_2},j}\right]^T = \left[x_{1,j}, x_{2,j}, z_{3,j}, z_{4,j}\right]^T \tag{C.2}$$

where j refers to a phase which comprises the set $j \in \{Aq, V, H\}$. We then refer to the matrix of phase compositions as $x_{i,j}$ to denote the composition of component i in phase j. We similarly number the phases when convenient, but there is not a direct correspondence between the phases and a set of numbers.

Our pre-computed compositional diagram includes sufficient points in the compositional space to define 6 unique phase regions numbered according to the phases that are stable as the following (1) Aq, (2) V, (3) Aq-V, (4) Aq-H, (5) H-V, (6) Aq-H-V.

Region 1 occurs where all guest components can be dissolved in the aqueous phase, which typically occurs when $z_{\mathrm{H_2O}} \approx 1$. The aqueous phase composi-

tions in region 3, region 5, and region 6 are used to evaluate the stability of only an aqueous phase.

Region 2 occurs where all components are in the vapor phase, which typically occurs when $z_{\mathrm{H_2O}} \approx 0$. The vapor phase compositions in region 3, region 4, and region 6 are used to determine if only a vapor phase is stable.

Region 3 occurs where the components partition into an aqueous phase and a vapor phase, which typically occurs when $z_{\mathrm{N_2}}/(1 - z_{\mathrm{H_2O}}) > 0.75$. This region is defined by a family of tie lines, so all the tie lines in this region are used to determine the composition and stability of the aqueous and vapor phases.

Region 4 occurs where the components partition into an aqueous phase and a hydrate phase, which only occurs when $z_{\mathrm{H_2O}} > 0.84$ and when $z_{\mathrm{N_2}}/(1 - z_{\mathrm{H_2O}}) < 0.75$. This region is defined by a family of tie lines, so all the tie lines in this region are used to determine the composition and stability of the aqueous and hydrate phases.

Region 5 occurs where the components partition into a hydrate phase and a vapor phase, which only occurs when $z_{\mathrm{H_2O}} < 0.84$ and when $z_{\mathrm{N_2}}/(1 - z_{\mathrm{H_2O}}) < 0.75$. This region is defined by a family of tie lines, so all the tie lines in this region are used to determine the composition and stability of the hydrate and vapor phases.

Region 6 occurs where the components partition into an aqueous phase, a hydrate phase, and a vapor phase, which in a finite width region spanning from the H_2O-CH_4-N_2 and H_2O-CO_2-N_2 exterior faces of the quaternary compositional phase diagram. This region is situated between region 3, region 4, and region5. This region is defined by a family of tie triangles, so all the tie triangles in this region are used to determine the composition and stability of the aqueous, hydrate, and vapor phases.

In the two-phase regions, we determine the potential composition of the stable phases, $x_{i,j}$, using a distance-weighted interpolation where the distance is measured between a queried composition, $\mathbf{z}^q$, and the projected point onto each tie-line, $\mathbf{z}^p$, where $\mathbf{z}^{p,k}$ defines all projected compositions for k total tie lines. We define the composition of each tie line as $x^l_{i,j}$ for i components and j phases, $x^{l,k}_{i,j}$ defines all tie line compositions. We formally define the distance, d^k, from the

queried point to the projected point on each of the k tie lines as

$$d^k(\mathbf{z}^q) = \sqrt{\sum_{ic}\left[z^q_{ic} - x^{l,k}_{ic,1} - \frac{\sum_c (x^{l,k}_{c,2} - x^{l,k}_{c,1})(z^q_c - x^{l,k}_{c,2} - x^{l,k}_{c,1})}{\sum_c (x^{l,k}_{c,2} - x^{l,k}_{c,1})^2}(x^{l,k}_{ic,2} - x^{l,k}_{ic,1})\right]^2} \quad \text{(C.3)}$$

$$\text{, for } ic = 1, ..., 4, c = 1, ..., 4$$

where $x_{i,j=1,2}$ is the composition of component i in each of the two j phases that are defined on the tie line.

Then, the composition of the new interpolated tie line $x^n_{i,j}$ is given by

$$x^n_{i,j}(\mathbf{z}^q) = \frac{\sum_k x^{l,k}_{i,j}(d^k(\mathbf{z}^q))^{-p}}{\sum_k (d^k(\mathbf{z}^q))^{-p}}, \text{ for } k = 1, ..., Nt \quad \text{(C.4)}$$

where Nt is the number of tie lines considered and p is an arbitrary exponent. In practice, Nt=20 and exponent p=3 shows good agreement with the full flash calculation.

The phase fraction α^q is determined by solving the following equation

$$z^q_i - \sum_{j=1,2} x^n_{i,j}\alpha^q_j = 0, \text{ for } i = 1, ..., 4 \quad \text{(C.5)}$$

In the three-phase regions, we determine the potential composition of the stable phases by determining the tie triangle that produces a plane that intersects the query composition. We formally define this as

$$Q(\mathbf{z}^q, \gamma) = \left[\mathbf{z}^q - \mathbf{x}^t_1(\gamma)\right]^T \cdot \left[\left[\mathbf{x}^t_2(\gamma) - \mathbf{x}^t_1(\gamma)\right]^T \times \left[\mathbf{x}^t_3(\gamma) - \mathbf{x}^t_1(\gamma)\right]^T\right]^T \quad \text{(C.6)}$$

where $x^t_{j=1,2,3}$ describes the composition of a tie triangle for each of the j phases and γ is an index vector defined on the interval $0 \leq \gamma \leq 1$ that describes a specific tie triangle in our set. We formally define γ as the distance along the vapor phase composition of the tie triangle family such that $\gamma = 0$ on the H_2O-CH_4-N_2 external face and $\gamma = 1$ on the H_2O-CO_2-N_2 external face. Furthermore, we use the $\times$ operator to denote the cross product and the $\cdot$ operator to denote the dot product.

We determine the phase compositions in the three-phase region by solving for the γ that minimizes Q at $\mathbf{z}^q$, which we call γ^0. The phase fraction α^q is determined by solving the following equation

$$z_i^q - \sum_{j=1,2,3} x_{i,j}^t(\gamma^0)\alpha_j^q = 0, \text{ for } i = 14 \tag{C.7}$$

We replicate a flash calculation by cycling through each phase region until we obtain a set of phase compositions $x_{i,j}^q$ and phase fractions α_j^q subject to the following constraints:

$$z_i^q - \sum_{j=1}^{Np} x_{i,j}^q \alpha_j^q = 0, \text{ for } i = 14, \tag{C.8}$$

and

$$\sum_{j=1}^{Np} \alpha_j^q = 1, \text{ s.t. } 0 \leq \alpha_j^q \leq 1, \tag{C.9}$$

and

$$\sum_{i=1}^{Nc}(1 - \sum_{j=1}^{Np} x_{i,j}^q) = 0, \text{ s.t. } 0 \leq x_{i,j}^q \leq 1. \tag{C.10}$$

Where Np is the number of total phases considered, which is three, Nc is the number of total components considered, which is four, $x_{i,j}^q$ is the either the output of $x_{i,j}^n(\mathbf{z}^q)$ padded to have zeros for the phase that is not stable or the output of $x_{i,j}^t(\mathbf{z}^q, \gamma^0)$.

Our two-phase region tie line interpolation scheme is quite similar that presented by Rannou et al. (2013), but our three-phase region tie triangle interpolation scheme is not. Instead of minimizing the angle between the query point and a specific tie triangle, Rannou et al. (2013) minimizes the distance between the query point and the query point project onto the tie line. In general, this algorithmic scheme is computationally fast and produces similar results to the output produced by CSMGem.

Appendix D

Basis for thermodynamic simulator

In this appendix, we provide detailed description of the flash calculation algorithm and the various equations of state used for each phase. The culmination of these calculations is available publicly at https://github.com/kdarnell/hydrateflash.

Table D.19 describes the nomenclature of the flash algorithm and each equation of state. In some cases, variables are used in multiple places, but take on different parameters. To avoid confusion, reference the nomenclature table.

D.1 Flash Algorithm

For the flash algorithm, we use the same approach given by Ballard and Sloan (2004a) where we minimize objective functions by Newton's Method to determine the molar phase fraction α_j of all j possible phases and the molar composition $x_{i,j}$ for all components i in phases j. The equations described below are nearly identical to those found in Ballard with a few exceptions. As input we provide the molar feed fractions z_i of each component. As stated in the main text, feed fractions sum to one, molar phase fractions sum to one, molar compositions in each phase sum to one, and these are all related by

$$\sum_{k=1}^{\Pi} \alpha_k x_{i,k} = z_i, \, i = 1, \ldots, C \tag{D.1}$$

for Π possible phases and C components.

We define one phase as the reference phase, which must be present and serves as the comparison phase for phase stability of the remaining possible phases. We can then re-arrange equation (D.1) as,

$$\alpha_r x_{i,r} + \sum_{\substack{k=1 \\ k \neq r}}^{\Pi} \alpha_k x_{i,k} = z_i, \, i = 1, \ldots, C \tag{D.2}$$

where r refers to the reference phase.

We then use the various equations of state (Section 2) to solve for the fugac-

ity $f_{i,k}$ of each component i in each phase k. A phase is stable by the following criteria,

$$\frac{f_{i,r}}{f_{i,k}} = \frac{x_{i,r}\phi_{i,r}P}{x_{i,k}\phi_{i,k}P} \begin{cases} 1, \text{ if phase } k \text{ is present} \\ < 1, \text{ if phase } k \text{ is not present} \end{cases}, i = 1, \ldots, C \tag{D.3}$$

where $\phi_{i,k}$ is the fugacity coefficient of component i in phase k and P is pressure.

This information is then combined into a distribution coefficient that compares the relative fugacity coefficients between component i and r in phase k as,.

$$K_{i,k} = \frac{\phi_{i,r}}{\phi_{i,k}} = \begin{cases} \frac{x_{i,k}}{x_{i,r}}, \text{ if phase } k \text{ is present} \\ \frac{x_{i,k}f_{i,r}}{x_{i,r}f_{i,k}}, \text{ if phase } k \text{ is not present} \end{cases}, i = 1, \ldots, C, k = 1, \ldots, \Pi \tag{D.4}$$

These two equations can be combined by introducing a stability variable that is zero when phase k is stable, described as,

$$y_k = \ln\left(\frac{f_{i,k}}{f_{i,r}}\right), k = 1, \ldots, \Pi \tag{D.5}$$

The distribution coefficient can then be re-written as,

$$K_{i,k} = \frac{\phi_{i,r}}{\phi_{i,k}} = \frac{x_{i,k}f_{i,r}}{x_{i,r}f_{i,k}} = \frac{x_{i,k}}{x_{i,r}}\exp(\ln(\frac{f_{i,r}}{f_{i,k}})) = \frac{x_{i,k}}{x_{i,r}}\exp(-y_k) \tag{D.6}$$

So, we can define the ratio of molar compositions for all phases and all components, regardless of whether they are present, as,

$$\frac{x_{i,k}}{x_{i,r}} = K_{i,k}e^{y_k} \tag{D.7}$$

And, Gupta et al. (1991) showed that this representation of the ratio of molar compositions is equivalent to minimizing the Gibbs free energy of the system subject to

$$S_k = \frac{\alpha_k y_k}{\alpha_k + y_k} = 0, k = 1, \ldots, \Pi \tag{D.8}$$

The minimum of the Gibbs free energy is found by minimizing S_k, such that $y_k = 0$ if $\alpha_k \neq 0$ (i.e., phase k is present) or $\alpha_k = 0$ if $y_k \neq 0$ (i.e., phase k is not present).

Then the relationship between molar composition, molar phase fraction, and feed compositions can be written as,

$$\left(\alpha_r + \sum_{\substack{k=1 \\ k\neq r}}^{\Pi} \alpha_k K_{i,k} e^{y_k}\right) x_{i,r} = z_i, \, i = 1, \ldots, C \tag{D.9}$$

which is valid for all phases and for all components. This relationship can then be combined with constraints on α and x to yield,

$$1 = \sum_{i=1}^{C} x_{i,k} = \sum_{i=1}^{C} \frac{z_i K_{i,k} e^{y_k}}{1 + \sum_{\substack{j=1 \\ j\neq r}}^{\Pi} \alpha_j (K_{i,j} e^{y_k} - 1)} \tag{D.10}$$

This gives a second set of objective functions that need to be minimized,

$$E_k = \sum_{i=1}^{C} \frac{z_i (K_{i,k} e^{y_k} - 1)}{1 + \sum_{\substack{j=1 \\ j\neq r}}^{\Pi} \alpha_j (K_{i,j} e^{y_j} - 1)} = 0, \, k = 1, \ldots, \Pi \tag{D.11}$$

The molar compositions are then defined as

$$x_{i,k} = \frac{z_i K_{i,k} e^{y_k}}{1 + \sum_{\substack{j=1 \\ j\neq r}}^{\Pi} \alpha_j (K_{i,j} e^{y_j} - 1)} = 0, \, i = 1, \ldots, C; \, k = 1, \ldots, \Pi \tag{D.12}$$

except the hydrate phase, which is defined as

$$x_{i,\mathrm{H}} = \frac{\sum_m \nu_m \theta_{i,m}}{1 + \sum_m \sum_j \nu_m \theta_{j,m}} \tag{D.13}$$

The algorithm is broken into an inner loop and outer loop. The inner loop solves for the minimum of S_k and E_k by updating y_k and α_k at fixed $x_{i,k}$ and $K_{i,k}$ until convergence. The outer loop uses the updated y_k and α_k to calculate $x_{i,k}$ and consequently $K_{i,k}$ through the equations of state. This update is performed only once (successive substitution), such that $|\Delta x_{i,k}| < 0.5 x_{i,k}$. The algorithm terminates when $\Delta x_{i,k} \approx 0$, $S_k < \epsilon$, and $E_k < \epsilon$, where ϵ is a sufficiently small number.

The inner loop is minimized by solving the following equation for $\Delta\beta_k$ where $\beta = y$ or $\beta = \alpha$,

$$\frac{\partial R}{\partial \beta}\Delta\beta = -R \tag{D.14}$$

with R_k either as S_k or E_k. These equations are all solved simultaneously yielding this system of equations

$$\begin{bmatrix} \frac{\partial E_1}{\alpha_1} & \cdots & \frac{\partial E_1}{\partial \alpha_\Pi} & \frac{\partial E_1}{\partial y_1} & \cdots & \frac{\partial E_1}{y_\Pi} \\ \vdots & \ddots & \vdots & \vdots & \ddots & \vdots \\ \frac{\partial E_\Pi}{\alpha_1} & \cdots & \frac{\partial E_\Pi}{\partial \alpha_\Pi} & \frac{\partial E_\Pi}{\partial y_1} & \cdots & \frac{\partial E_\Pi}{\partial y_\Pi} \\ \frac{\partial S_1}{\alpha_1} & \cdots & \frac{\partial S_1}{\partial \alpha_\Pi} & \frac{\partial S_1}{\partial y_1} & \cdots & \frac{\partial S_1}{y_\Pi} \\ \vdots & \ddots & \vdots & \vdots & \ddots & \vdots \\ \frac{\partial S_\Pi}{\alpha_1} & \cdots & \frac{\partial S_\Pi}{\partial \alpha_\Pi} & \frac{\partial S_\Pi}{\partial y_1} & \cdots & \frac{\partial S_\Pi}{\partial y_\Pi} \end{bmatrix} \begin{bmatrix} \Delta\alpha_1 \\ \vdots \\ \Delta\alpha_\Pi \\ \Delta y_1 \\ \vdots \\ \Delta y_\Pi \end{bmatrix} = - \begin{bmatrix} E_1 \\ \vdots \\ E_\Pi \\ S_1 \\ \vdots \\ S_\Pi \end{bmatrix} \tag{D.15}$$

We also ensure convergence of the inner loop using the suggestion of Gupta et al. (1991), who shows that if $y_k < \delta$ or $\alpha_k < \delta$, then we set $y_k = \delta, \alpha_k = \delta$ where $\delta = 1 \times 10^{-10}$. This ensures that either y_k or α_k goes to zero on the next iteration.

We define the Jacobian matrix terms similar to Ballard, except modify one term. The derivatives of E and S with respect to α are the same and defined as

$$\frac{\partial E_k}{\partial \alpha_j} = -\sum_{i=1}^{C} \frac{z_i(K_{i,k}e^{y_k} - 1)(K_{i,j}e^{y_j} - 1)}{\left(1 + \sum_{\substack{m=1 \\ m\neq r}}^{\Pi} \alpha_m(K_{i,m}e^{y_m} - 1)\right)^2}, k = 1, \ldots, \Pi(k \neq r), j = 1, \ldots, \Pi(j \neq r) \tag{D.16}$$

$$\frac{\partial S_k}{\partial \alpha_j} = \begin{cases} 0, & \text{if } k \neq j \\ \frac{y_k}{\alpha_k + y_k} - \frac{\alpha_k y_k}{(\alpha_k + y_k)^2}, & \text{if } k = j \end{cases} \tag{D.17}$$

And, the derivatives of S with respect to y are also the same and defined as,

$$\frac{\partial S_k}{\partial y_j} = \begin{cases} 0, & \text{if } k \neq j \\ \frac{\alpha_k}{\alpha_k + y_k} - \frac{\alpha_k y_k}{(\alpha_k + y_k)^2}, & \text{if } k = j \end{cases} \tag{D.18}$$

However, the derivatives of E with respect to y are different in the case that

$k = j$. The standard case is the same and defined as

$$\frac{\partial E_k}{\partial y_j} = -\sum_{i=1}^{C} \frac{z_i(K_{i,k}e^{y_k} - 1)(\alpha_j K_{i,j} e^{y_j})}{\left(1 + \sum_{\substack{m=1 \\ m \neq r}}^{\Pi} \alpha_m (K_{i,m} e^{y_m} - 1)\right)^2}, k = 1, \ldots, \Pi(k \neq r, j), j = 1, \ldots, \Pi(j \neq r, k) \tag{D.19}$$

In the case that $j = k$, the derivative is

$$\frac{\partial E_k}{\partial y_k} = \sum_{i=1}^{C} \frac{z_i(K_{i,k}e^{y_k} - 1)}{1 + \sum_{\substack{m=1 \\ m \neq r}}^{\Pi} \alpha_m (K_{i,m} e^{y_m} - 1)} - \frac{z_i(K_{i,k}e^{y_k} - 1)(\alpha_k K_{i,k} e^{y_k})}{(1 + \sum_{\substack{m=1 \\ m \neq r}}^{\Pi} \alpha_m (K_{i,m} e^{y_m} - 1))^2}, k = 1, \ldots, \Pi(k \neq r) \tag{D.20}$$

which has an extra term added to the standard derivative.

The algorithm is initialized by setting $\alpha_k = 1/\Pi$ and $y_k = 0$ and then approximating $K_{i,k}$ and $x_{i,k}$ using ideal (i.e., composition-independent) distribution coefficients defined in Section 2.

D.2 Equations of State

We have three equations of state for four possible phases (aqueous, hydrate, vapor hydrocarbon, and liquid hydrocarbon). We detail these equations of state using the published equations (Ballard and Sloan Jr, 2002, Jager et al., 2003, Sloan Jr and Koh, 2007) and the accompanying fitting parameters relevant to the components considered in this manuscript. We address each equation of state separately. However, for each equation of state the desired output is the fugacity of each component in each phase. Where applicable, the reference conditions are defined as $T_0 = 298.15$ K and $P_0 = 1$ bar.

We also describe the equations used to define the ideal distribution coefficients necessary to initialize the flash algorithm.

D.2.1 Hydrate equation of state

The hydrate equation of state found in Ballard is similar to other equations of state that use the chemical potential method of van der Waals-Platteeuw. How-

ever, the key difference is that the Ballard version allows for volume changes associated with different guests and the fugacity is, both, explicit in pressure, temperature, and composition and does not require an aqueous phase to be present.

Water is the only component where the fugacity in hydrate can be defined. Fugacity in hydrate for the other components is determined by whichever phase is stable. Thus, the equation of state presented below is only for water, but does consider the combined effects of the other components.

The fugacity of water in hydrate $f_{\mathrm{w}}^{\mathrm{H}}$ is defined as

$$f_{\mathrm{w}}^{\mathrm{H}} = f_{\mathrm{w},o} \exp\left[\frac{\mu_{\mathrm{w}}^{\mathrm{H}} - g_{\mathrm{w},o}}{RT}\right] \tag{D.21}$$

where the subscript refers to component and the superscript refers to the phase ($f_{\mathrm{w}}^{\mathrm{H}} = f_{\mathrm{w,H}}$ in the nomenclature of the flash algorithm), $\mu_{\mathrm{w}}^{\mathrm{H}}$ is the chemical potential of water in hydrate, $g_{\mathrm{w},o}$ is the Gibbs free energy of pure water in the ideal gas state, $f_{\mathrm{w},o}$ is the fugacity T is temperature, and R is the universal gas constant.

The chemical potential of water in the hydrate is defined as

$$\mu_{\mathrm{w}}^{\mathrm{H}} = g_{\mathrm{w}}^{\beta} + RT \sum_i \nu_i \ln\left(1 - \sum_J \theta_{J,i}\right) + RT \ln \gamma_{\mathrm{w}}^{\mathrm{H}} \tag{D.22}$$

where g_{w}^{β} is the Gibbs free energy of water in in standard hydrate state, $\theta_{J,i}$ is the fractional occupancy of component J in cage i (i.e., small or large cage for structure I hydrate), and $\gamma_{\mathrm{w}}^{\mathrm{H}}$ is the activity coefficient of water in hydrate, which accounts for the volume expansion of hydrate when filled with guest molecules.

The fractional occupancy of the cages follows the original van der Waals and Plateeuw theory, which takes the adsorption-like form of

$$\theta_{J,i} = \frac{C_{J,i} f_J}{1 + C_{J,i} f_J} \tag{D.23}$$

where J refers to each component, i refers to the hydrate cage, $C_{J,i}$ is the Langmuir constant defined as "attractiveness" of component J to the ith cage, and f_J is the fugacity of component J in some other phase that is stable.

The Langmuir constant is found by integrating a Kihara core potential with fitted parameters specific for each guest (i.e., kihara potential parameters) that a fit based on experimental data. The Kihara fitting parameters for the guests consid-

ered here are found in Table D.1. The equation for the Langmuir constant is

$$C_{J,i} = \frac{4\pi}{kT} \int_0^{R_1 - a_J} \exp\left[\frac{-\sum_n \omega_{J,n}(r)}{kT}\right] r^2 \, \mathrm{d}r \tag{D.24}$$

where k is the Boltzmann constant, a_J is the radius of the spherical core of component J (Table D.1), r is the distance of the guest molecule from the cavity center, R_1 is the free cavity radius of shells in cage i, and $\omega_{J,n}$ is the cell potential of shell n in cage i. The various shells considered here are found in Table D.7. The cell potential is defined as

$$\omega_{J,n}(r) = 2 z_n \epsilon_J \left[\frac{\sigma_J^{12}}{R_n^{11} r}\left(\delta^{10} + \frac{a_J}{R_n}\delta^{11}\right) - \frac{\sigma_J^{6}}{R_n^{5} r}\left(\delta^{4} + \frac{a_J}{R_n}\delta^{5}\right)\right] \tag{D.25}$$

where σ_J is the core distance at zero potential of component J (Table D.1), ϵ_J is the maximum attractive potential of component J (Table D.1), z_n is the number of water molecules in shell n of cage i (Table D.7), R_n is the free cavity radius of shell n in cage i (Table D.7), and δ is a function defined as

$$\delta^N = \frac{1}{N}\left[\left(1 - \frac{r}{R_n} - \frac{a_J}{R_n}\right)^{-N} - \left(1 + \frac{r}{R_n} - \frac{a_J}{R_n}\right)^{-N}\right] \tag{D.26}$$

The molar Gibbs free energy of water in the empty hydrate is defined as

$$\frac{g_{\mathrm{w}}^{\beta}}{RT} = \frac{g_{\mathrm{w}_0}^{\beta}}{RT_0} - \int_{T_0}^{T} \frac{h_{\mathrm{w}}^{\beta}}{RT^2} \, \mathrm{d}T + \int_{P_0}^{P} \frac{v_{\mathrm{w}}^{\beta}}{RT} \, \mathrm{d}P \tag{D.27}$$

where $g_{\mathrm{w}_0}^{\beta}$ is the molar Gibbs free energy of water for empty hydrate at reference conditions (Table D.2), g_{w}^{β} is the molar enthalpy of water in hydrate, and v_{w}^{β} is the molar volume of the hydrate.

The molar enthalpy of water in the hydrate is defined as

$$h_{\mathrm{w}}^{\beta} = h_{\mathrm{w}_0}^{\beta} + \int_{T_0}^{T} c_{P_{\mathrm{w}}^{\beta}} \, \mathrm{d}T \tag{D.28}$$

where $h_{\mathrm{w}_0}^{\beta}$ is the molar enthalpy of water in the empty hydrate at reference conditions (Table D.2) and $c_{P_{\mathrm{w}}^{\beta}}$ is the heat capacity of water in the empty hydrate.

The heat capacity of hydrate is defined as

$$c_{P_w} = a_0 + a_1 T + a_2 T^2 + a_3 T^3 \tag{D.29}$$

where the constants a_0, a_1, a_2, and a_3 are shown in Table D.5.

The molar volume of empty hydrate is expressed as

$$v_{\mathrm{w}}^{\beta} = (a_0^*)^3 \exp[\alpha_1(T - T_0) + \alpha_2(T - T_0)^2 + \alpha_3(P - T_0)^3 - \kappa_H(P - P_0)] \tag{D.30}$$

where a_0^* is the standard lattice parameter at reference conditions (11.99245 Å), κ_H is the volumetric compressibility of hydrate (Table D.3), and the constants α_1, α_2, and α_3 are volumetric thermal expansion parameters for hydrate (Table D.6).

The activity of water in hydrate is defined as the differences between a filled hydrate with guests and the standard empty hydrate. This is expressed as

$$\ln \gamma_{\mathrm{w}}^{\mathrm{H}} = \frac{\Delta g_{\mathrm{w}_0}^{\beta}}{RT_0} + \frac{\Delta h_{\mathrm{w}_0}^{\beta}}{R}\left(\frac{1}{T} - \frac{1}{T_0}\right) + \int_{P_0}^{P} \frac{\Delta v^{\mathrm{H}}}{RT}\,\mathrm{d}P \tag{D.31}$$

where $\Delta g_{\mathrm{w}_0}^{\beta}$ is the perturbation of the molar Gibbs free energy in water of hydrate due to filled cages, $\Delta h_{\mathrm{w}_0}^{\beta}$ is the perturbation of the molar enthalpy in water of hydrate due to filled cages, and Δv^{H} is the perturbation of the molar volume due to filled cages.

The perturbations of the molar Gibbs free energy and enthalpy are functions of the molar volume change at reference conditions. They are expressed as

$$\Delta g_{\mathrm{w}_0}^{\beta} = A^{\Delta} \Delta v_0^{\mathrm{H}} \tag{D.32}$$

$$\Delta h_{\mathrm{w}0}^{\beta} = B^{\Delta} \Delta v_0^{\mathrm{H}} \tag{D.33}$$

where A^{Δ} and B^{Δ} are fitted constants (Table D.2) and Δv_0^{H} is the difference between an empty and a filled hydrate at reference conditions.

More generally, the change in molar volume is expressed as

$$\Delta v^{\mathrm{H}} = v^{\mathrm{H}} - v^{\beta} \tag{D.34}$$

where v^{H} is molar volume of hydrate and is a function similar to that for the empty hydrate, but with additional terms for the filling of the hydrate. The molar volume of hydrate is expressed as

$$v^{\mathrm{H}} = v_0 \exp[\alpha_1(T - T_0) + \alpha_2(T - T_0)^2 + \alpha_3(T - T_0)^3 - \kappa_H(P - P_0)] \tag{D.35}$$

where v_0 is the guest-specific volume dependence at reference conditions. This guest-specific volume dependence is expressed as

$$v_0(\vec{x}) = \left(a_0^* + \sum_i N_i \sum_J f(\theta_{J,i}) \Delta r_{J,i}\right)^3 \tag{D.36}$$

where $v_0(\vec{x})$ denotes that the volume dependence is a function of composition, N_i is the number of cages of type i in the hydrate, $\Delta r_{J,i}$ are fitted repulsive constants for component J in cage i (Table D.4), and $f(\theta_{J,i})$ is a function of the fractional occupancy of component J in cage i.

The function $f(\theta_{J,i})$ is expressed as

$$\begin{aligned} f(\theta_{J,i}) &= \frac{(1 + \eta_{\mathrm{S}})\theta_{J,\mathrm{S}}}{1 + \eta_{\mathrm{S}}\theta_{J,\mathrm{S}}} \exp[D_J - (\bar{D})_{\mathrm{S}}], \text{ for } 5^{12} \text{ (S) cages} \\ &= \frac{(1 + \eta_{\mathrm{L}})\theta_{J,\mathrm{L}}}{1 + \eta_{\mathrm{L}}\theta_{J,\mathrm{L}}}, \text{ for } 5^{12}6^2 \text{ (L) cages} \end{aligned} \tag{D.37}$$

where η_i is the coordination number of cage i (z_i) per water molecule in the hydrate (Table D.7), D_J is the molecular diameter of component J (Table D.4), and $(\bar{D})_i$ is the fractional occupancy average of guest molecule diameters in cage i.

Formally, the fractional occupancy average of guest molecule diameters is expressed as

$$(\bar{D})_i = \sum_{J=1}^{C-1} D_J \theta_{J,i} \tag{D.38}$$

Table D.1: Regressed Kihara Potential Parameters

Component	a_J (Å)	σ_J (Å)	ϵ_J/k (K)
CH_4	0.3834	3.14393	155.593
CO_2	0.6805	2.97638	175.405
N_2	0.3526	3.13512	127.426

Table D.2: Regressed Formation Properties of Standard Hydrates

Property	sI
$g^{\beta}_{w_0}$ (J/mol)	-235537.85
$h^{\beta}_{w_0}$ (J/mol)	-291758.77
A^{Δ} (J/cm^3)	25.74
B^{Δ} (J/cm^3)	-481.32

The compressibility of hydrate when more than one guest is present is similarly expressed as

$$\kappa_{\mathrm{H}} = \sum_{J=1}^{C-1} \kappa_{J,\mathrm{H}} \theta_{J,\mathrm{L}} \tag{D.39}$$

D.2.2 Vapor and liquid hydrocarbon equation of state

We use the Soave-Redlich-Kwong (SRK) equation of state for the vapor and liquid hydrocarbons phases to mimic that used in Ballard. This is a well-known equation of state. However, we reproduce the necessary equations here for completeness.

Table D.3: Regressed Volumetric Compressibility Parameters for Hydrate Volume

Component	$\kappa_{J,\mathrm{H}}$ (bar^{-1})
CH_4	3.0E-05
CO_2	3.0E-6
N_2	3.1E-5

Table D.4: Regressed Repulsive Constants and Guest Diameters for Hydrate Volume

Component	Diameter (Å) D_J	Repulsive Constant sI small cage $\Delta r_{J,\mathrm{S}}$	Repulsive Constant sI large cage $\Delta r_{J,\mathrm{L}}$
CH_4	4.427	1.7668E-2	1.0316E-2
CO_2	4.603	0	5.8282E-3
N_2	4.177	1.7377E-2	0

Table D.5: Heat capacity parameters for sI Hydrate at 1 bar

a_0/R	a_1/R (K^{-1})(10^2)	a_2 (K^{-2})(10^5)	a_3 (K^{-3})(10^9)
0.735409713	1.14180551	-1.72746	63.5104

Table D.6: Regressed Volumetric Thermal Expansion Parameters for sI Hydrate

α_1 (K^{-1})	α_2 (K^{-2})	α_3 (K^{-3})
3.384960E-4	5.400990E-7	-4.769460E-11

Table D.7: Hydrate Cage Characteristics of sI Hydrates

Nominal size (a_0)	12.03 Å
Small cage (5^{12})	
No. of water molecules in cage	20
Average radius	3.908 Å
Layer 1	
Layer type	(i)
No. of water molecules in layer	8
Radius of layer	3.83 Å
Layer 2	
Layer type	(k)
No. of water molecules in layer	12
Radius of layer	3.96 Å
Large cage ($5^{12}6^2$)	
No. of water molecules in cage	24
Average radius	4.326 Å
Layer 1	
Layer type	(i)
No. of water molecules in layer	8
Radius of layer	4.47 Å
Layer 2	
Layer type	(k)
No. of water molecules in layer	8
Radius of layer	4.06 Å
Layer 3	
Layer type	(k)
No. of water molecules in layer	4
Radius of layer	4.645 Å
Layer 4	
Layer type	(c)
No. of water molecules in layer	4
Radius of layer	4.25 Å

This equation of state equation relates pressure, temperature, molar volume as

$$P = \frac{RT}{v-b} - \frac{a}{v(v+b)} \tag{D.40}$$

where v is molar volume, a is an energy constant, and b is a volume constant. The energy constant parameter is defined as

$$a = \sum_{i=1}^{C}\sum_{j=1}^{C} x_i x_j a_{ij} \tag{D.41}$$

where x_i is the mole fraction of component i in either the vapor phase ($x_{i,\mathrm{V}}$) or the liquid hydrocarbon phase ($x_{i,\mathrm{L}}$), a_{ij} represents attractive forces between components i and j, and is expressed as,

$$a_{ij} = (1-k_{ij})\sqrt{\alpha_i a_i \alpha_j a_j} \tag{D.42}$$

where k_{ij} is the interaction parameter between components i and j (Table D.9), and a_i represents attractive forces between two molecules of component i, and is expressed as

$$a_i = 0.42747\frac{R^2 T_{c_i}^2}{P_{c_i}} \tag{D.43}$$

The α_i term is a corrective term for the vapor pressure of pure component i, and is expressed as

$$\alpha_i = \left(1 + S_{1_i}(1-\sqrt{T_{r_i}}) + S_{2_i}\frac{(1-\sqrt{T_{r_i}})}{\sqrt{T_{r_i}}}\right)^2 \tag{D.44}$$

where S_{2_i} is a constant, T_{r_i} is the reduced temperature calculated as

$$T_{r_i} = \frac{T}{T_{c_i}} \tag{D.45}$$

and S_{1_i} is expressed in terms of the acentric factor as

$$S_{1_i} = 0.48508 + 1.55171\omega_i - 0.15613\omega_i^2 \tag{D.46}$$

Table D.8: Critical properties and molecular weight

Component	T_c (K)	P_c (bar)	V_c (L/mol)	M_w	ω	S_2
CH_4	190.56	45.991	0.09865	16.043	0.0115	-0.012223
CO_2	304.21	73.831	0.09396	44.010	0.2236	-0.004474
N_2	126.20	34.001	0.08919	28.013	0.0377	-0.011016
H_2O	647.30	220.483	0.05595	18.015	0.3440	-0.201789

For water, $S_{1_w} = 1.2440$.

The volume constant b represents the average hard core volume of the mixture and is expressed using standard linear mixing rules as

$$b = \sum_{i=1}^{C} x_i b_i \tag{D.47}$$

where b_i is the hard core volume of component i, expressed as

$$b_i = 0.08664 \frac{T T_{c_i}}{P_{c_i}} \tag{D.48}$$

Development of the fugacity of any component in the vapor and liquid hydrocarbon phases using a cubic equation of state is explicit in fugacity, which can be found via the following thermodynamic relationship

$$\begin{aligned} f_i &= x_i P \exp\left[\int_0^P \left(\frac{\bar{v_i}}{RT} - \frac{1}{P}\right) \mathrm{d}P\right] \\ &= x_i P \exp\left[\frac{b_i}{b}(z-1) - \ln(z-B) - \frac{A}{B}\left(\frac{2\sum_{j=1}^{C} x_j a_{ij}}{a} - \frac{b_i}{b}\right) \ln(1+\frac{B}{z})\right] \end{aligned} \tag{D.49}$$

where $A = \frac{aP}{R^2T^2}$, $B = \frac{bP}{RT}$, and $z = \frac{Pv}{RT}$.

Table D.9: Interaction parameters (k_{ij}) for SRK EOS

Components	CH_4	CO_2	N_2	H_2O
CH_4	-	0.0936	0.0291	0.4965
CO_2	0.0936	-	-0.0462	-0.07
N_2	0.0291	-0.0462	-	0.5063
H_2O	0.4965	-0.07	0.5063	-

D.2.3 Aqueous equation of state

The fugacity for the aqueous phase is expressed using an explicit relationship similar to the hydrate phase. This relationship is defined as

$$f_{i,k} = f_{i,o} \exp\left[\frac{\mu_{i,k} - g_{i,o}}{RT}\right] \tag{D.50}$$

where the subscript o refers to the property of component i in the ideal gas stat, $f_{i,o}$ is the ideal gas fugacity of component i at 1 bar simply equal to 1 bar, $g_{i,o}$ is the gibbs energy of component i in the ideal gas state.

The Gibbs free energy of component i in the ideal gas state is expressed as

$$\frac{g_{i,o}}{RT} = \frac{g_{i_0,o}}{RT_0} - \int_{T_0}^{T} \frac{h_{i,o}}{RT^2} \mathrm{d}T \tag{D.51}$$

where $g_{i_0,o}$ is the molar Gibbs energy of formation at T_0 and P_0 (Table D.10) and $h_{i,o}$ is the enthalpy at P_0 and T_0.

The enthalpy of component i in the ideal gas state is expressed as

$$h_{i,o} = h_{i_0,o} + \int_{T_0}^{T} c_{P_i} \mathrm{d}T \tag{D.52}$$

where $h_{i_0,o}$ is the molar enthalpy of formation at T_0 and P_0 (Table D.10), c_{P_i} is the heat capacity.

The heat capacity of component i in water is expressed

$$c_{P_i} = a_0 + a_1 T + a_2 T^2 + a_3 T^3 \tag{D.53}$$

where the constants a_0, a_1, a_2, and a_3 are defined in Table D.11.

The chemical potential of component i (excluding water) in the aqueous phase is expressed as

$$\frac{\mu_{i,\text{Aq}}}{RT} = \frac{\bar{g}_{i_0^*}}{RT_0} - \int_{T_0}^{T} \frac{\bar{h}_{i^*}}{RT^2}\mathrm{d}T + \int_{P_0}^{P} \frac{\bar{v}_{i^*}}{RT}\mathrm{d}P + \ln a_{i,\text{Aq}},\ i \neq \text{water} \tag{D.54}$$

where the subscripts $*$ and 0 refer to the component i in a hypothetical 1 molal solution and standard conditions (T_0 and P_0), respectively. $\bar{g}_{i_0^*}$ (Table D.12), $\bar{h}_{i^*}$, and $\bar{v}_{i^*}$ (Table D.12) are the partial molar Gibbs energy of formation, enthalpy, and volume of component i in the 1 molal solution.

The partial molar enthalpy is expressed as

$$\bar{h}_{i^*} = \bar{h}_{i_0^*} + \int_{T_0}^{T} \bar{c}_{P_i^*}\mathrm{d}T \tag{D.55}$$

where $\bar{h}_{i_0^*}$ is the partial molar enthalpy (at T_0 and P_0) (Table D.12) and $c_{P_i^*}$ is the partial molar heat capacity (at P_0) of solutes in the aqueous phase.

The partial molar heat capacity and partial molar volume is expressed as

$$c_{P_i^*} = c_1 + \frac{c_2}{T^2} + \omega_{Born} T X \tag{D.56}$$

where the constants c_1 and c_2 are defined in Table D.13, and ω_{Born} is defined in Table D.12.

The partial molar volume of component i is defined as

$$\bar{v}_{i^*} = v_1 + \frac{v_2}{\Psi + P} + \left[v_3 + \frac{v_4}{\Psi + P}\right]\frac{1}{T - \Theta - \tau} - \frac{\omega_{\text{Born}}}{\epsilon^2}\left(\frac{\partial \epsilon}{\partial P}\right)_T \tag{D.57}$$

where $\Theta = 228$K, $\Psi = 2600$ bar, ω_{Born} is the Born coefficient (Table D.12), and the constants v_1, v_2, v_3, and v_4 are defined in Table D.13.

The term X is calculated from

$$X = \frac{1}{\epsilon}\left[\left(\frac{\partial^2 \ln \epsilon}{\partial T^2}\right)_P - \left(\frac{\partial \ln \epsilon}{\partial T}\right)_P^2\right] \tag{D.58}$$

The dielectric constant of water ϵ is expressed as

$$\epsilon = \sum_{n=0}^{2}(a_{1n} + a_{2n}P + a_{3n}P^2)T^n \tag{D.59}$$

where the a_{mn} constants are defined in Table D.14.
The term τ in the partial molar volume is calculated from

$$\tau = \frac{(5/6)T - \Theta}{1 + e^{(T-273.15)/5}} \tag{D.60}$$

The chemical potential of water in the aqueous phase is defined as

$$\frac{\mu_{\text{w,Aq}}}{RT} = \frac{g_{w_0,\text{Aq}_{\text{pure}}}}{RT_0} - \int_{T_0}^{T}\frac{h_{\text{w,Aq}_{\text{pure}}}}{RT^2}\mathrm{d}T + \int_{P_0}^{P}\frac{v_{\text{w,Aq}_{\text{pure}}}}{RT}\mathrm{d}P + \ln a_{\text{w,Aq}} \tag{D.61}$$

where the Aq_{pure} subscript refers to pure liquid water phase.
The volume of pure liquid water is expressed as

$$v_{\text{w,Aq}_{\text{pure}}} = \sum_{n=0}^{3}(a_{1n} + a_{2n}P + a_{3n}P^2 + a_{4n}P^3)T^n \tag{D.62}$$

where the constants a_{mn} are defined in Table D.16.
The activity of the solutes is expressed as,

$$a_{j,\text{Aq}} = \frac{m_j}{m_{j^*}}\gamma_{j,\text{Aq}} \tag{D.63}$$

where m_j is the molality of species j, m_{j^*} is the molality at the standard state (1 molal), and $\gamma_{j,\text{Aq}}$ is the activity coefficient of species j in the aqueous phase

Since we do not consider any ionic species in this paper, the activity coefficient is expressed using the Pitzer-type relationship,

$$\ln \gamma_{j,\text{Aq}} = 2\sum_{k} m_k \gamma_{P1_{jk}} \tag{D.64}$$

$$\gamma_{P1_{jk}} = \beta_{0_{jk}} \tag{D.65}$$

Table D.10: Ideal gas formation properties

Component	$g_{i_{0,o}}$(J/mol)	$h_{i_{0,o}}$(J/mol)
CH_4	-50830	-74900
CO_2	-394600	-393800
N_2	0	0
H_2O	-228700	-242000

Table D.11: Ideal gas heat capacity parameters

Component	a_0/R	a_1/R(K^{-1})(10^2)	a_2/R(K^{-2})(10^5)	a_3/R(K^{-3})(10^9)
CH_4	2.3902	0.6039	0.1525	-1.3234
CO_2	2.6751	0.7188	-0.4208	0.8977
N_2	3.4736	-0.0189	0.0971	-0.3453
H_2O	3.8747	0.0231	0.1269	-0.4321

$$\ln a_{\text{w,Aq}} = -M_w \left[\sum_j \sum_k m_j m_k \gamma_{P1_{jk}} + \sum_j m_j \right] \tag{D.66}$$

where M_w is the molecular weight of water.

For a CO_2-CO_2 molecular interaction,

$$\beta_{0_{jj}} = 0.107 - 4.5\text{E-}4T, \text{ for } j = \text{CO}_2 \tag{D.67}$$

For all other interactions, $\gamma_{P1_{jk}} = 0$.

Table D.12: Partial molar formation properties and Born constants of solutes

Component	$\bar{g}^*_{i_0}$(J/mol)	$\bar{h}^*_{i_0}$(J/mol)	ω_{Born}(J/mol)
CH_4	-34451	-87906	-133009
CO_2	-385974	-413798	-8368
N_2	18188	-10439	-145101

Table D.13: Partial molar heat capacity (at 1 bar) and volume terms of solutes

Parameter	CH_4	CO_2	N_2
c_1(J/mol-K)	176.12	167.50	149.75
c_2(J-K/mol)	6310762	5304066	5046230
v_1(J/mol-bar)	2.829	2.614	2.596
v_2 (J/mol)	3651.8	3125.9	3083.0
v_3(J-K/mol-bar)	9.7119	11.7721	11.9407
v_4(J-K/mol)	-131365	-129198	-129018

Table D.14: Parameters for dielectric constant of water

	$n = 0$	$n = 1$ (K^{-1})	$n = 2$ (K^{-2})
a_{1n}	243.9576	-0.7520846	6.60648E-4
a_{2n} (bar^{-1})	0.039037	-2.12309E-4	3.18021E-7
a_{3n} (bar^{-2})	-1.01261E-5	6.04961E-8	-9.33341E-11

Table D.15: Formation properties and heat capacity terms of pure water

$g_{w_0,\mathrm{Aq}_{\mathrm{pure}}}$(J/mol)	-237129
$h_{w_0,\mathrm{Aq}_{\mathrm{pure}}}$(J/mol)	-285830
a_0/R	8.712
a_1/R(K^{-1})(10^2)	0.125
a_2/R(K^{-2})(10^5)	-0.018
a_3/R(K^{-3})(10^9)	0

Table D.16: Parameters for volume of water (cm^3/mol)

	$n = 0$	$n = 1$ (K^{-1})	$n = 2$ (K^{-2})	$n = 3$ (K^{-3})
a_{1n}	31.1251	-1.14154E-1	3.10034E-4	-2.48318E-7
a_{2n} (bar^{-1})	-2.46176E-2	2.15663E-4	-6.48160E-7	6.47521E-10
a_{3n} (bar^{-2})	8.69425E-6	-7.96939E-8	2.45391E-10	-2.51773E-13
a_{4n} (bar^{-3})	-6.03348E-10	5.57791E-12	-1.72577E-14	1.77978E-17

D.3 Ideal distribution coefficients (K-values)

Ideal distribution coefficients are composition-independent distribution coefficients that depend on a single component at a time. These distribution coefficients are used to initialize $K_{i,k}$ and $x_{i,k}$ in the flash algorithm. There is a separate subsection for each several phase combinations.

D.3.1 Vapor and Liquid hydrocarbon phases

The distribution coefficients between vapor phase and liquid phase hydrocarbons is expressed by the Wilson correlation for ideal K-values as

$$K_i = \frac{x_{i,\mathrm{V}}}{x_{i,\mathrm{L}}} = \frac{P_{c_i}}{P} \exp\left(5.373(1+\omega_i)(1-\frac{T_{c_i}}{T})\right), i \neq \text{water}. \tag{D.68}$$

The distribution coefficients is slightly different for water and expressed as

$$K_i = \frac{x_{i,\mathrm{V}}}{x_{i,\mathrm{L}}} = \frac{-133.67 + 0.63288T}{P} + 3.19211\text{E-}3P, i = \text{water}. \tag{D.69}$$

D.3.2 Vapor and aqueous phases

The distribution coefficients between vapor phase and aqueous phase is defined by a modification to Raoult's law. Raoult's law is

$$x_{i,\mathrm{V}}\phi_{i,\mathrm{V}}P = x_{i,\mathrm{Aq}}\gamma_{i,\mathrm{Aq}}P_i^{sat} \exp\left[\int_{P_i^{sat}}^{P} \frac{v}{RT}, \mathrm{d}P\right] \tag{D.70}$$

where $\gamma_{i,\mathrm{Aq}}$ is the activity coefficient of component i in the Aqueous phase and P_i^{sat} is the temperature-dependent saturation pressure of component i.

We make the same assumptions as Ballard, which are 1) $\gamma_{i,\mathrm{Aq}} \approx \gamma_{i,\mathrm{Aq}}^{\infty}$, 2) $\phi_{i,\mathrm{V}} \approx 1$, and 3) exponential term (poynting correction) is unity. Then we define the distribution coefficient as

$$K_i = \frac{x_{i,\mathrm{V}}}{x_{i,\mathrm{Aq}}} = \frac{P_i^{sat}}{P}\gamma_{i,\mathrm{Aq}}^{\infty}. \tag{D.71}$$

where $\gamma_{i,\mathrm{Aq}}^{\infty}$ is the infinite dilution activity coefficient.

These remaining parameters are expressed with correlations. For hydrocarbons, the saturation pressure is expressed as

$$P_i^{sat} = P_{c_i} \exp[a_1 + \omega_i a_2] \tag{D.72}$$

where a_1 and a_2 are constants.
These constants are defined as

$$a_1 = 5.927140 - 6.096480\frac{T_{c_i}}{T} - 1.288620 \ln \frac{T}{T_{c_i}} + 0.169347\frac{T^6}{T_{c_i}^6} \tag{D.73}$$

and

$$a_2 = 15.25180 - 15.68750\frac{T_{c_i}}{T} - 13.47210 \ln \frac{T}{T_{c_i}} + 0.43577\frac{T^6}{T_{c_i}^6} \tag{D.74}$$

For water, the saturation pressure is expressed as

$$P_i^{sat} = \exp\left[12.048399 - \frac{4030.18245}{T - 38.15}\right] \tag{D.75}$$

The infinity dilution coefficient for hydrocarbons is defined as

$$\gamma_i^{\infty} = \exp\left[0.688 + 0.642 N_1\right] \tag{D.76}$$

where N_1 is the total number of carbon atoms in molecule i (the solute in the water). For water, $\gamma_i^{\infty} = 1$.

D.3.3 Vapor and hydrate phases

The ideal distribution coefficient between hydrate phase and vapor phase is based on water-free correlations that are converted to a regular distribution coefficient. The water-free distribution coefficient is expressed as

$$K_i^{wf} = \frac{x_{i,\mathrm{V}}^{wf}}{x_{i,\mathrm{H}}^{wf}} \tag{D.77}$$

where the wf subscript refers to the water-free basis.

Water-free compositions as are represented as

$$x_{i,\mathrm{H}}^{wf} = \frac{x_{i,\mathrm{H}}}{\sum_{\substack{j=1 \\ j\neq \mathrm{w}}}^{C} x_{j,\mathrm{H}}} = \frac{x_{i,\mathrm{H}}}{1 - x_{\mathrm{w,H}}} \tag{D.78}$$

This is then re-arranged to provide a relationship between the real composition and the water-free compositions as

$$x_{i,\mathrm{H}} = x_{i,\mathrm{H}}^{wf}(1 - x_{\mathrm{w,H}}), \tag{D.79}$$

The ideal K-value is then

$$\begin{aligned} K_i = \frac{x_{i,\mathrm{V}}}{x_{i,\mathrm{H}}} &= \frac{x_{i,\mathrm{V}}}{x_{i,\mathrm{H}}^{wf}(1 - x_{\mathrm{w,H}})} \approx \frac{x_{i,\mathrm{V}}^{wf}}{x_{i,\mathrm{H}}^{wf}(1 - x_{\mathrm{w,H}})} \\ &= \frac{K_i^{wf}}{1 - x_{\mathrm{w,H}}} \end{aligned} \tag{D.80}$$

where $x_{\mathrm{w,H}} = 0.88$ for structure 1 (prior to flash calculation).

However, the K-value for water in hydrate is, alternatively, expressed as

$$K_{\mathrm{w}} = \frac{x_{\mathrm{w,V}}}{x_{\mathrm{w,H}}} = \frac{K_{\mathrm{w,V\text{-}Aq}}}{x_{\mathrm{w,H}} K_{\mathrm{w,Ice\text{-}Aq}}} \tag{D.81}$$

where the $K_{\mathrm{w,V\text{-}Aq}}$ distribution is given in the vapor and aqueous phase ideal K-value section and the $K_{\mathrm{w,Ice\text{-}Aq}}$ is defined in the next section.

For guest, the water-free distribution coefficients are expressed as

$$\begin{aligned} K_i^{wf} &= \frac{x_{i,\mathrm{V}}^{wf}}{x_{i,\mathrm{H}}^{wf}} \\ &= \exp\Bigg[a_1 + a_2 \ln P + a_3 (\ln P)^2 - (1/T)(a_4 + a_5 \ln P + a_6 (\ln P)^2 + \\ &\quad a_7 (\ln P)^3) + a_8/P + a_9/P^2 + a_{10} T + a_{11} P + a_{12} \ln \frac{P}{T^2} + a_{13}/T^2\Bigg] \end{aligned} \tag{D.82}$$

where the constants are shown in Table D.17

Table D.17: Parameters for Eq.

	CH_4	CO_2	N_2
a_1	27.474169	15.8336435	173.2164
a_2	-0.8587468	3.119	-0.5996
a_3	0	0	0
a_4	6604.6088	3760.6324	24751.6667
a_5	50.8806	1090.27777	0
a_6	1.57577	0	0
a_7	-1.4011858	0	0
a_8	0	0	1.441
a_9	0	0	-37.0696
a_{10}	0	0	-0.287334
a_{11}	0	0	-2.07405E-5
a_{12}	0	0	0
a_{13}	0	0	0

D.3.4 Ice and aqueous phases

We do not explicitly consider ice as a possible phase. However, we need the ideal K-value for water in ice to produce the ideal K-value for water in hydrate.

The ideal K-value between ice phase and aqueous phase is

$$K_i = \frac{x_{i,\text{Ice}}}{x_{i,\text{Aq}}} \begin{cases} 0, \text{ if } i \neq \text{water}, \\ \frac{1}{x_{i,\text{Aq}}}, \text{ if } i = \text{water} \end{cases} \tag{D.83}$$

The aqueous phase water composition is expressed as

$$x_{\text{w,Aq}} = 1 + 8.33076\text{E-}3(T - T_{\text{ice}}) + 3.91416\text{E-}5(T - T_{\text{ice}})^2 \tag{D.84}$$

where T_{ice} is expressed as

$$T_{\text{ice}} = 273.1576 - 7.404\text{E-}3(P - P_0) - 1.461\text{E-}6(P - 6.11657\text{E-}3)^2 \tag{D.85}$$

Table D.18: K-values for each phase with respect to each possible reference phase

	Reference phase		
	V	L	Aq
$K_{i,\mathrm{V}}$	1	$K_{i;1}$	$K_{i;2}$
$K_{i,\mathrm{L}}$	$\frac{1}{K_{i;1}}$	1	$\frac{K_{i;2}}{K_{i;1}}$
$K_{i,\mathrm{Aq}}$	$\frac{1}{K_{i;2}}$	$\frac{K_{i;1}}{K_{i;2}}$	1
$K_{i,\mathrm{H}}$	$\frac{1}{K_{i;3}}$	$\frac{K_{i;1}}{K_{i;3}}$	$\frac{K_{i;2}}{K_{i;3}}$

D.3.5 Combining ideal K-values

The ideal distribution coefficients must be combined into distribution coefficients that all have the reference phase in the denominator. Thus, the ideal K-values described above need to be converted into K-values that correspond to meaningful values in the flash algorithm.

We treat the ideal K-values according to a naming system that where a semicolon and a number in the subscript reference one of the ideal K-values. These are expressed as

$$K_{i;1} = \frac{x_{i,\mathrm{V}}}{x_{i,\mathrm{L}}}, K_{i;2} = \frac{x_{i,\mathrm{V}}}{x_{i,\mathrm{Aq}}}, K_{i;3} = \frac{x_{i,\mathrm{V}}}{x_{i,\mathrm{H}}} \tag{D.86}$$

We seek a set of distribution coefficients for the flash algorithm that is defined as

$$K_{i,m} = \frac{x_{i,m}}{x_{i,r}}, \text{ for } m = \text{V,L,Aq,H, for } r = \text{V,L,Aq} \tag{D.87}$$

These reference phase distribution coefficients are determined according the conversion relationship defined in Table D.18.

Table D.19: Nomenclature

Symbol	Parameter	Unit
	Hydrate Equation of State	
a_J	Hard core radius of component J for Kihara Potential	Å
σ_J	Soft core radius of component J for Kihara Potential	Å

Table D.19: Nomenclature

Symbol	Parameter	Unit
ϵ_J	Potential well depth of component J for Kihara Potential	J
$g^{\beta}_{\mathrm{w}_0}$	Gibbs free energy of water at reference conditions in empty hydrate phase	J/mol
$h^{\beta}_{\mathrm{w}_0}$	Enthalpy of water at reference conditions in empty hydrate phase	J/mol
A^{Δ}	Constant for perturbed Gibbs free energy of filled hydrate	J/cm^3
B^{Δ}	Constant for perturbed enthalpy of filled hydrate	J/cm^3
$\kappa_{J,\mathrm{H}}$	Compressibility of hydrate when filled with component j	bar^{-1}
D_J	Diameter of guest molecule J	Å
$\Delta r_{J,\mathrm{m}}$	Repulsive constant for hydrate volume of guest J in cage m	-
a_0	Nominal size of hydrate unit cell	Å
α_n	Thermal expansion parameter for hydrate of exponent n	K^{-n}
$\theta_{J,i}$	Fractional occupation of cage i by component J	-
$C_{J,i}$	Langmuir constant for cage i and component J	-
k	Boltzmann constant	J/K
$\omega_{J,n(m)}$	Cell potential of component J in shell n of cage m	J
$z_n(m)$	Number of water molecules in shell n of cage m	-
$\gamma^{\mathrm{H}}_{\mathrm{W}}$	Activity coefficient for water in hydrate	-
g^{H}_J	Gibbs energy of component J in hydrate	J/mol
μ^{H}_J	Chemical potential of component J in hydrate	J/mol
R	Universal Gas constant	J/mol-K
T	Temperature	K
T_0	Reference temperature (298 K)	K
P	Pressure	bar
P_0	Reference pressure (1 bar)	bar
ν_i	Number of cages of type i per water molecule in hydrate	-
$f^{\mathrm{H}}_{\mathrm{w}}$	Fugacity of water in hydrate	bar
v^{β}_{w}	Molar volume of empty hydrate	cm^3/mol
$v^{\mathrm{H}}_{\mathrm{w}}$	Molar volume of filled hydrate	cm^3/mol
$c^{\beta}_{P_{\mathrm{w}}}$	Heat capacity of water in empty hydrate	J/mol-K
$v_0(x)$	Compositional dependence of hydrate at reference conditions	cm^3/mol

Table D.19: Nomenclature

Symbol	Parameter	Unit
P_{c_i}	Critical pressure of component i	bar
T_{c_i}	Critical temperature of component i	K
ω_i	Acentric factor of component i	-
$\gamma^{\infty}_{i,\text{Aq}}$	Infinite dilution activity coefficient of component i in the aqueous phase	-
P_i^{sat}	Saturation pressure of component i	bar
K_i^{wf}	Water-free ideal distribution coefficient for component i	-
K_i	Ideal distribution coefficient between two phases for component i	-
$K_{i,M\text{-}N}$	Ideal distribution coefficient between phases M and N for component i	-
	Hydrate Equation of State	
$f_{i,o}$	Fugacity of component i in the ideal gas state	bar
$g_{i,o}$	Gibbs free energy of component i in the ideal gas state	J/mol
$h_{i,o}$	Enthalpy of component i in the ideal gas state	J/mol
$g_{i_0,o}$	Gibbs free energy of formation at reference conditions for component i	J/mol
$h_{i_0,o}$	Enthalpy of formation at reference conditions for component i	J/mol
$\bar{g}_i^*$	Partial molar Gibbs free energy in a hypothetical 1 molal solution i	J/mol
$\bar{h}_i^*$	Partial molar enthalpy in a hypothetical 1 molal solution for component i	J/mol
$\bar{v}_i^*$	Partial molar volume in a hypothetical 1 molal solution for component i	J/mol
$\bar{g}_{i0}^*$	Partial molar heat capacity at P_0 for component i	J/mol
ϵ	Dielectric constant of water	-
ω_{Born}	Born coefficient	-
m_j	Molality of species j	molal
$a_{j,Aq}$	Activity coefficient for component j in the aqueous phase	-

Table D.19: Nomenclature

Symbol	Parameter	Unit
	Vapor and Liquid Hydrocarbon Equation of State	
v_i	Molar volume of component i in either the liquid hydrocarbon or vapor phase	cm^3/mol
a_{ij}	Attractive forces between components i and j	-
k_{ij}	Interaction parameter between components i and j	-
a_i	Attractive forces between two molecules of component i	-
α_i	Corrective term for the vapor pressure of pure component i	-
T_{r_i}	Reduced temperature of component i	K
S_{1_i}	Constant for acentric factor for component i	-
	Flash Calculation	
α_k	Molar phase fraction of phase k	-
$x_{i,k}$	Mole fraction of component i in phase k	-
$K_{i,k}$	Distribution coefficient of component i in phase k	-
$\phi_{i,k}$	Fugacity coefficient of component i in phase k	-
y_k	Stability coefficient of component k	-
S_k	Gibbs free energy minimization constraint for phase k	-
E_k	Objective function to minimize Gibbs free energy for phase k	-

Bibliography

Brian Anderson, Ray Boswell, Timothy S Collett, Helen Farrell, Satoshi Ohtsuki, Mark White, and Margarita Zyrianova. Review of the findings of the iġnik sikumi co2-ch4 gas hydrate exchange field trial. In *Proceedings of the 8th International Conference on Gas Hydrates (ICGH8-2014), July*, 2014.

David Archer, Bruce Buffett, and Victor Brovkin. Ocean methane hydrates as a slow tipping point in the global carbon cycle. *Proceeding of the National Academy of Sciences*, 106, 2009.

AL Ballard and ED Sloan. The next generation of hydrate prediction: Part iii. gibbs energy minimization formalism. *Fluid phase equilibria*, 218(1):15–31, 2004a. ISSN 0378-3812.

AL Ballard and ED Sloan Jr. The next generation of hydrate prediction: I. hydrate standard states and incorporation of spectroscopy. *Fluid Phase Equilibria*, 194: 371–383, 2002. ISSN 0378-3812.

L Ballard and ED Sloan. The next generation of hydrate prediction iv: A comparison of available hydrate prediction programs. *Fluid phase equilibria*, 216(2): 257–270, 2004b. ISSN 0378-3812.

Jacob Bear. Dynamics of fluids in porous media. *Eisevier, New York, 764p*, 1972.

C. Berndt, T. Feseker, T. Treude, S. Krastel, V. Liebetrau, H. Niemann, V. J. Bertics, I. Dumke, K. Dünnbier, B. Ferré, C. Graves, F. Gross, K. Hissmann, V. Hühnerbach, S. Krause, K. Lieser, J. Schauer, and L. Steinle. Temporal constraints on hydrate-controlled methane seepage off svalbard. *Science*, 343(6168):284–287, 2014. doi: 10.1126/science.1246298. URL `http://www.sciencemag.org/content/343/6168/284.abstract`.

A. Biastoch, T. Treude, L. H. Rüpke, U. Riebesell, C. Roth, E. B. Burwicz, W. Park, M. Latif, C. W. Böning, G. Madec, and K. Wallmann. Rising arctic ocean temperatures cause gas hydrate destabilization and ocean acidification. *Geophysical Research Letters*, 38(8):n/a–n/a, 2011. ISSN 1944-8007. doi: 10.1029/2011GL047222. URL `http://dx.doi.org/10.1029/2011GL047222`. L08602.

A. Knut Birkedal, P. Lars Hauge, Arne Graue, and Geir Ersland. Transport mechanisms for co2-ch4 exchange and safe co2 storage in hydrate-bearing sandstone. *Energies*, 8(5), 2015. ISSN 1996-1073. doi: 10.3390/en8054073.

Ray Boswell. Resource potential of methane hydrate coming into focus. *Journal of Petroleum Science and Engineering*, 56(1–3):9–13, 2007. ISSN 0920-4105. doi: http://dx.doi.org/10.1016/j.petrol.2006.09.002. URL http://www.sciencedirect.com/science/article/pii/S0920410506001847.

Ray Boswell and Timothy S Collett. Current perspectives on gas hydrate resources. *Energy & Environmental Science*, 4(4):1206–1215, 2011.

Ray Boswell, David Schoderbek, Timothy S. Collett, Satoshi Ohtsuki, Mark White, and Brian J. Anderson. The ignik sikumi field experiment, alaska north slope: Design, operations, and implications for co2âĂŞch4 exchange in gas hydrate reservoirs. *Energy & Fuels*, 31(1):140–153, 2017. doi: 10.1021/acs.energyfuels.6b01909. URL http://dx.doi.org/10.1021/acs.energyfuels.6b01909.

Royal Harvard Brooks and Arthur Thomas Corey. Hydraulic properties of porous media and their relation to drainage design. *Transactions of the ASAE*, 7(1):26–0028, 1964.

D. S. Brothers, C. Ruppel, J. W. Kluesner, U. S. ten Brink, J. D. Chaytor, J. C. Hill, B. D. Andrews, and C. Flores. Seabed fluid expulsion along the upper slope and outer shelf of the u.s. atlantic continental margin. *Geophysical Research Letters*, 41: 1–6, 2014.

Lawrence M Cathles and Duo Fu Chen. A compositional kinetic model of hydrate crystallization and dissolution. *Journal of Geophysical Research: Solid Earth (1978–2012)*, 109(B8), 2004.

Holger Class, Rainer Helmig, and Peter Bastian. Numerical simulation of nonisothermal multiphase multicomponent processes in porous media.: 1. an efficient solution technique. *Advances in Water Resources*, 25(5):533–550, 2002.

George E Claypool and IR Kaplan. The origin and distribution of methane in marine sediments. In *Natural gases in marine sediments*, pages 99–139. Springer, 1974.

Timothy S. Collett, Ray Boswell, Myung W. Lee, Brian J. Anderson, Kelly Rose, and Kristen A. Lewis. Evaluation of long-term gas-hydrate-production testing locations on the alaska north slope. 2012. doi: 10.2118/155504-PA.

Ann E Cook, Dave Goldberg, and Robert L Kleinberg. Fracture-controlled gas hydrate systems in the northern gulf of mexico. *Marine and Petroleum Geology*, 25 (9):932–941, 2008.

Hugh Daigle and Brandon Dugan. Origin and evolution of fracture-hosted methane hydrate deposits. *Journal of Geophysical Research: Solid Earth*, 115(B11), 2010.

K. N. Darnell, P. B. Flemings, and D. DiCarlo. Subsurface injection of combustion power plant effluent as a solid-phase carbon dioxide storage strategy. *Geophysical Research Letters*, 44(11):5521–5530, 2017. doi: 10.1002/2017GL073663. URL https://agupubs.onlinelibrary.wiley.com/doi/abs/10.1002/2017GL073663.

KN Darnell and PB Flemings. Transient seafloor venting on continental slopes from warmingâĂŘinduced methane hydrate dissociation. *Geophysical Research Letters*, 42(24), 2015. ISSN 1944-8007.

Matthew K Davie and Bruce A Buffett. A numerical model for the formation of gas hydrate below the seafloor. *Journal of Geophysical Research: Solid Earth (1978–2012)*, 106(B1):497–514, 2001.

Birol Dindoruk. Analytical theory of multiphase, multicomponent displacement in porous media. 1993.

Z. H. Duan, N. Moller, J. Greenberg, and J. H. Weare. The prediction of methane solubility in natural waters to high ionic strength from 0 to 250c and from 0 to 1600 bar. *Geochem. Cosmichim. Acta*, 56:1451–1460, 1992.

G Ersland, J Husebø, A Graue, BA Baldwin, J Howard, and J Stevens. Measuring gas hydrate formation and exchange with co2 in bentheim sandstone using mri tomography. *Chemical Engineering Journal*, 158(1):25–31, 2010.

Geir Ersland, Jarle Husebø, Arne Graue, and Bjørn Kvamme. Transport and storage of co2 in natural gas hydrate reservoirs. *Energy Procedia*, 1(1):3477–3484, 2009.

PB Flemings, JH Behrmann, CM John, and E Scientists. Gulf of mexico hydrogeology. In *Proceedings of the Integrated Ocean Drilling Program*, volume 308, 2006.

JM Frederick and BA Buffett. Taliks in relict submarine permafrost and methane hydrate deposits: Pathways for gas escape under present and future conditions. *Journal of Geophysical Research: Earth Surface*, 119(2):106–122, 2014.

Nagasree Garapati and Brian J. Anderson. Statistical thermodynamics model and empirical correlations for predicting mixed hydrate phase equilibria. *Fluid Phase Equilibria*, 373:20–28, 2014. ISSN 0378-3812. doi: http://dx.doi.org/10.1016/j.fluid.2014.03.010. URL http://www.sciencedirect.com/science/article/pii/S037838121400168X.

Sabodh K Garg, John W Pritchett, Arata Katoh, Kei Baba, and Tetsuya Fujii. A mathematical model for the formation and dissociation of methane hydrates in the marine environment. *Journal of Geophysical Research: Solid Earth*, 113(B1), 2008.

Arne Graue, B. Kvamme, Bernie Baldwin, Jim Stevens, James J. Howard, Eirik Aspenes, Geir Ersland, Jarle Husebo, and D. Zornes. Mri visualization of spontaneous methane production from hydrates in sandstone core plugs when exposed to co2. 2008. doi: 10.2118/118851-PA.

Anup K Gupta, P Raj Bishnoi, and Nicolas Kalogerakis. A method for the simultaneous phase equilibria and stability calculations for multiphase reacting and non-reacting systems. *Fluid Phase Equilibria*, 63(1-2):65–89, 1991.

LP Hauge, KA Birkedal, G Ersland, and A Graue. Methane production from natural gas hydrates by co2 replacement-review of lab experiments and field trial. In *SPE Bergen One Day Seminar*. Society of Petroleum Engineers, 2014.

Susan L. Hautala, Evan A. Solomon, H. Paul Johnson, Robert N. Harris, and Una K. Miller. Dissociation of cascadia margin gas hydrates in response to contemporary ocean warming. *Geophysical Research Letters*, 41(23):8486–8494, 2014.

ISSN 1944-8007. doi: 10.1002/2014GL061606. URL http://dx.doi.org/10.1002/2014GL061606. 2014GL061606.

Friedrich G. Helfferich. The theory of precipitation/dissolution waves. *AIChE Journal*, 35(1):75–87, 1989. doi: 10.1002/aic.690350108. URL https://onlinelibrary.wiley.com/doi/abs/10.1002/aic.690350108.

P. Henry, M. Thomas, and M. B. Clennell. Formation of natural gas hydrates in marine sediments 2. thermodynamic calculations of stability conditions in porous sediments. *J. Geophys. Res.*, 104:23005–23022, 1999.

Kurt Zenz House, Daniel P. Schrag, Charles F. Harvey, and Klaus S. Lackner. Permanent carbon dioxide storage in deep-sea sediments. *Proceedings of the National Academy of Sciences*, 103(33):12291–12295, 2006. doi: 10.1073/pnas.0605318103. URL http://www.pnas.org/content/103/33/12291.abstract.

MD Jager, AL Ballard, and ED Sloan. The next generation of hydrate prediction: Ii. dedicated aqueous phase fugacity model for hydrate prediction. *Fluid phase equilibria*, 211(1):85–107, 2003. ISSN 0378-3812.

Kristian Jessen, Guo-Qing Tang, and Anthony R. Kovscek. Laboratory and simulation investigation of enhanced coalbed methane recovery by gas injection. *Transport in Porous Media*, 73(2):141–159, Jun 2008. ISSN 1573-1634. doi: 10.1007/s11242-007-9165-9. URL https://doi.org/10.1007/s11242-007-9165-9.

Joel E. Johnson, Jürgen Mienert, Andreia Plaza-Faverola, Sunil Vadakkepuliyambatta, Jochen Knies, Stefan Bünz, Karin Andreassen, and Bénédicte Ferré. Abiotic methane from ultraslow-spreading ridges can charge arctic gas hydrates. *Geology*, 43(5):371–374, 2015. doi: 10.1130/G36440.1. URL http://geology.gsapubs.org/content/43/5/371.abstract.

Hyery Kang, Dong-Yeun Koh, and Huen Lee. Nondestructive natural gas hydrate recovery driven by air and carbon dioxide. *Scientific Reports*, 4:6616, 2014. URL http://dx.doi.org/10.1038/srep06616.

Susan W. Kieffer, Xinli Lu, Craig M. Bethke, John R. Spencer, Stephen Marshak, and Alexandra Navrotsky. A clathrate reservoir hypothesis for enceladus' south

polar plume. *Science*, 314(5806):1764–1766, 2006. doi: 10.1126/science.1133519. URL http://science.sciencemag.org/content/sci/314/5806/1764.full.pdf.

Dong-Yeun Koh, Hyery Kang, Dae-Ok Kim, Juwoon Park, Minjun Cha, and Huen Lee. Recovery of methane from gas hydrates intercalated within natural sediments using co2 and a co2/n2 gas mixture. *ChemSusChem*, 5(8):1443–1448, 2012. ISSN 1864-564X. doi: 10.1002/cssc.201100644. URL http://dx.doi.org/10.1002/cssc.201100644.

Huen Lee, Yongwon Seo, YuâĂŘTaek Seo, Igor L Moudrakovski, and John A Ripmeester. Recovering methane from solid methane hydrate with carbon dioxide. *Angewandte Chemie International Edition*, 42(41):5048–5051, 2003. ISSN 1521-3773.

Seungmin Lee, Yohan Lee, Jaehyoung Lee, Huen Lee, and Yongwon Seo. Experimental verification of methane–carbon dioxide replacement in natural gas hydrates using a differential scanning calorimeter. *Environmental Science & Technology*, 47(22):13184–13190, 2013. ISSN 0013-936X. doi: 10.1021/es403542z. URL http://pubs.acs.org/doi/abs/10.1021/es403542z.

S. Levitus, T. Boyer, M. Conkright, T. O'Brien, J. Antonov, and C. Stephens. World ocean database. 18, National Oceanographic Data Center, NOAA/NESIDS, 1998.

Jinxiang Liu, Yujie Yan, Jiafang Xu, Shujuan Li, Gang Chen, and Jun Zhang. Replacement micro-mechanism of ch4 hydrate by n2/co2 mixture revealed by ab initio studies. *Computational Materials Science*, 123:106–110, 2016. ISSN 0927-0256. doi: http://dx.doi.org/10.1016/j.commatsci.2016.06.025. URL http://www.sciencedirect.com/science/article/pii/S0927025616303123.

X. Liu and P. Flemings. Dynamic multiphase flow model of hydrate formation in marine sediments. *Journal of Geophysical Research*, 112:23, 2007.

Alberto Malinverno. Marine gas hydrates in thin sand layers that soak up microbial methane. *Earth and Planetary Science Letters*, 292(3-4):399–408, 2010.

Hector Marin-Moreno, Timothy A. Minshull, Graham K. Westbrook, Bablue Sinha, and Sudipta Sarkar. The response of methane hydrate beneath the seabed off-

shore svalbard to ocean warming during the next three centuries. *Geophysical Research Letters*, 40:1–5, 2013.

Héctor Marín-Moreno, Timothy A. Minshull, Graham K. Westbrook, and Bablu Sinha. Estimates of future warming-induced methane emissions from hydrate offshore west svalbard for a range of climate models. *Geochemistry, Geophysics, Geosystems*, 16(5):1307–1323, 2015. ISSN 1525-2027. doi: 10.1002/2015GC005737. URL http://dx.doi.org/10.1002/2015GC005737.

Jürgen Mienert, Maarten Vanneste, Stefan Bünz, Karin Andreassen, Haflidi Haflidason, and Hans Petter Sejrup. Ocean warming and gas hydrate stability on the mid-norwegian margin at the storegga slide. *Marine and Petroleum Geology*, 22 (1-2):233–244, 2005.

Alexei V. Milkov. Global estimates of hydrate-bound gas in marine sediments: how much is really out there? *Earth-Science Reviews*, 66(3–4):183 – 197, 2004a. ISSN 0012-8252. doi: http://dx.doi.org/10.1016/j.earscirev.2003.11.002. URL http://www.sciencedirect.com/science/article/pii/S0012825203001296.

Alexei V Milkov. Global estimates of hydrate-bound gas in marine sediments: how much is really out there? *Earth-Science Reviews*, 66(3):183–197, 2004b. ISSN 0012-8252.

G. Moridis. Numerical studies of gas production from methane hydrates. *SPE Journal*, 8:12, 2003.

George J. Moridis and Matthew T. Reagan. Estimating the upper limit of gas production from class 2 hydrate accumulations in the permafrost: 1. concepts, system description, and the production base case. *Journal of Petroleum Science and Engineering*, 76(3–4):194–204, 2011. ISSN 0920-4105. doi: http://dx.doi.org/10.1016/j.petrol.2010.11.023. URL http://www.sciencedirect.com/science/article/pii/S0920410510002676.

George J Moridis, Michael Brendon Kowalsky, and Karsten Pruess. Depressurization-induced gas production from class-1 hydrate deposits. *SPE Reservoir Evaluation & Engineering*, 10(05):458–481, 2007. ISSN 1094-6470.

Kazunari Ohgaki, Kiyoteru Takano, Hiroyuki Sangawa, Takuya Matsubara, and Shinya Nakano. Methane exploitation by carbon dioxide from gas hydrates. phase equilibria for co2-ch4 mixed hydrate system. *Journal of chemical engineering of Japan*, 29(3):478–483, 1996. ISSN 0021-9592.

Franklin Mattes Orr. *Theory of gas injection processes*. Tie-Line Publications, 2007.

Masaki Ota, Yuki Abe, Masaru Watanabe, Richard L. Smith Jr., and Hiroshi Inomata. Methane recovery from methane hydrate using pressurized {CO2}. *Fluid Phase Equilibria*, 228âĂŞ229:553 – 559, 2005a. ISSN 0378-3812. doi: https://doi.org/10.1016/j.fluid.2004.10.002. URL http://www.sciencedirect.com/science/article/pii/S0378381204004753. {PPEPPD} 2004 Proceedings.

Masaki Ota, Kenji Morohashi, Yuki Abe, Richard Lee Smith Masaru Watanabe, and Hiroshi Inomata Jr. Replacement of ch4 in the hydrate by use of liquid co2. *Energy Conversion and Management*, 46:1680–1691, 2005b.

M Paganoni, JA Cartwright, M Foschi, RC Shipp, and P Van Rensbergen. Structure ii gas hydrates found below the bottom-simulating reflector. *Geophysical Research Letters*, 2016. ISSN 1944-8007.

Justin L. Panter, Adam L. Ballard, Amadeu K. Sum, E. Dendy Sloan, and Carolyn A. Koh. Hydrate plug dissociation via nitrogen purge: Experiments and modeling. *Energy & Fuels*, 25(6):2572–2578, 2011. ISSN 0887-0624. doi: 10.1021/ef200196z. URL http://dx.doi.org/10.1021/ef200196z.

Youngjune Park, Do-Youn Kim, Jong-Won Lee, Dae-Gee Huh, Keun-Pil Park, Jaehyoung Lee, and Huen Lee. Sequestering carbon dioxide into complex structures of naturally occurring gas hydrates. *Proceedings of the National Academy of Sciences*, 103(34):12690–12694, 2006. doi: 10.1073/pnas.0602251103. URL http://www.pnas.org/content/103/34/12690.abstract.

Charles K Paull, Williamr Ussle, and Walter S Borowski. Sources of biogenic methane to form marine gas hydrates in situ production or upward migration? *Annals of the New York Academy of Sciences*, 715(1):392–409, 1994.

B. Phrampus and M. Hornbach. Recent changes to the gulf stream causing widespread gas hydrate destabilization. *Nature*, 490:527–531, 2012.

Benjamin J. Phrampus, Matthew J. Hornbach, Carolyn D. Ruppel, and Patrick E. Hart. Widespread gas hydrate instability on the upper u.s. beaufort margin. *Journal of Geophysical Research: Solid Earth*, 119(12):8594–8609, 2014. ISSN 2169-9356. doi: 10.1002/2014JB011290. URL http://dx.doi.org/10.1002/2014JB011290. 2014JB011290.

Gary A Pope et al. The application of fractional flow theory to enhanced oil recovery. *Society of Petroleum Engineers Journal*, 20(03):191–205, 1980.

J Posewang and J Mienert. The enigma of double bsrs: indicators for changes in the hydrate stability field? *Geo-marine letters*, 19(1-2):157–163, 1999.

Guillaume Rannou, Denis Voskov, Hamdi A Tchelepi, et al. Tie-line-based k-value method for compositional simulation. *SPE Journal*, 18(06):1–112, 2013.

Matthew T. Reagan and George J. Moridis. Dynamic response of oceanic hydrate deposits to ocean temperature change. *Journal of Geophysical Research*, 113: C12023, 2008.

Matthew T. Reagan and George J. Moridis. Large-scale simulation of methane hydrate dissociation along the west spitsbergen margin. *Geophysical Research Letters*, 36:L23612, 2009.

Gregor Rehder, Peter W. Brewer, Edward T. Peltzer, and Gernot Friederich. Enhanced lifetime of methane bubble streams within the deep ocean. *Geophysical Research Letters*, 29(15):21–1–21–4, 2002. ISSN 1944-8007. doi: 10.1029/2001GL013966. URL http://dx.doi.org/10.1029/2001GL013966.

C. A. Rochelle, A. P. Camps, D. Long, A. Milodowski, K. Bateman, D. Gunn, P. Jackson, M. A. Lovell, and J. Rees. Can co2 hydrate assist in the underground storage of carbon dioxide? *Geological Society, London, Special Publications*, 319(1):171–183, 2009. doi: 10.1144/sp319.14. URL http://sp.lyellcollection.org/content/319/1/171.abstract.

A. N. Salamatin, A. Falenty, T. C. Hansen, and W. F. Kuhs. Guest migration revealed in co2 clathrate hydrates. *Energy & Fuels*, 29(9):5681–5691, 2015. ISSN 0887-0624. doi: 10.1021/acs.energyfuels.5b01217. URL http://dx.doi.org/10.1021/acs.energyfuels.5b01217.

Kiran J. Sathaye, Toti E. Larson, and Marc A. Hesse. Noble gas fractionation during subsurface gas migration. *Earth and Planetary Science Letters*, 450:1 – 9, 2016. ISSN 0012-821X. doi: https://doi.org/10.1016/j.epsl.2016.05.034. URL http://www.sciencedirect.com/science/article/pii/S0012821X1630259X.

David Schoderbek and Ray Boswell. Ignik sikumi 1, gas hydrate test well, successfully installed on the alaska north slope. *Natural Gas & Oil*, 304:285–4541, 2011.

Young-ju Seo, Daeok Kim, Dong-Yeun Koh, Joo Yong Lee, Taewoong Ahn, Se-Joon Kim, Jaehyoung Lee, and Huen Lee. Soaking process for the enhanced methane recovery of gas hydrates via co2/n2 gas injection. *Energy & Fuels*, 29(12):8143–8150, 2015. doi: 10.1021/acs.energyfuels.5b02128. URL http://dx.doi.org/10.1021/acs.energyfuels.5b02128.

Carolyn J Seto, Kristian Jessen, and Franklin M Orr. A multicomponent, two-phase-flow model for co2 storage and enhanced coalbed-methane recovery. *SPE Journal*, 14(01):30–40, 2009. ISSN 1086-055X.

A. Skarke, C. Ruppel, M. Kodis, D. Brothers, and E. Lobecker. Widespread methane leakage from the sea floor on the northern us atlantic margin. *Nature Geosci*, 7(9):657–661, 09 2014. URL http://dx.doi.org/10.1038/ngeo2232.

E. D. Sloan. *Clathrate Hydrates of Natural Gases*. Marcel Decker, New York, 1998.

E Dendy Sloan Jr and Carolyn Koh. *Clathrate hydrates of natural gases*. CRC press, 2007. ISBN 1420008498.

Andrew J. Smith, Peter B. Flemings, Xiaoli Liu, and Kristopher Darnell. The evolution of methane vents that pierce the hydrate stability zone in the world's oceans. *Journal of Geophysical Research: Solid Earth*, 119(8):6337–6356, 2014a. ISSN 2169-9356. doi: 10.1002/2013JB010686. URL http://dx.doi.org/10.1002/2013JB010686. 2013JB010686.

Andrew J. Smith, Jürgen Mienert, Stefan Bünz, and Jens Greinert. Thermogenic methane injection via bubble transport into the upper arctic ocean from the hydrate-charged vestnesa ridge, svalbard. *Geochemistry, Geophysics, Geosystems*,

15(5):1945–1959, 2014b. ISSN 1525-2027. doi: 10.1002/2013GC005179. URL http://dx.doi.org/10.1002/2013GC005179.

Andrew J Smith, Jürgen Mienert, Stefan Bünz, and Jens Greinert. Thermogenic methane injection via bubble transport into the upper arctic ocean from the hydrate-charged vestnesa ridge, svalbard. *Geochemistry, Geophysics, Geosystems*, 15(5):1945–1959, 2014c. ISSN 1525-2027.

Christian Stranne, Matthew O'Regan, and Martin Jakobsson. Overestimating climate warming-induced methane gas escape from the seafloor by neglecting multiphase flow dynamics. *Geophysical Research Letters*, 43(16):8703–8712, 2016.

Duo Sun and Peter Englezos. Determination of co2 storage density in a partially water-saturated lab reservoir containing ch4 from injection of captured flue gas by gas hydrate crystallization. *The Canadian Journal of Chemical Engineering*, 95 (1):69–76, 2017. ISSN 1939-019X. doi: 10.1002/cjce.22655. URL http://dx.doi.org/10.1002/cjce.22655.

Duo Sun, John Ripmeester, and Peter Englezos. Phase equilibria for the co2/ch4/n2/h2o system in the hydrate region under conditions relevant to storage of co2 in depleted natural gas reservoirs. *Journal of Chemical & Engineering Data*, 61(12):4061–4067, 2016. doi: 10.1021/acs.jced.6b00547. URL http://dx.doi.org/10.1021/acs.jced.6b00547.

Peter K Swart, UG Wortmann, RM Mitterer, MJ Malone, PL Smart, DA Feary, and AC Hine. Hydrogen sulfide–hydrates and saline fluids in the continental margin of south australia. *Geology*, 28(11):1039–1042, 2000. ISSN 0091-7613.

Yoshihiro Terao, Mike Duncan, Bill Hay, and Le Dang. Deepwater methane hydrate gravel packing completion results and challenges. In *Offshore Technology Conference*. Offshore Technology Conference, 2014.

K. E. Thatcher, G. K. Westbrook, S. Sarkar, and T. A. Minshull. Methane release from warming-induced hydrate dissociation in the west svalbard continental margin: Timing, rates, and geological controls. *Journal of Geophysical Research: Solid Earth*, 118(1):22–38, 2013. ISSN 2169-9356. doi: 10.1029/2012JB009605. URL http://dx.doi.org/10.1029/2012JB009605.

ME Torres, Klaus Wallmann, AM Tréhu, Gerhard Bohrmann, WS Borowski, and H Tomaru. Gas hydrate growth, methane transport, and chloride enrichment at the southern summit of hydrate ridge, cascadia margin off oregon. *Earth and Planetary Science Letters*, 226(1):225–241, 2004.

Stanley M Walas. *Phase equilibria in chemical engineering*. Butterworth-Heinemann, 2013. ISBN 1483145085.

Klaus Wallmann, Elena Pinero, Ewa Burwicz, Matthias Haeckel, Christian Hensen, Andrew Dale, and Lars Ruepke. The global inventory of methane hydrate in marine sediments: A theoretical approach. *Energies*, 5(7):2449–2498, 2012.

Henry J Welge et al. A simplified method for computing oil recovery by gas or water drive. *Journal of Petroleum Technology*, 4(04):91–98, 1952.

Graham K. Westbrook, Kate E. Thatcher, Eelco J. Rohling, Alexander M. Piotrowski, Heiko Palike, Anne H. Osborne, Euan G. Nisbet, Tim A. Minshull, Mathias Lanoiselle, Rachael H. James, Veit Huhnerbach, Darryl Green, Rebecca E. Fisher, Anya J. Crocker, Anne Chabert, Clara Bolton, Agnieszka Beszczynska-Moller, Christian Berndt, and Alfred Aquilina. Escape of methane gas from the seabed along the west spitsbergen continental margin. *Geophysical Research Letters*, 36:L15608, 2009.

Curt M. White, Duane H. Smith, Kenneth L. Jones, Angela L. Goodman, Sinisha A. Jikich, Robert B. LaCount, Stephen B. DuBose, Ekrem Ozdemir, Badie I. Morsi, and Karl T. Schroeder. Sequestration of carbon dioxide in coal with enhanced coalbed methane recoverya review. *Energy & Fuels*, 19(3):659–724, 2005. doi: 10.1021/ef040047w. URL `https://doi.org/10.1021/ef040047w`.

Mark White and Won Suk Lee. Guest molecule exchange kinetics for the 2012 ignik sikumi gas hydrate field trial. In *Offshore Technology Conference*. Offshore Technology Conference, 2014.

Wenyue Xu and Leonid N Germanovich. Excess pore pressure resulting from methane hydrate dissociation in marine sediments: A theoretical approach. *Journal of Geophysical Research: Solid Earth*, 111(B1), 2006.

Catherine MR Yonkofski, Jake A Horner, and Mark D White. Experimental and numerical investigation of hydrate-guest molecule exchange kinetics. *Journal of Natural Gas Science and Engineering*, 2016.

Kehua You, David DiCarlo, and Peter B Flemings. Quantifying hydrate solidification front advancing using method of characteristics. *Journal of Geophysical Research: Solid Earth*, 120(10):6681–6697, 2015. ISSN 2169-9356.

Yeobum Youn, Minjun Cha, Minchul Kwon, Juwoon Park, Yutaek Seo, and Huen Lee. One-dimensional approaches for methane hydrate production by co2/n2 gas mixture in horizontal and vertical column reactor. *Korean Journal of Chemical Engineering*, pages 1–8, 2016. ISSN 1975-7220. doi: 10.1007/s11814-015-0294-5. URL http://dx.doi.org/10.1007/s11814-015-0294-5.

MH Yousif, HH Abass, MS Selim, ED Sloan, et al. Experimental and theoretical investigation of methane-gas-hydrate dissociation in porous media. *SPE reservoir Engineering*, 6(01):69–76, 1991.